INSTABILITIES IN COLLISIONAL PLASMAS STUDIED BY MEANS OF 3-D KINETIC PARTICLE-IN-CELL SIMULATIONS

by

Steffen Mattias Brask

Thesis

for the degree of

Master of Science

Faculty of Mathematics and Natural Sciences
University of Oslo

December 2018

"If I have seen further it is by standing on the shoulders of Giants"
Isaac Newton, 1675

Abstract

This thesis presents the first set of results from 3-Dimensional kinetic simulations of the Farley-Buneman instability in the framework of a new Particle-in-Cell code PINC. A new null-collision module is implemented in PINC, which uses the regular null-collision scheme, but with modified cross-section models. The new collision module is rigorously tested using several tests derived from theory, proving its validity. It is shown how the Farley-Buneman instability simulations agree with the original theory of Buneman (1963) and Farley Jr. (1963), and some modern theoretical concepts. A comparison with recent simulations is made, and several similarities and discrepancies are pointed out. The results include a stability analysis on the simulations performed, and show how numerical effects can play a role in collisional Particle-in-Cell simulations.

Acknowledgements

I am very proud of of the work that was mainly done by me to get this thesis finished. However, it would never have been possible without certain people.

To my girlfriend Hou Jie, I know these past months have been hard on you. I am very grateful that you have supported me through all of this.

I would first like to thank all of my great fellow students at the 4DSpace Strategic Research Initiative group. I have enjoyed all of our talks over the broken coffee machine. It is true that one will never truly know anyone in the same way you know someone with whom you walked into battle, and this is how I feel about all of you. I would especially like to thank Vigdis Holta for all of the support, and interest in my work.

Throughout the whole masters project I have received extremely high quality advice, guidance, and feedback from Sigvald Marholm. I am surprised and grateful for the amount of help I have received from him.

I have to thank my primary supervisor Wojciech Miloch for all of his guidance. It truly is amazing how many projects one man can be a central part of. To my co-supervisors Hideuki Usui, and Yohei Myiaki, thank you for all of the help, especially during my stay in Japan.

I also thank Bjørn Lybekk for always being available to help with technical issues.

At last I want to thank my parents. I would never have been where I am without you believing in me.

Contents

1 Introduction **1**
1.1 Scope Of This Thesis 2

2 Theoretical background **5**
2.1 Basic Equations 5
2.1.1 Single Particle Motion 6
2.1.2 Plasma Parameters 6
2.2 Instabilities In Plasmas 8
2.2.1 Classification Of Instabilities 8
2.2.2 Analogy To Classical Mechanics 9
2.2.3 Dispersion Relations 10
2.2.4 Two-Stream Instability 11
2.3 Farley-Buneman Instability 13
2.3.1 Linear Fluid Theory 13
2.3.2 Linear Kinetic Theory 17
2.3.3 Conditions For Growth 17
2.3.4 Ion Thermal Effects 20
2.3.5 Non-Linear Theory 21

3 Numerical Method **23**
3.1 Particle in Cell Main Idea 23
3.1.1 Derivation Of PIC Method 25
3.2 Particle In Cell - Implementation In PINC 26
3.2.1 Integration Of The Equations Of Motion 26
3.2.2 Field Solver 28
3.2.3 Particle Weighting 29
3.3 Simulation Constraints 30
3.3.1 Finite Grid 30
3.3.2 Finite Time 30
3.3.3 The CFL Condition 31
3.3.4 Resolving Oscillations Due To External B 31
3.3.5 Additional Constraints 31

3.4 Monte Carlo Collision Module . . . 32
3.4.1 General Description Null-Collision Module . . . 33
3.4.2 Collision Geometry . . . 34
3.4.3 Electron-Neutral Elastic Collision . . . 35
3.4.4 Ion-neutral Elastic Collision . . . 36
3.4.5 Ion-Neutral Charge-Exchange Collision . . . 37
3.4.6 Cross-Sections . . . 37
3.5 Implementation In PINC . . . 40
3.5.1 Design Choices . . . 41
3.5.2 The Collision Functions . . . 42
3.5.3 The Scatter Functions . . . 44
3.5.4 MCC Initialization And Normalization . . . 44
3.6 Verification MCC . . . 45
3.6.1 Verification Using Change In Energies . . . 47
3.7 Simulation Setup . . . 53
3.8 Data Analysis Tools . . . 56
3.8.1 Electric Field . . . 56
3.8.2 Fourier Transforms . . . 57
3.8.3 Temperatures . . . 57
3.9 Scale of FB Simulations . . . 57

4 Results **59**
4.1 FB Instability - Simulation Runs . . . 59
4.1.1 Comparing Baseline To Optional Run . . . 59
4.1.2 Lowered Driving Electric Field . . . 70
4.2 Baseline Simulation - Stability Test . . . 76

5 Discussion **81**
5.1 Comparing Result With Theory . . . 81
5.2 Result With New MCC Module . . . 83
5.3 Results With Numerical Issues . . . 84

6 Future work **85**
6.1 Improving the Collision model . . . 85
6.2 Improving The Field Solver . . . 86

Appendices **89**

A Additional Collision Tests **91**

B Growth rate Baseline vs Optional **97**

Chapter 1

Introduction

In the ionospheric E-region, at high and low latitudes, electric currents develop during periods of high geomagnetic activity. These currents are driven by the interaction between the solar wind and the Earth's magnetosphere. the solar wind consisting of charged particles gets focused in at the magnetic poles, driving the polar electrojets. The electrojet is responsible for large scale transverse polarization electric fields, which give rise to currents flowing perpendicular to the geomagnetic field. In strongly driven cases these currents can lead to irregularities in the plasma density. These irregularities form with strictly magnetic field aligned fronts, and propagate mainly in the direction of the Hall current D. T. Farley (1985).

As early as in 1937, Eckersley (1937) radar backscatter was observed from the upper atmosphere. The origin of the irregularities that gave rise to the backscatter was not known at that time, but later experiments in the 1950s and 1960s in conjunction with theoretical advancements allowed to attribute them to large amplitude ion sound waves J. Sahr and G. Fejer (1996). A large number of radar experiments were performed from that time until today in attempts to further understand the complex nature of these irregularities. For a comprehensive review see J. Sahr and G. Fejer (1996). The radar data is usually composed of a Doppler-shifted radar backscatter. This type of data gives accurate measurements of the power spectrum of the backscatter and phase speed of the irregularities, but is generally lacking in fine structure details.

It was determined that local measurements where needed, and in the mid 1960s the first sounding rockets where launched to get in-situ data (project: AD-II-52 1964, published: McNamara (1969)). Because of the high drag in the lower E-region satellites can not hold an orbit, and therefore sub-orbital sounding rockets are used instead. The rocket data represents all knowledge we have of the absolute level of density fluctuations. However, sounding rockets are expensive, so a large amount of dedication is given for each launch. This leads to launch campaigns, which are conducted with a few years in between. With flight times in the range of minutes, and a single point of data in space

(usually a few, but close in space), along a trajectory in time. This means that rocket data is sparse.

With numerical simulations we can address the problem of E-region instabilities, not being limited in the analysis by sparse rocket data collected by in-situ measurements. In a simulation we can extract data from the whole simulated domain, which can provide a deeper insight of the physics of the irregularities. In recent years computer efficiency has reached a point where computer simulations have become an increasingly useful tool. Early on plasma simulations where done in 1 dimension to help prove the existence of Landau damping Hockney and Eastwood (1988). This also proved the viability of simulations as a powerful experimental tool. A spike in interest of developing better codes over the next couple of decades lead to the self consistent Particle-in-Cell (PIC) model, pioneered with the Berkeley code in 1972 C. K. Birdsall and Langdon (1985). Because of the scales involved as will be discussed later in this thesis, the E-region irregularities could not be studied until computers became powerful enough. The first attempt at simulating these irregularities using a kinetic approach for both ions and electrons was done by Janhunen (1994) in 2 spatial dimensions. These simulations showed great promise, and a characteristic turning of the waves. This result lead to several theories being developed to explain this behaviour. However, the inherent three dimensional nature of the irregularities where of course absent. The first fully kinetic three dimensional simulation on a large scale was done by Oppenheim M. M. and Dimant Y. S. (2013). Although efficiency has come a long way, to put things in perspective, this simulation was run on $\sim$ 8000 CPU's for 35 hrs, amounting to roughly 30 years on one CPU.

1.1 Scope Of This Thesis

The main goal of this thesis is to simulate a highly collisional plasma, typical of the lower ionospheric E-region, at high latitude. We wish to do this to gain insight into the complex nature of the plasma irregularities observed in this region of the ionosphere.

To reach this goal we will do a series of experiments, using numerical methods. The past 4 years a new Particle-in-Cell (PiC) code has been developed by the 4DSpace Strategic Research Initiative at the University of Oslo. This code has been called PINC. To reach our goal we will use PINC as the main framework to run simulations. PINC will need a new collisional module because collisions are a central part of the physics of irregularities in the E-region.

We choose to implement a collisional module in PINC using the null-collision Monte Carlo Collisions (MCC) method Vahedi and Surendra (1995). Within the MCC method we will implement our own cross-section models that are made to work on the energy ranges of interest (typical E-region, a detailed explanation follows). We must also

rigorously test this new MCC module to show that it works as expected.

Lastly, the ultimate goal is to set up, and run a series of simulations, using the new collision module. We will present the results of these simulations, and link them to theory, to prove that we are simulating the observed plasma irregularities. We will discuss where these simulations show expected behaviour, and where they deviate from theory. In this discussion we will try to pinpoint whether the deviation is due to numerical effects in the scope of a fully kinetic Particle-in-Cell simulation, or unexplained physics.

Chapter 2

Theoretical background

In the introduction we referred to the E-region irregularities as “irregularities” after the original radar backscatter research. In the literature these irregularities are often classified as type 1, type 2, type 3, and type 4, where the exact definition is not sharply defined. However most agree on the type 1 irregularities. These irregularities are today known to originate from the Farley-Buneman (FB) instabilities, also referred to as Farley-Buneman turbulence after the original theoretical formulation of the irregularities Buneman (1963) and Farley Jr. (1963). Where “type 1” will generally refer to the form of the radar backscatter, and FB instability refers to the physical process that result in such backscatter. Although all these types are included in the theory, we will focus on the type 1 (sometimes called “pure” Farley-Buneman instabilities). In general, in this thesis, when we talk about FB instabilities we will be referring to the physical process that leads to type 1 backscatter.

2.1 Basic Equations

In plasma physics we need to consider both single particle motion and the overall collective behaviour. The single particle motion is important since the mean free path of a particle is often long enough for the single particle motion to be valid. In other words, the density is often low enough that collisions don’t dominate in the bulk plasma. However, we still require the density to be "large enough“ that collective effects dominate over single particle, or particle-particle effects. This is reflected in the plasma parameter, and means that the electro-magnetic forces acting on a particle needs to be a sum of force terms from ”enough“ other particles.

2.1.1 Single Particle Motion

In a plasma, since the density is low enough that particles can move relatively freely, we need to consider single particle motion Chen (2016). Consider the case of a single charged particle, subject only to a a magnetic $\vec{B}$, and electric $\vec{E}$ field. The force on the particle from the fields is the Lorentz force

$$\vec{F} = q(\vec{E} + \vec{v} \times \vec{B}) \tag{2.1}$$

Where q is the charge, and $\vec{v}$ is the particles velocity. In the absence of any other forces the particle will gyrate around the magnetic field lines Chen (2016) and H. Pécseli (2012). The radius of gyration (gyroradius) is given by

$$r_g = \frac{m_s v_\perp}{|q|B} \tag{2.2}$$

where the subscript s indicates a particle specie, and $v_\perp$ is the speed of the particle in the plane perpendicular to $\vec{B}$. Note that the gyroradius is often called the Larmor radius r_L, or cyclotron radius r_c. The frequency of the gyrations is given by the gyro frequency

$$\Omega_s = \frac{|q|B}{m_s}. \tag{2.3}$$

The gyro frequency is also often called the cyclotron frequency Ω_c.

A single particle subject to an electric field which is perpendicular to a magnetic field, will drift with the average drift velocity given as Chen (2016)

$$\vec{v}_d = \frac{\vec{E} \times \vec{B}}{B^2} \tag{2.4}$$

This drift is sometimes called a Hall drift, or the $\vec{E} \times \vec{B}$ drift. The direction of such a drift is perpendicular to both the electric and magnetic field. For this drift to be valid we need to consider several gyro periods, and take the average position of a particle. This position is called the guiding center.

2.1.2 Plasma Parameters

In the bulk plasma, when several particles are in the vicinity of each other, one positive charge will attract negative charges, and at some distance from the positive charge its

potential will be shielded from the negative charges gathering around it. The scale length in which the potential from one charge is shielded is given by the Debye length λ_D, which defines a sphere in three dimensions. Outside the Debye sphere, particles are unable to distinguish potential contributions from discrete particles inside the sphere. The electron Debye length is given by Chen (2016)

$$\lambda_D = \sqrt{\frac{\epsilon_0 k_B T_e}{n_e e^2}} \tag{2.5}$$

where n_e is the electron number density, e the elementary charge, m_e is electron mass, and ϵ_0 is the vacuum permitivity. k_b is the Boltzmann constant, and T_e is the electron temperature. On scale lengths smaller than the Debye length, quasi neutrality breaks down. Because of this, for the charged gas to be considered a plasma, we require $\lambda_D \ll L$, where L is the length of the system. Positive and negative charges have potential energy stored in the electric field between them. If the charges are free to move, that potential energy will be released to kinetic energy, and the particles will gain speed. In a plasma, where particles are on average free to move, this phenomenon will happen collectively. If we consider a quasi-neutral plasma, and then perturb the electrons slightly, energy will be stored in electric fields between ions and electrons. If we consider the ions to be massive, energy will then oscillate between potential, and kinetic for the electrons with the electron plasma frequency ω_p Chen (2016).

$$\omega_p = \sqrt{\frac{n_e e^2}{m_e \epsilon_0}} \tag{2.6}$$

The definition of a characteristic scale length λ_D, and the inverse characteristic time ω_p, leads to a definition of a characteristic speed $v_{th,e}$. Where we define this speed through $\lambda_D = v_{th,e}\omega_p^{-1}$. From the definitions above we can see that $v_{th,e}$ is the standard deviation of the thermal speed from a Maxwellian distribution

$$v_{th,s} = \sqrt{\frac{k_b T_s}{m_s}} \tag{2.7}$$

Where the subscript s indicates the specie, and we used electrons for the characteristic speed.

For a charged gas to be considered a plasma we require $N_D \ggg 1$, that means that we require the number of particles within a Debye sphere to be much more than one. This is because collective effects should dominate over singe particle or particle-particle effects. The plasma parameter N_D is defined as Chen (2016)

$$N_D = \frac{4\pi}{3} n \lambda_d^3 \tag{2.8}$$

where $n \approx n_e \approx n_i$ is the the number density of particles. We can note straight away that the requirement $N_D \ggg 1$ also needs to hold for the number of particles in simulations, where we might use super particles that represent several real particles.

In an ordinary neutral gas, pressure waves propagate by collisions as sound waves. An analogous phenomenon occurs in a plasma with few collisions, and no neutrals, where the wave propagates through the electric field. We call this ion acoustic waves. Considering a collisionless plasma, linearizing the fluid equation, and assuming plane waves leads to the dispersion relation for ion acoustic waves (eq. 4.41 Chen (2016)). (he has $\gamma_e = 1$)

$$C_s \equiv \frac{\omega}{k} = \sqrt{\frac{\gamma_i T_i + \gamma_e T_e}{m_i}}, \tag{2.9}$$

where C_s is speed of the waves, γ_s is a specie specific heat ratio (in 3 dimensions $\gamma_s = 1$ for isothermal particles, and $\gamma_s = 5/3$ for adiabatic), ω is the frequency of the wave in time, and k is the wave number. T_s is the temperature for specie s, and m_i the ion mass.

2.2 Instabilities In Plasmas

Plasma instabilities might seem like mathematical constructs, but it is proven experimentally that they are real physical phenomena. However when identifying an instability through mathematical considerations we need to be able to pinpoint the source of energy that drives the amplitude of the waves. If this is not possible, the instability can not be considered to be physical.

2.2.1 Classification Of Instabilities

Plasma instabilities are classified in some different ways in the literature. Many choose to classify them in two general groups

1. Hydrodynamic instabilities - which generally refer to instabilities which can be identified in magneto hydro dynamics (MHD).

2. Kinetic instabilities - which need a kinetic treatment, using the Vlasov equation.

We can further use the classifications provided by Chen (2016):

	Type	Source
Streaming Instabilities	Hydrodynamic	Stream or beam of particles
Rayleigh-Taylor instabilities	Hydrodynamic	External force (gravity)
Universal instabilities	Hydrodynamic	Expansion from pressure
Kinetic instabilities	Kinetic	Complex particle velocity distribution

where the source relates to the energy that drives the instability. In this thesis we will focus on the streaming instabilities, where the source of energy is from different species having a drift velocity relative to one another. In particular we will focus on streaming instabilities that arise due to electrons streaming through collisionally slowed ions. Where the "stream" is due to the $\vec{E} \times \vec{B}$ drift of the electrons eq. 2.4, and the source of free energy is the external electric field.

2.2.2 Analogy To Classical Mechanics

To understand what a plasma instability is, we start with an analogy to classical mechanics.

Consider a simple mass-spring system. This is an harmonic oscillator, but we include a friction term. In this system a ball of mass m is extended from a fixed surface by a spring. The spring exerts the force $F_{spring} = -kx(t)$, given by Hooke's law. We use a linear term for the friction $F_{friction} = -\mu v\,(t)$ Newtons 2. law then gives us the equation of motion

$$m\frac{dx(t)}{dt} = -\mu\frac{dx(t)}{dt} - kx(t) \tag{2.10}$$

We can do a practical guess, and define the variables

$$\omega_0 = \sqrt{\frac{k}{m}}, \qquad \gamma = \frac{\mu}{2m} \tag{2.11}$$

Where ω_0 is the natural frequency of the system, and γ is the damping factor. Rewriting eq. 2.10 to use ω_0 and γ,

$$\frac{dx(t)}{dt} + 2\gamma\frac{dx(t)}{dt} + \omega_0^2 x(t) = 0 \tag{2.12}$$

By assuming a solution on the form $e^{\lambda t}$, we get the characteristic equation

$$\lambda^2 + 2\gamma\lambda + \omega_0^2 = 0. \tag{2.13}$$

Inserting this into the quadratic equation to obtain the roots

$$\lambda = -\gamma \pm \sqrt{\gamma^2 - \omega_0^2}. \tag{2.14}$$

We are interested in the underdamped solutions, where the system loses a small amount of energy at each oscillation, but we still have oscillations. So we are looking for complex solutions, that means that $\gamma^2 - \omega_0^2 < 0$. Plugging this back into the assumed and solution, and taking Euler's identity, we get two possible solutions. We write the full solution as a superposition of these two as $x(t) = c_1 x_1(t) + c_2 x_2(t)$, to get

$$x(t) = x_0 e^{-\gamma t} \cos(\sqrt{\omega_0^2 - \gamma^2} t). \tag{2.15}$$

The term $e^{-\gamma t}$ gives us exponential decay of the oscillations. Physically the system loses energy to the surroundings, usually as heat, through friction. If we instead let the system gain energy from the surroundings, through a linear force, say $F_{ext} = \mu v(t)$, we would have a solution with a exponential growth

$$x(t) = x_0 e^{\gamma t} \cos(\sqrt{\omega_0^2 - \gamma^2} t). \tag{2.16}$$

where the term $e^{\gamma t}$ now gives us exponential growth of the oscillations. Such a system would not persist in nature as nonlinear effects would dampen or break the system, For example the spring will brake at some point, or be deformed such that the spring force can not be considered linear.

This is a good analogy to instabilities in plasmas. Plasma instabilities are much more complicated, and differ from this simple example as they often have inherent nonlinear properties. However, they often have a linear growth phase, analogous to the spring force still holding, and a non linear phase, analogous to the spring braking or deforming. In plasma instabilities similar non linearities that arise from kinetic effects, can also lead to linear analysis not holding any more.

2.2.3 Dispersion Relations

In plasma physics dispersion relations are important tools for understanding the dynamics of a plasma under certain conditions. A dispersion relation gives the relation between the frequency ω and the wave vector $\vec{k}$, where $k \equiv |\vec{k}|$. From the analysis of the dispersion relations several properties of a wave can be inferred, such as

phase velocity Chen (2016)

$$v_{ph} = \frac{\omega}{k}, \tag{2.17}$$

and the group velocity Chen (2016)

$$v_g = \frac{d\omega}{dk}. \tag{2.18}$$

Analyzing the dispersion relation can uncover the frequency range of the wave (extremal points), or under which conditions the wave is growing or damped (complex root analysis).

Dispersion relations in plasma physics are often found through linearization of the fluid equations of motion, using a linearization of an infinitesimal perturbation of the quantities involved. In these cases they include the linear phenomenon, but are void of complex non linear effects.

2.2.4 Two-Stream Instability

As a method of understanding the steps involved in retaining a dispersion relation for a plasma instability, we can first consider a basic two-stream instability. We follow the derivation in chapter 6.6 of Chen (2016).

We consider a cold uniform unmagnetized plasma. The electrons and ions have a velocity $\vec{v}_0 = v_0\hat{x}$ relative to each other. We let the frame of the observer move with the ions, so $\vec{v}_{0,i} = 0, \vec{v}_{0,e} = \vec{v}_0$.

Then, the linearized equations of motion can be written as Chen (2016)

$$m_i n_0 \frac{\partial \vec{v}_{i,1}}{\partial t} = e n_0 \vec{E}_1 \tag{2.19}$$

$$m_e n_0 \left[\frac{\partial \vec{v}_{e,1}}{\partial t} + (\vec{v}_0 \cdot \nabla)\vec{v}_{e,1} \right] = -e n_0 \vec{E}_1 \tag{2.20}$$

These equations are fluid momentum equations, using the lorentz force as the force term, with zero magnetic field. To linearize the equations we have assumed assuming that $\vec{v}_{s,0}$ can, after a very short time, be written as a linearization $\vec{v}_{s,0+dt} = \vec{v}_{s,0} + \vec{v}_{s,1}$ of the original term plus a small perturbation.

Using continuity for electrons and ions, and remembering that $\vec{v}_{0,i} = 0$, we get

$$\frac{\partial n_{e,1}}{\partial t} + n_0 \nabla \cdot \vec{v}_{e,1} + (\vec{v}_0 \cdot \nabla) n_{e,1} = 0, \qquad \frac{\partial n_{i,1}}{\partial t} + n_0 \nabla \cdot \vec{v}_{i,1} = 0. \tag{2.21}$$

Looking for electrostatic plane waves, we assume the form of

$$\vec{E}_1 = Ee^{i(kx-wt)}\hat{x} \tag{2.22}$$

inserting and doing a Fourier analysis, where

$$\frac{\partial}{\partial t} = -i\omega, \qquad \nabla = i\vec{k} \tag{2.23}$$

one will arrive at the dispersion relation

$$1 = \omega^2\Big[\frac{m_e/m_i}{\omega^2} + \frac{1}{(\omega - kv_0)^2}\Big] \tag{2.24}$$

Looking for complex roots of the dispersion relation, and taking them to be written on the form

$$\omega = \omega_r + i\gamma \tag{2.25}$$

The time dependence of the oscillating electric field will now be given by

$$\vec{E}_1 = Ee^{i(kx-\omega_r t)}e^{\gamma t}\hat{x} \tag{2.26}$$

From this it is simple to see that if complex roots exist, these will lead to an exponential decay of the oscillations in $\vec{E}$ if the imaginary part is negative, or they will lead to an exponential growth if the imaginary part is positive. It is found that for sufficiently small kv_0, there are complex roots, and one can show that these roots lead to the growth rate Chen (2016)

$$\gamma \approx \omega_p\Big(\frac{m_e}{m_i}\Big)^{1/3} \tag{2.27}$$

The theory says that for any value of k, v_0 needs to be sufficiently small for an instability to occur. This makes little sense physically since v_0 is the source of energy driving the instability. This problem is accounted for if we treat it with kinetic theory (within the Vlasov frame), where Landau damping will occur if $v_0 \leq v_{th}$. This means that the oscillations (plane waves) will be damped out if v_0 is too small, and thus there is no instability.

2.3 Farley-Buneman Instability

In this section we introduce the mathematics of the Farley-Buneman (FB) instability. The FB-instability is similar to the two-stream instability as it arises when the electrons drift (”stream“) through the ions. This happens due to the ions being slowed by collisions. Collisions are therefore an important part of the FB-instability, but they also complicate the mathematics, and physics.

We start with some of the important results from the original work of Buneman Buneman (1963). Next we will review a more modern formulation of the dispersion relation, and a solution which gives us the growth function for the FB-instability. After this a somewhat heuristical explanation is given to understand the physics of the FB-instability, and at last we will review some of the most recent theoretical advancements for the FB-instability.

2.3.1 Linear Fluid Theory

In the 1950’ several radar experiments observed reflections in the polar aurora, and the equatorial electrojet. Most of the reflections early on where made with 50 MHz signals witch correspond to a wavelength of 3m J. Sahr and G. Fejer (1996). There was also observed some slightly longer and shorter length reflections. The first general dispersion relation to explain these waves was given by Buneman in 1963 Buneman (1963).

Buneman observed that the ionospheric instability was analogous to other known plasma wave phenomena which were excited by streaming electrons. In order to have streaming electrons he first assumed the condition

$$\nu_e m_e << eB << \nu_i m_i, \tag{2.28}$$

Here $\nu_{e,i}$, $m_{e,i}$ is the collision frequency, and mass of the electron (e) and ion (i), e is the elementary charge, and B is the magnetic field. This condition tells a lot about the dynamical system of the plasma, as it implies that the electrons are magnetized, and the ions are not. The magnetized electrons will follow the $\vec{E}x\vec{B}$ drift, and the ions will drift as a Pedersen current in the $\vec{E}$ direction. This makes the electrons ”stream“ through the ions and can make the plasma unstable.

The general dispersion relation was derived from a three component gas analysis using a Navier-Stokes equation for each component, and was given by Buneman as follows Buneman (1963):

$$\frac{\omega}{k}\left(1-\frac{\nu_i^2}{\omega_{pi}^2}-\frac{\nu_i^2 m_i m_e}{e^2B^2}\right)=\frac{8k_bTk}{3m_i\omega}-\frac{\nu_i}{\nu_e}\left[v_d-\frac{\omega}{k}\left(1+\frac{\nu_i m_i \nu_e m_e}{e^2B^2}\right)\right] \tag{2.29}$$

where v_d is the component of drift in the direction of wave propagation, and k_b is the Boltzmann constant, with T being the temperature of the neutral background. For waves to persist the Doppler shifted frequency for the electrons should be negative $\omega' = \omega - kv_d$ which yields the condition

$$v_d > (\omega/k)(1+\nu_i m_i \nu_e m_e/e^2B^2). \tag{2.30}$$

Through various simplifications, and using continuity of the density perturbations, and ignoring small terms, it is possible to determine an angle at which undamped propagation can take place Buneman (1963)

$$\frac{v_d}{\omega/k}-1-\frac{\nu_i m_i \nu_e m_e}{e^2B^2}=\frac{\nu_i m_i}{\nu_e m_e}\cos^2\theta \tag{2.31}$$

This angle is often referred to as the aspect angle θ. The aspect angle is the relative angle between the direction of the wave vector $\vec{k}$, and the magnetic field $\vec{B}$. This was an important result because it gives a small range of angles where waves can persist (or grow), close to $\vec{B}_\perp$, which coincided with observations.

The same year as Buneman published his linear fluid theory, there was also published a linear kinetic theory by Farley Farley Jr. (1963), describing the same phenomena. The kinetic approach by Farley gave the same dispersion relation as the one of Buneman, but was more complicated by the mathematics of the kinetic approach.

Over the next couple of decades the fluid theory was revised and refined several times, and a general solution to the dispersion relation equation was derived. A fairly complete account is given in (Fejer et. al. 1984) or (Farley 1985). As with Buneman's theory it is valid only when $\nu_i \gg \Omega_i, \nu_e \ll \Omega_e$, (equivalent to equation 2.28). Again the dispersion relation is derived using the well known first-order continuity and momentum (Navier-Stokes) equations for electrons and ions, in particular

$$\frac{\partial n}{\partial t}+\nabla\cdot(n\vec{v})=Q-2\alpha n^2, \tag{2.32}$$

$$m\frac{D}{Dt}\vec{v}=q(-\nabla\phi+\vec{v}\times\vec{B})-\frac{\nabla P}{n}-m\nu\vec{v}. \tag{2.33}$$

Where each fluid specie has their own set of equations, with specie specific variables for density, velocity, and pressure $n, \vec{v}, P$, but we have omitted the subscript. These equations include effects of production Q, and recombination α rates, for particles. The operator $\frac{D}{Dt}$ is called the convective derivative, and is defined Chen (2016)

$$\frac{D}{Dt} = \frac{\partial}{\partial t} + (\vec{v} \cdot \nabla) \tag{2.34}$$

To close the set of equations a form of Poisson's equation can be used B. G. Fejer, Providakes, and Donald T. Farley (1984)

$$\nabla^2 \phi = e(n_e - n_i)/\epsilon_0 \tag{2.35}$$

To derive a dispersion relation the usual first order linearization of perturbations is used, e.g. $\chi = \chi + \tilde{\chi}$, for any perturbed parameter χ. Further, assuming plane waves B. G. Fejer, Providakes, and Donald T. Farley (1984), neglecting electron inertia and ion motion along the magnetic field Sudan, Akinrimisi, and D. T. Farley (1973) B. Fejer et al. (1975), and only field aligned irregularities are considered i.e ($k_\perp \ll k_\parallel$). Quasi neutrality is also assumed, and we get the dispersion relation B. G. Fejer, Providakes, and Donald T. Farley (1984) in the reference frame of the ions,

$$\begin{aligned}&[\nu_i - i(\omega - \Omega_i/kL_n)](\bar{\omega} - \vec{k} \cdot \vec{v}_d) + [\bar{\omega}(\Omega_i^2 + (\nu_i - i\omega)^2) \\ &+ ik^2 C_s^2(\nu_i - i(\omega - \Omega_i/kL_n))]\Big(\frac{\psi}{\nu_i} - \frac{i}{kL_n\Omega_i}\Big) = 0.\end{aligned} \tag{2.36}$$

Where $L_n = n \sec\theta \frac{\partial n}{\partial h}^{-1}$ is a typical scale length of density perturbations along $\vec{B}$, and is assumed to be small. The parameter ψ is defined as

$$\psi \equiv \frac{\nu_e \nu_i}{\Omega_e \Omega_i}\Big(1 + \frac{\Omega_e^2 k_\parallel^2}{\nu_e^2 k^2}\Big) \tag{2.37}$$

Here $\vec{v}_d = \vec{v}_e - \vec{v}_i$, as it is given in the reference frame of the ions, is the total (cross-field and field-aligned) drift velocity. For a complete derivation see B. G. Fejer, Providakes, and Donald T. Farley (1984).

By assuming a solution to the dispersion relation on the form

$$\omega = \omega_r + i\gamma \tag{2.38}$$

We get a solution to the dispersion relation with a real and imaginary part

$$\omega_r = (\vec{k} \cdot \vec{v}_d)/(1+\psi) \tag{2.39}$$

and

$$\gamma \simeq (1+\psi)^{-1}\left[\frac{\psi}{\nu_i}(\omega_r^2 - k^2 C_s^2) + \frac{\omega_r \nu_i}{\Omega_i k L_n}\right] - 2\alpha N_0 \tag{2.40}$$

Equation 2.40 accounts for both type 1, and type 2 radar backscatter. D. T. Farley (1985) describes several properties and differences between these two types. In the present type 2 is primarily resulting from what is known as gradient drift waves. These are accounted for in the third term in the bracket of equation 2.40. The factor L_n is typically on the order of kilometers, and this term is therefore negligible for short wavelength waves. The first two terms account for type 1 backscatter, (sometimes called "pure" FB waves). These two terms are proportional to k and will dominate at short wavelengths. Type 1 backscatter is today what is usually associated to the Farley-Buneman instability, and it is the focus of this thesis. The last term in 2.40 will always dampen the waves, but not change the physics beyond dampening growth. This dampening will be minimal for short wavelengths because recombination happens slowly compared to the timescale of the wave. In addition the simulator does not at present account for recombination. (production or destruction of charged particles.) In our simulations we can thus neglect gradient drift and recombination to get the following expression for the FB growth rate:

$$\gamma \simeq (1+\psi)^{-1}\left[\frac{\psi}{\nu_i}(\omega_r^2 - k^2 C_s^2)\right] \tag{2.41}$$

It can often be useful to do simplified calculations of ideal cases where we can use

$$\psi_0 = \frac{\nu_e \nu_i}{\Omega_e \Omega_i}. \tag{2.42}$$

ψ_0 will often be close to ψ since $k_\parallel \ll k$

From these results we can do some further simplifications. It is useful to know the threshold drift velocity i.e. the drift velocity where the growth equals zero. By inserting eq. 2.39 into eq. 2.41 with $\gamma = 0$ we find

$$\vec{k} \cdot \vec{v}_d = k C_s (1+\psi) \tag{2.43}$$

Where we neglected the gradient drift and recombination terms. We can simplify this even further by assuming $\vec{k}$, and $\vec{v}_d$ to have the same direction and assuming that drift due to collisions is small (see a complete expression for the drift in B. G. Fejer,

Providakes, and Donald T. Farley (1984)) the drift is close to the $\vec{E}_0 \times \vec{B}_0$ drift, where $\vec{E}_0$ is the external driving electric field, and $\vec{B}_0$ is the external magnetic field. (This also implies that we have assumed the aspect angle to be zero). Inserting this, and taking the absolute value we get

$$\frac{E_0}{B_0} = C_s(1 + \psi) \tag{2.44}$$

This equation can be used to find threshold (minimum) values for the parameters involved, usually the threshold electric field E_{trs}.

2.3.2 Linear Kinetic Theory

Fluid theory gives us the simplest mathematical approach to find the dispersion relation for the FB-instability. However, to understand under which conditions this dispersion relation is valid we need to consider kinetic theory. Kinetic plasma theory is often more complicated to develop as they start with the Boltzmann equation, and use a distribution function. The fluid equations for continuity, and momentum can be derived from the collisionless Boltzmann equation, called the Vlasov equation. This means that some information is already lost when using the fluid equations.

The kinetic theory of the FB-instability leads to the same dispersion relation as the fluid theory Farley Jr. (1963), but it needs several assumptions that give limitations on when the dispersion relation 2.36 is valid, and thus when eq. 2.40 is valid, and leads to growth. We will discuss these in a subsequent section.

2.3.3 Conditions For Growth

To understand the dynamics of the FB-instability we need to ask two questions. First, how can waves in the E-region persist? Second, what drives the instability i.e, how can waves grow? For the pure FB waves (accounted for in the two first terms in the bracket of eq. 2.40, and the reason for type 1 backscatter) these two questions are answered in Y. S. Dimant and Sudan (1995) or Yakov S. Dimant and Meers M. Oppenheim (2003).

In this simplified explanation ions are assumed to have a drift close to zero. We consider only the dimension parallel to $\vec{v}_d$, and waves strictly parallel to $\vec{k}$. The electrons have a drift velocity $v_d > v_{ph}$, such that the electrons drift past the wave. In the frame of reference moving along with the wave, the wave represents quasi-stationary density perturbations dn. The electrons will drift ahead of the collisionally slowed ions, which gives rise to a polarization electric field $d\vec{E}$ parallel to $\vec{k}$.

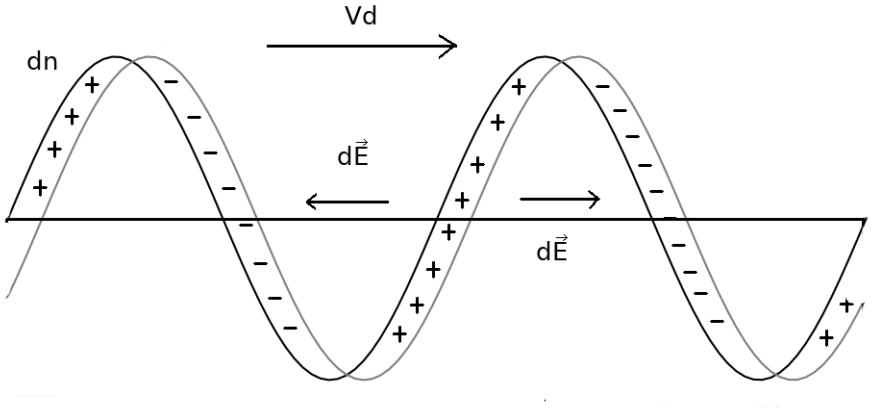

Figure 2.1: Schematic diagram of the mechanism behind FB-instability. Retained from Yakov S. Dimant and Meers M. Oppenheim (2003) . In this schematic the frame is co moving with the wave at a velocity v_{ph}. The ions then have the velocity $-v_{ph}$, and the electrons have the velocity $v_d - v_{ph}$, with $v_d > v_{ph}$. The quasi stationary wave is represented by the density perturbation dn, and the conditions give rise to the polarization electric field dE.

The direction of $d\vec{E}$ is such that it slows down both electrons and ions at local density hills, and speed them up at wells. It is possible to show Yakov S. Dimant and Meers M. Oppenheim (2003) Y. S. Dimant and Sudan (1995) that neglecting ion inertia, and pressure gradients, will lead to the quasi-stationary wave persisting in this manner. If however one takes into account pressure gradients $\Delta dP = \Delta(dnT_e + dnT_i)$ Yakov S. Dimant and Meers M. Oppenheim (2003), this will generally lead to damping of the initial density perturbation dn. Now, the answer to the second question is given in Y. S. Dimant and Sudan (1995). For waves to grow we need to take into account ion inertia. This leads to an additional term in the ion force balance equation

$$m_i(\vec{v}_i \cdot \Delta)\vec{v}_i \equiv \Delta\frac{m_i\vec{v}_i^2}{2} \simeq -m_i\vec{v}_{ph}^2\frac{\Delta dn}{n} \tag{2.45}$$

From this additional term we can see that since the ion velocities have local maxima at the local minima of the density perturbations dn (due to the polarization electric field dE), and the ion velocities have local minima at the maxima of the density perturbations. This additional gradient "pressure" has the opposite sign of the normal pressure gradient. Furthermore, when this gradient is larger than the normal pressure gradient, the density perturbations will grow.

Both the linear fluid and kinetic theory uses conditions to arrive at the dispersion relation. Kinetic theory often uses the same, and some extra conditions as fluid theory.

A summary of these conditions is given in Y. S. Dimant and Sudan (1995)) and presented below.

$$\tau^{-1} \ll \Omega_i, \omega \ll \nu_{in} \ll \nu_{en} \ll \Omega_e, \qquad \delta_{en} \ll 1 \tag{2.46}$$

$$\nu_{ii} \ll \nu_{in}, \nu_{ei} \sim \nu_{ee} \ll \nu_{en} \tag{2.47}$$

$$k_\perp r_{ge} \ll 1, \qquad r_{ge} \ll \lambda_e \ll k_\parallel^{-1} \ll L, \qquad k\lambda_i \ll 1 \tag{2.48}$$

$$k\lambda_d \ll 1 \tag{2.49}$$

$$\delta_{ei}\nu_{ei} \ll \nu_{in}, \qquad \delta_{ei} \ll 1 \tag{2.50}$$

Here we adopt the notation in the original paper where ω, $k_\parallel$, and $k_\perp$ are as before the wave frequency, and wave numbers parallel and perpendicular to the ambient magnetic field B. $\nu_{ee} \sim \nu_{ii}$ are the electron-electron, and ion-ion collision frequencies. λ_e, λ_i are the electron and ion mean free paths (not to be confused with Debye length). r_{ge}, Ω_e, Ω_i are the gyroradius and gyro frequencies, and λ_d is the Debye length. τ and L are typical temporal and spatial scale variations of time, and length along B. δ_{ei}, and δ_{en} are the fractions of energy lost in one electron-ion, or electron-neutral collision.

The first condition 2.46 is a modification to 2.28 including some extra terms. This inequality says that we need unmagnetized ions, due to collisions with neutrals, and magnetized electrons. In addition the electron-neutral collision frequency needs to be greater than the ion-neutral collision frequency. This is so that quasi-neutrality is maintained. We can also see that the wave frequency must be lower than both ν_{en}, and ν_{in}

The second inequality 2.47 tells us that ion-neutral and electron-neutral collisions must dominate. For our purposes in a collisionless PIC simulation with the added MCC module this will always be satisfied.

The third inequality 2.48 says that a wave traveling perpendicular to B must be larger than the gyroradius of the electrons. So "short" waves are omitted from the solution. The mean free path of the electrons needs to be larger than the gyroradius of the electrons, and the mean free path of the ions must be shorter than any wavelength. This gives us an accepted range of wavelengths which is usually on the scale of $10cm - 10m$, it is stated in several places Yakov S. Dimant and Meers M. Oppenheim (2003) and J. Sahr and G. Fejer (1996) that the wavelength is comparable or greater than the mean free path.

The two last inequalities 2.49, and 2.50 say that the wave must be larger than the Debye length. This is again to maintain quasi-neutrality, and that the energy exchange in electron-ion collisions can not be too large, as there is an assumption of thermal equilibrium between the ions and neutrals.

2.3.4 Ion Thermal Effects

Recently a number of new models have been developed for the Farley-Buneman instability Yakov S. Dimant and Meers M. Oppenheim (2003) and L. M. Kagan and Kelley (2000). These models take into account different driving mechanisms of the instability, like ion-thermal (IT), electron-thermal (ET) in addition to the "pure" FB instability, where "pure" refers to the ion inertia mechanism explained above. The differentiation of these mechanisms is a somewhat artificial construct as they are all included in the original dispersion relation 2.36. However, they provide insight in mechanisms that can alter the behaviour of the system. In particular the IT driving mechanism that arises from the thermal perturbations of the ions being out of phase with the density perturbations Yakov S. Dimant and Meers M. Oppenheim (2003). The analysis provided in the model by Yakov S. Dimant and Meers M. Oppenheim (2003) gives us an estimate of the optimum flow angle θ and the optimum wavelength.

$$\frac{k v_{th,i}}{\nu_i} = (\kappa_i |\tan\chi)^{1/2} \lesssim 1. \tag{2.51}$$

Where $v_{th,i}$, ν_i are the ion thermal velocity and collision frequency. $\kappa_i \equiv \frac{\Omega_i}{\nu_i}$ is the ion magnetization parameter, χ is related to the usual flow angle θ through $\chi = \theta + \arctan\kappa_i$, and θ is the angle between $\vec{E} \times \vec{B}$ and $\vec{k}$ (if we assume $\vec{k}$ to be strictly perpendicular to $\vec{B}$, θ is the angle of flow for the waves in the plane perpendicular to $\vec{B}$).

We can point out that the optimum flow for the "pure" FB instability should be $\chi_{opt} \approx 0$, so $\theta_{opt} \approx \chi_{opt} \approx 0$, is close to zero for low magnetized ions. However it is unclear if there exits other mechanisms that can alter the preferred flow angle. For the IT mechanism χ_{opt} is between 0 and -45 degrees from the direction of the $\vec{E} \times \vec{B}$ drift, in the plane perpendicular to $\vec{B}$.

In addition to the optimum flow angle, Yakov S. Dimant and Meers M. Oppenheim (2003) also provides modifications to electric field threshold values. Another useful result from Yakov S. Dimant and Meers M. Oppenheim (2003) is the expression for the polarization electric field

$$dE = \frac{dn}{n_0} \frac{v_d}{\mu_i(1+\psi)}, \qquad \mu_i = \frac{e}{m_i \nu_{in}}. \tag{2.52}$$

Where μ_i is the Pedersen mobility along the electric field, and the waves propagate parallel to the drift v_d.

2.3.5 Non-Linear Theory

Several attempts at extending theory to include non linear effects have been made. These non-linear theories show accurate matching of certain parameters with observational data. However, the lack of precise experimental data to verify them, and certain discrepancies, has lead to them not gaining general acceptance.

A usual approach to explain the non-linear turbulent nature of the FB instability is to extend the linear theory to include wave coupling of two or three modes. This leads to a system that will saturate and show density and phase velocities similar to observations Hamza and Imamura (2001) and Otani and M. Oppenheim (2006). In wave coupling models the energy is transferred from one wave in the $B_\perp$ plane to a wave with a large aspect angle (significant component along $B_\parallel$).

Another approach to explain non linear saturation of the FB-instability is that of the non-spectral "blob" method St.-Maurice and Hamza (2001) and Hysell and Drexler (2006). In the "blob" model a density blob is shown to get polarized leading to the blob turning away from the regular drift. The turning is also shown to lead to saturation of the growing density perturbation. In St.-Maurice and Hamza (2001) we are given an expression for the angle of flow for the blob

$$\cos\theta_{max} = \frac{C_s(1+\psi)}{E_0/B} \tag{2.53}$$

Where E_0 is the external driving electric field, and θ_{max} is the maximum flow angle. It is implicitly assumed that the blob will rotate to θ_{max}.

Other promising models are those of Haldoupis et al. (2005), that look at the effects of density gradients on the FB-instability. Or Bahcivan and Cosgrove (2010) that that discuss the effects of vertical electron density gradients on the FB-instability.

All of these models exclude either some kinetic effects or some dimension, to limit the case. The result of this is that none of them capture the full 3-D kinetic turbulent behaviour of the Farley-Buneman instability.

Chapter 3

Numerical Method

In this chapter we will briefly explain the methods we use to solve the different parts of the Particle-in-Cell (PiC) main cycle. These will be explained in short as most details where worked out by others, and are documented elsewhere. As the time of writing there is no complete reference, but this will be made available in the PHD thesis of Sigvald Marholm, while a partial account is given in Killie (2016).

Next, the new Monte Carlo Collision (MCC) Module will be explained in some detail, as this has been worked out as a part of this project. Lastly, we will show some tests performed to verify the implementation of the Null-collision MCC method in PINC.

3.1 Particle in Cell Main Idea

In the PiC method the goal is to realistically simulate physics using simplifications enabling us to compute larger systems with more particles. These simplifications are in particular using a grid as an intermediate between the particles and forces, and the use of super particles.

The simplest approach to particle simulations is the Particle-Particle (PP) method. In this method we directly compute the contribution to a force on a particle from every other particle. This makes it easy to argue for the validity of the simulation but for a system with N_p particles it gives a complexity of $O(N_p(N_p-1)) \simeq O(N_p^2)$ Hockney and Eastwood (1988) for the force calculations. The PP method could be used for small systems where the physics of interest involves few particles but once we are interested in physical effects in larger systems this scalability means the computational power needed to solve the forces might be impossible on even the largest High-Performance-Computers (HPC) of today.

The PiC method solves the problem of scalability from the PP method by weighting

the particle quantities to a grid. Following is an explanation, with reference to fig 3.1. Given a distribution of N_p particles with each particle having a value x_p and v_p, we start in the weighting square on the right of the figure. We then weight these particle values to adjacent grid points using a suitable weighting scheme to get charge and current densities. the most common is the nearest grid point (NGP) or cloud in cell (CIC) schemes. With the density of particle values at the grid points we then use a suitable field solver to solve Maxwell's equations. From these fields we then interpolate back to the particle position to obtain the force on each particle. Lastly, we use some numerical integrator to accelerate, and move the particles. This cycle is then repeated for each time step. Each part in the PIC cycle in fig. 3.1, used in PINC, is further explained in subsequent sections.

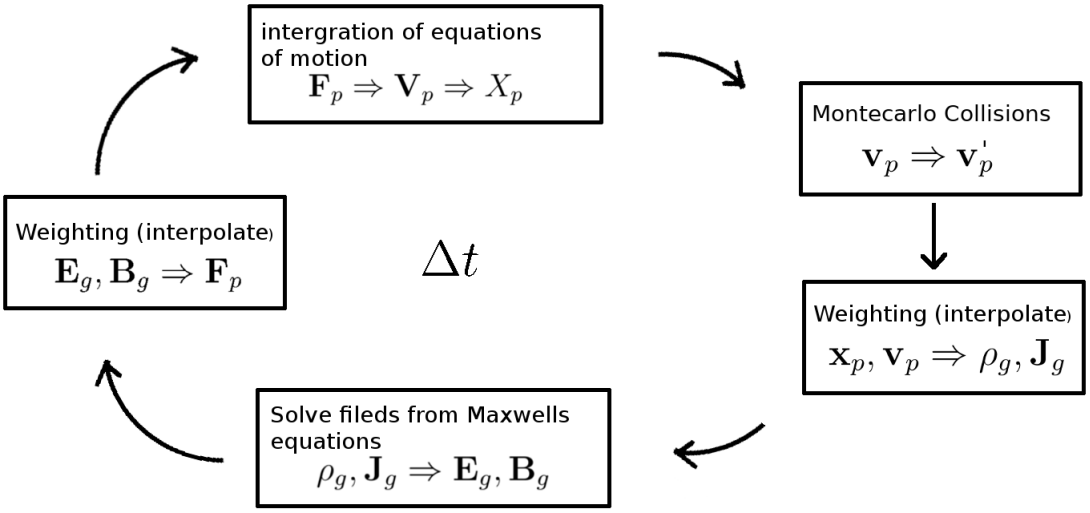

Figure 3.1: PIC scheme main cycle. The subscript p refers to particle p. the subscript g refers to grid point g. In the right weighting square charge ρ, and current $\vec{J}$, densities are computed from the particle positions. in the next square we compute electric field $\vec{E}$, and magnetic field $\vec{B}$ from these densities. In the weighting square on the left we interpolate field values from grid to particle position to get the force F_p on particle p. From the force we can update the positions and velocities for all particles. Last the collision module changes velocities of collided particles from v_p to v_p'

The complexity is dependent on the type of grid solver, often given as $O(N_g log(N_g))$, Hockney and Eastwood (1988) with N_g grid points, and the particles contribute $O(N_p)$. Our code, PINC, uses an electro-static multigrid solver which has a complexity of $O(N_g)$ Trottenberg, Oosterlee, and Schuller (2000), so the total complexity is $O(N_g) + O(N_p)$. This is clearly better than the PP method.

The grid quantities are defined as field quantities at discrete points on the grid and are given by Maxwell's equations in SI units

$$\text{Gauss' Law: } \nabla \cdot \vec{E} = \frac{\rho}{\epsilon_0} \tag{3.1}$$

$$\text{Gauss' Law for magnetism: } \nabla \cdot \vec{B} = 0 \tag{3.2}$$

$$\text{Maxwell - Faraday: } \nabla \times \vec{E} = -\frac{\partial \vec{B}}{\partial t} \tag{3.3}$$

$$\text{Ampere's law: } \nabla \times \vec{B} = \mu_0(\vec{J} + \epsilon_0 \frac{\partial \vec{E}}{\partial t}) \tag{3.4}$$

where $\vec{E}$ is the electric field, and $\vec{B}$ is the magnetic field. ϵ_0 and μ_0 are the permitivity and permeability of free space, ρ is the charge density, and the forces are given at the particle position from the Lorentz force eq. 2.1

3.1.1 Derivation Of PIC Method

In the classical texts C. K. Birdsall and Langdon (1985) Hockney and Eastwood (1988) they give a heuristic derivation of the PIC method. In later texts Lapenta (2012) we are given a more rigid mathematical derivation.

A full derivation is beyond the scope of this thesis, but I would like to point out some important observations from the derivation given in Lapenta (2012).

First it is proven that with the PIC method we are indeed solving the Vlasov equation

$$\frac{\partial f_s(\vec{x}, \vec{v}, t)}{\partial t} + \vec{v} \cdot \frac{\partial f_s(\vec{x}, \vec{v}, t)}{\partial \vec{x}} + \vec{a} \cdot \frac{\partial f_s(\vec{x}, \vec{v}, t)}{\partial \vec{v}} = 0 \tag{3.5}$$

Where $f_s(\vec{x}, \vec{v}, t)$, is a distribution function, which is the sum of the distribution functions for each particle. The Vlasov equation is sometimes called the collisionless Boltzmann equation. Solving the Vlasov equation through a Particle-in-Cell method means that we are simulating a collisionless plasma. This can be understood by considering two particles within one grid length. In reality these could collide through a Coulomb collision, where the force responsible for the scattering is the Coulomb force. With the Coulomb force the particles will be subject to a stronger force if they are in the same cell, possibly resulting in a collision. While If they are in adjacent cells the force will be weaker, likely not resulting in a collision. In PiC the force will be interpolated via the grid. In the standard PiC method the force will therefore go to zero as the distance between the particles goes to zero Lapenta (2012). Accurately simulating collective behaviour, but omitting collisional effects.

Solving the Vlasov equation means that the model is fully kinetic, and uses only first principles. Each particle is however a super particle, and should be treated as a part

of phase space. For the CIC scheme the particles velocities are delta functions and the positions have a spread in space equal to the grid spacing. The super particles are thus a collection of real particles contained in a cube that all follow the same trajectory.

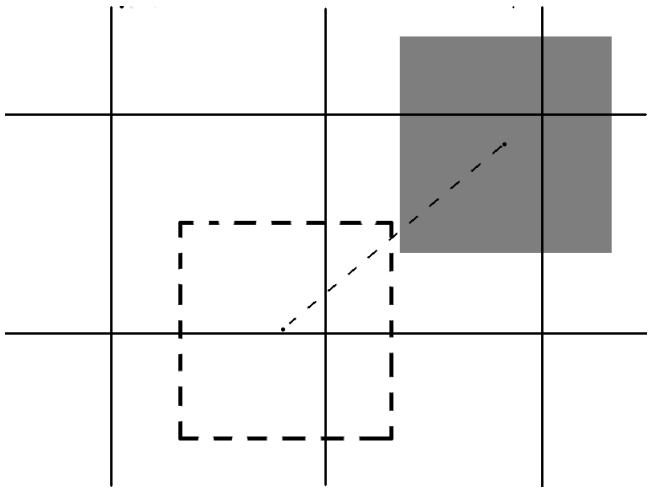

Figure 3.2: Visualization of a super particle moving across grid points in 2-D. The old position is shown by the dotted square, with the actual position in its centre. The updated position at the next time step is shown by the gray square.

A visualization of a super particle moving in a grid in 2-D is given in fig. 3.2. In this figure the area of the square representing a super particle that is within a grid square is proportional to the amount of charge that is interpolated to that grid point.

3.2 Particle In Cell - Implementation In PINC

In this section we review the relevant run time methods used in PINC. We will focus on the methods we use later in simulations, and the methods that are implemented as a part of this thesis.

3.2.1 Integration Of The Equations Of Motion

Since this thesis is focused on magnetized plasmas we choose to use the Boris algorithm. The Boris algorithm is a variation of the leapfrog algorithm, where position and velocity is offset by a half time step. The discrete equations to solve are the classical equations of motion discretized as follows

$$\frac{\vec{x}_p^{t+\Delta t} - \vec{x}_p^{t}}{\Delta t} = \vec{v}_p^{t+\frac{\Delta t}{2}} \tag{3.6}$$

$$\frac{\vec{v}_p^{t+\frac{\Delta t}{2}} - \vec{v}_p^{t-\frac{\Delta t}{2}}}{\Delta t} = \frac{q_s}{m_s}(\vec{E}_p + \frac{\vec{v}_p^{t+\frac{\Delta t}{2}} - \vec{v}_p^{t-\frac{\Delta t}{2}}}{2} \times \vec{B}_p) \tag{3.7}$$

Where Δt indicates the time step, the superscript indicates time, and the subscript p means *at the particle* with index p, and we used the Lorentz force as the force term. The Boris algorithm C. K. Birdsall and Langdon (1985) uses eq. 3.6, but decomposes eq. 3.7 into a part that adds half the acceleration, then rotates the particle due to the external $\vec{B}$, and last adds the second half of the acceleration.

$$\begin{aligned}
\vec{v}_p^{-} &= \vec{v}_p^{t-\frac{\Delta t}{2}} + \frac{q_s}{m_s}\vec{E}_p\frac{\Delta t}{2} \\
\vec{v}_p^{'} &= \vec{v}_p^{-} + \vec{v}_p^{-} \times \vec{T} \\
\vec{v}^{+} &= \vec{v}_p^{-} + \vec{v}_p^{'} \times \vec{S} \\
\vec{v}_p^{t+\frac{\Delta t}{2}} &= \vec{v}^{+} + \frac{q_s}{m_s}\vec{E}_p\frac{\Delta t}{2}
\end{aligned} \tag{3.8}$$

Where we have used the same notation as C. K. Birdsall and Langdon (1985) The rotational parameters are given by

$$\begin{aligned}
\vec{T} &= \hat{\mathbf{B}}_p \cdot \tan(\frac{q_s \Delta t}{2m} B_p) \\
\vec{S} &= \frac{2\vec{T}}{1 + \vec{T}^2}
\end{aligned} \tag{3.9}$$

The Boris algorithm is widely used in applications where the solver (i.e the physics) is electrostatic, but we still have an external magnetic field. In this case the rotational parameters need only be determined in the initialization of the program, and equations 3.8 iterated over each particle p. The Boris algorithm also has the advantage that it can not add energy to the system from the magnetic field, only a rotation. This makes it a good choice for use in combination with electrostatic solvers, where the electric fields are self consistent Qin et al. (2013).

3.2.2 Field Solver

The field solver of choice is the multigrid solver available in PINC. For details on this solver see the master thesis of Killie (2016). The solver is based on the book on multigrid from Trottenberg, Oosterlee, and Schuller (2000).

The main idea in multigrid is to speed up iterative solvers by solving them on a coarser grid first. On a coarser mesh we can obtain a solution faster. Then using this solution as an initial condition on a finer mesh, we can obtain a solution on this finer mesh faster. This can then also be done on an even finer mesh than originally defined to minimize the error in fewer iterations.

There is much theory dedicated to optimizing a multigrid solver to a problem, with what is called V-cycles W-cycles Trottenberg, Oosterlee, and Schuller (2000) and Killie (2016), how many levels of finer and coarser meshes to use etc. A well optimized multigrid solver scales with its complexity given as $O(N_g)$ on the local domain, and is one of the fastest electrostatic solvers to date. However, when using a decomposed domain as we do in PINC the global complexity is $O(N_g log(N_g))$

One drawback with the multigrid solver is that we solve the system in spatial domain and not in the frequency domain, and thus lose the option to store frequency data each time step without an extra Fourier transform function.

Multigrid uses the Gauss-Seidel algorithm which is an electrostatic solver, lets start with Gauss law for electricity, 3.1.

$$\nabla \cdot \vec{E} = \frac{\rho}{\epsilon}. \tag{3.10}$$

Since we are only interested in the electro-static solution we neglect any change in the magnetic field over time. From Faraday's law 3.3 we can see that that means the electric field is curl free $\nabla \times \vec{E} = 0$. Thus, from Helmholtz theorem we can define the electric field in terms of a scalar electric potential $\vec{E} = -\nabla\phi$. Substituting this back into Gauss law for electricity produces Poisson's equation

$$\nabla^2\phi = -\frac{\rho}{\epsilon} \tag{3.11}$$

This solution will neglect any physics that propagates in the magnetic field. Gauss-Seidel uses a Forward-Time-Centralized-Space scheme to solve Poisson's equation iteratively. We write these equations for one dimension,

$$\frac{\phi_g^{n+1} - \phi_g^{n-1}}{2\Delta x} = \vec{E}_g \tag{3.12}$$

and the discretization of the potential is obtained from

$$\frac{\phi_g^{n+1} - 2\phi_g^n + \phi_g^{n-1}}{\Delta x^2} = -\frac{\rho_g}{\epsilon_0} \tag{3.13}$$

Where the subscript g implies evaluation at the grid points, and the superscript refers to spatial grid point indices. It is straight forward to extend these to two, and three dimensions. There are some details in the Gauss-Seidel even-odd (red black) ordering, and special attention must be given to the boundary conditions Killie (2016).

3.2.3 Particle Weighting

PIC employs different schemes when weighting particles to the grid. We are simulating with super particles, and thus each simulated particle represents several real particles. So we need to define how much of these particles should reside at each of the neighboring grid points.

The most used schemes historically are the NGP (Nearest Grid Point), and CIC (Cloud In Cell). CIC is sometimes referred to as LS (linear spline), which is in line with higher order weighting schemes called QS (Quadratic Spline) or CS (Cubic Spline). For computational efficiency, and reasonable accuracy we use the linear interpolation CIC scheme.

For CIC we can define a linear weighting function Verboncoeur (2005)

$$\vec{w}_{i,j,k} = \vec{x}_p - \vec{X}_{i,j,k} \tag{3.14}$$

where the $\vec{x}_p$ is the position of particle p and $\vec{X}_{i,j,k}$ is the position of the nearest lower grid point. With this weighting function we can iterate over each particle and accumulate charge at the grid points, written out in 2 dimensions.

$$\begin{aligned} Q_{i,j} &= q_p(1 - w_i)(1 - w_j) \\ Q_{i+1,j} &= q_p w_i(1 - w_j) \\ Q_{i,j+1} &= q_p(1 - w_i)w_j \\ Q_{i+1,j+1} &= q_p w_i w_j \end{aligned} \tag{3.15}$$

Extending this to 3 dimensions is straight forward. The total charge on a grid point is now known and the charge density is found by $\rho = Q_{i,j,k}/V_{i,j,k}$, where $V_{i,j,k}$ is the volume of grid point i, j, k

A similar scheme is employed when interpolating the electric field to the particle, but instead of splitting the charge to several grid points we sum up contributions to the electric field from several grid points.

3.3 Simulation Constraints

In this section we will review and explain several analytical constraints on the stability of a simulated system. When running simulations we need to make sure that the system we simulate is numerically stable. A numerically unstable system can add unphysical effects, and in the worst case lead to exponential growth resulting in the simulation crashing.

3.3.1 Finite Grid

In our Particle-in-Cell code PINC we use a grid on which field quantities are discretely defined. Particles exist in a continuous space, and thus create fluctuations in the field quantities in continuous space. These fluctuations need to be resolved, and are generally on the scale of a Debye length. More rigid mathematical approaches can be found in Lapenta (2012) and C. K. Birdsall and Langdon (1985). If we let the spacing between the grid points be Δx the finite grid stability criteria can be expressed as

$$\Delta x < C\lambda_D \tag{3.16}$$

Where the constant C is dependent on the method used for interpolation. For Cloud-in-Cell (CiC) it is π. Failure to meet this criteria will cause aliasing of the poorly resolved fluctuations. This in turn leads to heating of the plasma until it is fulfilled.

3.3.2 Finite Time

We use an explicit forward-time integrator to move particles. The usage of such an integrator is subject to the finite time stability criteria. Using a Von Neumann type stability analysis on a discretized harmonic oscillator will lead to the equation Lapenta (2012), C. K. Birdsall and Langdon (1985), and Hockney and Eastwood (1988)

$$\sin\left(\frac{\omega_{num}\Delta t}{2}\right) = \pm\frac{\omega\Delta t}{2} \tag{3.17}$$

where ω_{num} is the numerical frequency, and ω is the real frequency we are trying to represent numerically. The sine function has complex solutions for any value outside of $[-1, 1]$, and thus if we try to represent oscillations $\omega\Delta t/2 > 1$, this leads to complex solutions. We can therefore formulate the finite time stability criteria as

$$\omega\Delta t < 2 \tag{3.18}$$

for any ω we simulate. Failing to meet this criteria will lead to an exponential growth of ω, which will unboundly heat the plasma.

3.3.3 The CFL Condition

The Courant-Friedrichs-Lewis (CFL) stability criteria, originally proposed by Courant, Friedrichs, and Lewy (1967), connects time and space resolution Δt, Δx in one criteria. It can be formulated as Trivellato and Raciti Castelli (2014)

$$\frac{\Delta x}{\Delta t} > C \tag{3.19}$$

Where C is a characteristic speed. This gives a finite "speed limit" in a simulation with finite Δx, Δt. If this criteria is not met, the solution will not converge, i.e we get the wrong solution.

3.3.4 Resolving Oscillations Due To External B

We need to resolve the smallest length scale of any physics by the grid size. If the smallest length scale is determined by the gyroradius r_g, this leads to the somewhat stringent condition

$$\Delta x < r_g \tag{3.20}$$

This condition is often stated with words when doing simulations, but empirical studies have shown that this condition may be too relaxed Horký, Miloch, and Delong (2017).

3.3.5 Additional Constraints

In addition to the simulation constraints imposed by discretizing time and space there are a number of additional limitations and constraints that should be taken into account when simulating the FB-instability.

In order to have wave growth in the simulated system, we must require the polarization electric field due to the density perturbations to be larger than the electric field generated by discrete noise. For any system of n_p particles per unit of space the fluctuations can be written as

$$\hat{E} \propto 1/\sqrt{n_p} \tag{3.21}$$

where $\hat{E}$ is the average fluctuation level. For a PiC simulation this is the number of particles per cell.

In order to maintain the correct simulated Pedersen drift rate M. M. Oppenheim and Y. S. Dimant (2004) we need

$$\frac{\Omega_{e,pic}}{\nu_{e,pic}} = \frac{\Omega_e}{\nu_e}. \tag{3.22}$$

In practice, this limitation says that if we artificially change one of the parameters in the gyro frequency we need to rescale the collision frequency accordingly. Usually this parameter is mass, and in the case of mass the simulated particles already represent a number of real particles. So raising the mass means we let each simulated particle represent even more simulated particles, and thus one collision in the simulator counts as several more physical collisions, and therefore we need to lower the collision rate proportionally.

To prevent electron Landau damping from becoming more important than ion Landau damping we need to meet the criteria M. M. Oppenheim and Y. S. Dimant (2004)

$$\frac{\nu_{e,pic}}{\nu_{i,pic}} > 1. \tag{3.23}$$

This is the same as the inequality 2.46, but modified to simulated collisions.

To maintain quasi neutrality we need to meet the criteria M. M. Oppenheim and Y. S. Dimant (2004) Rosenberg and Chow (1998)

$$\frac{\omega_{pi,pic}}{\nu_{i,pic}} > 1 \tag{3.24}$$

3.4 Monte Carlo Collision Module

The Monte Carlo Collision module (MCC) used in PINC is based on the method outlined in Vahedi and Surendra (1995) a condensed explanation is given in Verboncoeur (2005).

In a simple collision model we could use a fixed probability for a particle to undergo a collision and then iterate over each particle and use this probability to either let it collide or not. The general idea behind the null-collision method is to precompute the maximum probability for any particle to undergo a collision and then use this probability to exclude a part of the total number of particles. Then we let the rest undergo collisions according to appropriate statistical measures. In this method we still let the same amount of particles collide, but the exclusion of a part of particles can lead to a significant speedup.

3.4.1 General Description Null-Collision Module

First we need to define a max probability P_{max} for any particle to undergo a collision within one time step. This max probability will then also be the maximum possible fraction of particles that undergo a collision within a time step. For one particle p the probability to undergo a collision is given by Verboncoeur (2005)

$$P_{max} = 1 - \exp(-\nu_p \Delta t) \tag{3.25}$$

For each species s we have the maximum possible probability to collide given by P_{max}

$$P_{max} = 1 - \exp(-\nu_{max} \Delta t) \tag{3.26}$$

P_{max} is now given by the largest collision frequency present for species s in the system, with ν_{max} being the greatest collision frequency for any particle, and is scaled by the simulation time step Δt. The method needs the maximum collision frequency in the system, so for each particle p we check its collision frequency ν_p, and find the greatest collision frequency by

$$\begin{aligned} \nu_p &= n_t(x)\sigma_T(\epsilon)v_p(\epsilon) \\ \nu_{max} &= max\{\nu_p\} \end{aligned} \tag{3.27}$$

Where $n_t(x)$ is the number density of the neutral particles, and $v_p(\epsilon)$ is the speed of the particle. If we assume uniform density, ν_{max} only depends on the kinetic energy ϵ. $\sigma_T(\epsilon)$ is the total collision cross section given by

$$\sigma_T(\epsilon) = \sigma_1(\epsilon) + \sigma_2(\epsilon) + ... + \sigma_{N_{type}}(\epsilon) \tag{3.28}$$

Where the subscript 1, 2, ..., N_{type} refers to collision types. In general we need to iterate over all particles to find the one with the maximum collision frequency to decide N_{coll},

with the exception of a constant collision frequency for all particles. We use P_{max} to select a portion of particles by

$$N_{coll} = N_p P_{max}, \tag{3.29}$$

which is the number of particles per species we check for collisions and N_p is the total number of particles. Excluding duplicate collisions for one particle, we pick N_{coll} particles and check them for collision types. For each particle the probability of a collision type n is given by P_n, and hence the total probability of a chosen particle to collide can be split into the following parts

$$P_{max} = P_{null} + P_1 + P_2 + \ldots + P_{N_{type}}, \tag{3.30}$$

where the subscript is the same as that in eq. 3.28, and refers to the number of a collision type. We have added a null collision probability P_{null} to make P_{max} constant for the colliding particles over the whole range of possible individual collision frequencies. P_{null} is the probability that a particle chosen to collide still does not collide. That means that if the particle we are evaluating has a collision frequency equal to ν_{max}, P_{null} would equal zero.

Finally we pick a random number $R \in [0, 1]$, and decide the type of collision according to

$$R \leq \nu_1/\nu_{max} \quad \Rightarrow \text{collision type 1} \tag{3.31}$$

$$\nu_1/\nu_{max} < R \leq (\nu_1 + \nu_2)/\nu_{max} \quad \Rightarrow \text{collision type 2} \tag{3.32}$$

$$\vdots \tag{3.33}$$

$$\sum_{j=1}^{N_{type}} \nu_j/\nu_{max} < R \quad \Rightarrow \text{null collision} \tag{3.34}$$

After the collision type is selected we change the velocity of the particle according to that collision type. The specific types used in this thesis are explained in subsequent sections.

3.4.2 Collision Geometry

Before we explain the collision types it is useful to define some variables.

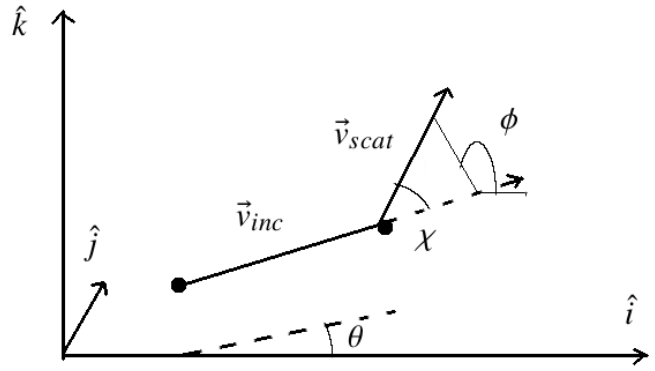

Figure 3.3: Geometry of a collision between a charged particle and a neutral. We have used the $\hat{i}, \hat{j}, \hat{k}$ notation, to denote unit vectors in the x, y, z spatial directions. χ, ϕ, are scattered angles, and θ is the angle between $\hat{i}$, and the projection of v_{inc} onto the $\hat{i}, \hat{j}$ plain.

The geometry given in fig 3.3 is the geometry used for elastic scattering. v_{inc} is the incident particle velocity, and v_{scat} is the scattered particle velocity. The angles χ and ϕ are scattered angles relative to the direction of v_{inc}. χ is often referred to as the scattering angle. ϕ is called the azimuthal scattering angle because it is the angle of rotation about the direction of v_{inc}.

3.4.3 Electron-Neutral Elastic Collision

For the collision types we use the general descriptions outlined in Vahedi and Surendra (1995) but with different formulations of the cross sections. We note that there is an underlying assumption that $M \gg m$, where M is the mass of the neutrals and m the mass of the electrons.

According to Vahedi and Surendra (1995) we can determine the scattering angle χ from approximate differential cross sections to produce the formulations

$$\cos(\chi) = \frac{2 + \epsilon - 2(1+\epsilon)^R}{\epsilon} \tag{3.35}$$

Where $R \in [0, 1]$ is a new random uniform number per collision event. For electrons we assume that $v_{electron} \gg v_{neutral}$ so that the neutrals are regarded as stationary compared to the neutrals. This means that the laboratory frame is the same as the center of mass frame. The azimuthal angle is uniformly distributed on the interval $[0, 2\pi]$ and is therefore determined by

$$\phi = 2\pi R. \tag{3.36}$$

We pick a new random number for this angle to be certain we avoid unphysical symmetries.

In the original paper from Surendra, Graves, and Jellum (1990) the electrons are fast moving with energies in the range 60-140 eV. For our purposes, where we are usually in the range of 0.1 eV. It might be better to use a uniform scattering on the interval $[0, \pi]$, but for now the implementation is done with the original scattering angles.

The relation between the velocity before the collision and after is given by geometric considerations by unit vectors parallel to the incident and scattered velocities by

$$\hat{\mathbf{v}}_{scat} = \hat{\mathbf{v}}_{inc} \cos\chi + \hat{\mathbf{v}}_{inc} \times \hat{\mathbf{i}} \frac{\sin\chi \sin\phi}{\sin\theta} + \hat{\mathbf{v}}_{inc} \times (\hat{\mathbf{i}} \times \hat{\mathbf{v}}_{inc}) \frac{\sin\chi \sin\phi}{\sin\theta} \tag{3.37}$$

Where θ is given by

$$\cos\theta = \hat{\mathbf{v}}_{inc} \cdot \hat{\mathbf{i}} \tag{3.38}$$

Scattered velocity components can then be determined by taking the projection of $\hat{\mathbf{v}}_{scat}$ on the coordinate axes.

The new speed is determined by the change in energy Vahedi and Surendra (1995)

$$\Delta\epsilon = \frac{2m}{M}(1 - \cos\chi) \tag{3.39}$$

and multiplied by the scattered unit vector. Again m is the electron mass, and M is the mass of the neutral.

3.4.4 Ion-neutral Elastic Collision

For ions the assumption we used for electrons, $v_{electron} \gg v_{neutral}$, can not be used. Thus, for each ion we need to transfer from a laboratory frame to the center of mass frame, let the ion collide, and transfer back to the laboratory frame. In practice this is done by picking a velocity at random from a Maxwellian Distribution, and using the difference between this velocity, and the particle velocity, to determine scattering angles. In the center of mass frame we use Θ as the scattering angle, and in the laboratory frame we use again χ as the scattering angle.

From energy considerations, and assuming scattering to be uniform and isotropic we get that the scattering angle is given by Vahedi and Surendra (1995)

$$\cos(\Theta) = 1 - 2R \tag{3.40}$$

In the center of mass frame, and

$$\cos(\chi) = \sqrt{1 - R} \tag{3.41}$$

in the laboratory frame. In theory, using any of these should yield the same answer, but cross sectional dependence on energy will make us have to transfer to the center of mass frame for each colliding ion. The change in energy of the incident particle is given by

$$\epsilon_{scat} = \epsilon_{inc} \cos^2(\chi) \tag{3.42}$$

which we can use to verify the implementation of the method. The azimuthal scattering angle is determined again with 3.36 and the scattered velocity components by 3.37, and 3.38.

3.4.5 Ion-Neutral Charge-Exchange Collision

In the charge-exchange collisions we still need to transfer to a center of mass frame since the type of collision is determined by incident energy according to eq. 3.31. If a particle is picked to undergo a charge-exchange collision we assume that one electron "hops" from the neutral to the ion. This is implemented by simply giving them each others velocities, or in the case where we do not track neutrals, giving the ion a new velocity picked from a Maxwellian distribution at the neutral species temperature T_N. These velocities have to be the same as the ones used to transfer frames.

3.4.6 Cross-Sections

For electron-neutral collisions, we used the model of Vahedi and Surendra (1995) which assumes $v_{electron} \gg v_{neutral}$, which does not transfer to the center-of-mass frame to compute the new velocity for the electrons. The assumption is actually not very well satisfied for ionospheric plasmas. However, since apparently no error has appeared due to this violation, the model is believed to work satisfactory. The alternative would be to use a center-of-mass frame with uniform scattering, and transfer back to the lab frame, as we do for the ions.

The different collision types outlined above are in PINC implemented in three different ways. Each model differs mainly by the implementation of the cross sections. Altough

earlier work Vahedi and Surendra (1995), Surendra, Graves, and Jellum (1990) uses more complicated models for the cross-sections, these models are made to work on different plasma regimes than we are currently studying. We therefore modify the original models and make them work on lower energy space-plasmas.

First we have a model for a constant collision frequency. This model simply takes a constant collision frequency and uses eq 3.26 and 3.29, to let all N_{coll} particles collide. This model has the advantage that if we wish to maintain a collision frequency, this will always be maintained. However, in many cases the constant collision frequency model might not make physical sense, since there is no dependency on energy. This also means that there are just as many slow moving particles that collide as fast moving particles, since every particle has the same probability to collide within a time step. (i.e no energy dependence of ν_p see eq. 3.25). This can, especially for electrons that always lose energy in a collision, lead to distortion of the distribution.

Secondly we have a model that uses a static cross section, with a collision frequency $\propto v$. This method is used in earlier work M. M. Oppenheim and Y. S. Dimant (2004) for simulating the Farley-Buneman instability, or in some cases a $\propto v^2$. Oppenheim M. M. and Dimant Y. S. (2013). The $\propto v$ model is probably the most physically correct one for cooler space plasmas as the collision frequency goes to zero as the speed of the particle goes to zero. (in Oppenheim M. M. and Dimant Y. S. (2013) they argue for the $\propto v^2$ model). It also lets more fast moving particles collide than slow ones on average. We decide the value of the cross section by solving eq 3.27 for σ_T to get

$$\sigma_{T,s} = \frac{\nu}{n_t v_{avg,s}} \tag{3.43}$$

and we use the average velocity for a species $v_{avg,s}$. For electrons $v_{avg,s}$ is the thermal velocity $v_{th,e}$, but for ions, because we transfer to the neutral frame of reference, we need to take into account the neutral thermal velocity, and thus we must use $v_{avg,s} = v_{th,i} + v_{th,n}$. Using this cross section we will maintain the collision frequency ν if the energy (temperature of the species) does not change significantly. However, if the temperature changes, the collision frequency and in turn the whole simulation may be incorrect.

Thirdly we have a model for a functional form of the cross-sections. We choose a function on the form

$$\sigma_{T,s} = \max\{\sigma_{T,s}\}\exp\left(-\frac{v_p^2}{v_{avg,s}^2}\right) \tag{3.44}$$

Here $\max\{\sigma_{T,s}\}$ is decided by eq 3.43 and is the largest cross section present at the velocity $v_{avg,s}$, and v_p is the particle speed. This function is only an educated guess,

but chosen such that the tipping point between rising collision frequency, and sloping collision frequency is at $v_{avg,s}$, and at this point the cross section is equal to $\max\{\sigma_{T,s}\}$. This function is implemented mostly for comparison, and not for physical simulations, as we wish to compare the two other models to a model that is roughly $\sim\propto v$ for slow particles, and $\sim\propto 1/v$ for fast particles. This is a topic for future work.

The $\propto v$ model is the de-facto standard as of the writing of this thesis. The functional model is an attempt at implementing a more physically correct cross section, as they usually are not linear functions of energy. However, since the functional form lacks proof of validity, we choose to run with the $\propto v$ model in every simulation presented in this thesis.

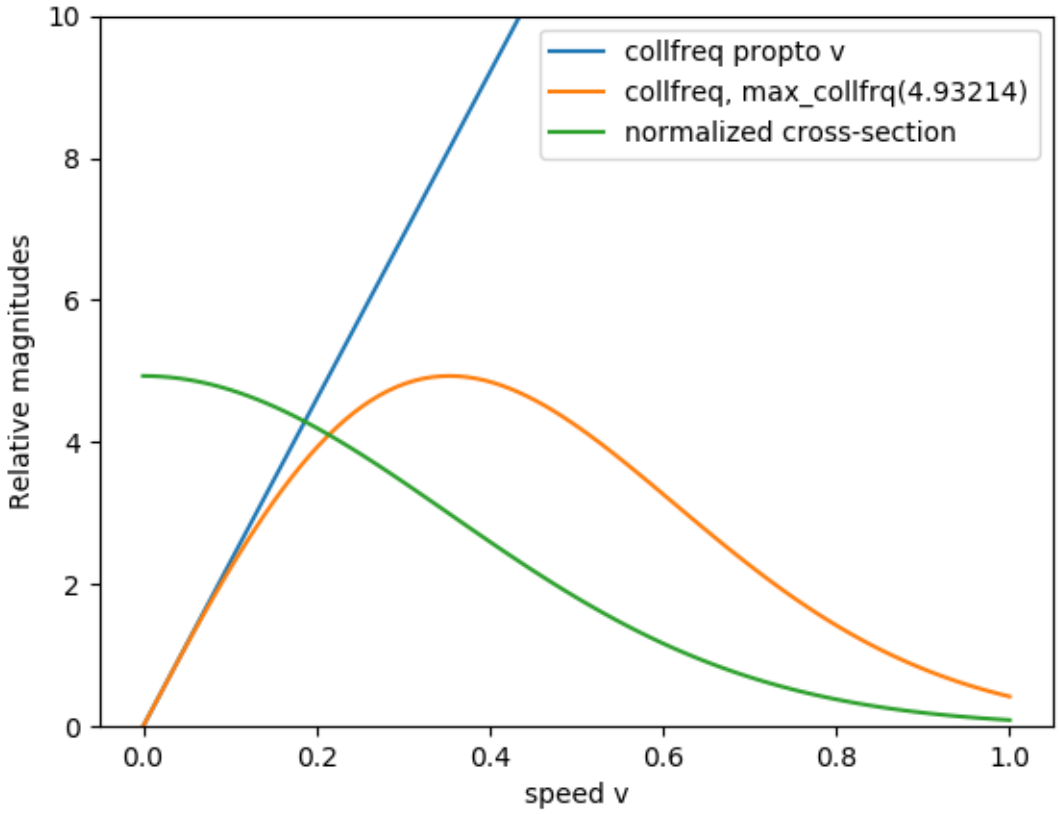

Figure 3.4: plot of the two models with varying collision frequency as a function of speed. The cross-section of the functional form model is plotted to see the form.

In fig 3.4 we have plotted the collision frequency as a function of speed for the two last cross-section models for $\max\{\sigma_{T,s}\} = \sigma_{T,s} = 0.5$ and $v_{avg,s} = 0.5$. We can see here how the two models are fairly similar for slow particles, but are different for fast

particles. It is possible in the functional form model to fit the parameters $\max\{\sigma_{T,s}\}$ and $v_{avg,s}$ to mimic real cross-sections for a type of particles if one knows what the maximum value of the cross-section for that given type is and at what value for $v_{avg,s}$ the cross-section should drop off.

3.5 Implementation In PINC

In this section we will go through in some detail the implementation of the collision method outlined above. For the past 4 years the PINC code has been developed from the ground - up to be a massively parallel, Particle-in-Cell code. Most of this work has been done as a part of Sigvald Marholms PHD, but several other people have been involved, as a part of their masters project. However, to study collisional plasmas, there was a need to implement a module that controls these collisions. This work was largely done as a part of this masters project, and we will therefore clarify the implementation details, and some choices made along the way.

Let us first quickly review what is needed in code in the collision module. First of all, we need one function for each cross-section model. These functions need to be able to pick a number decided by P_{max} of random particles, and decide the appropriate collision method (elastic, charge-exchange) for that particle. For each collision method we need some function to correctly update the velocity vector. The general idea and flow is shown in fig. 3.5

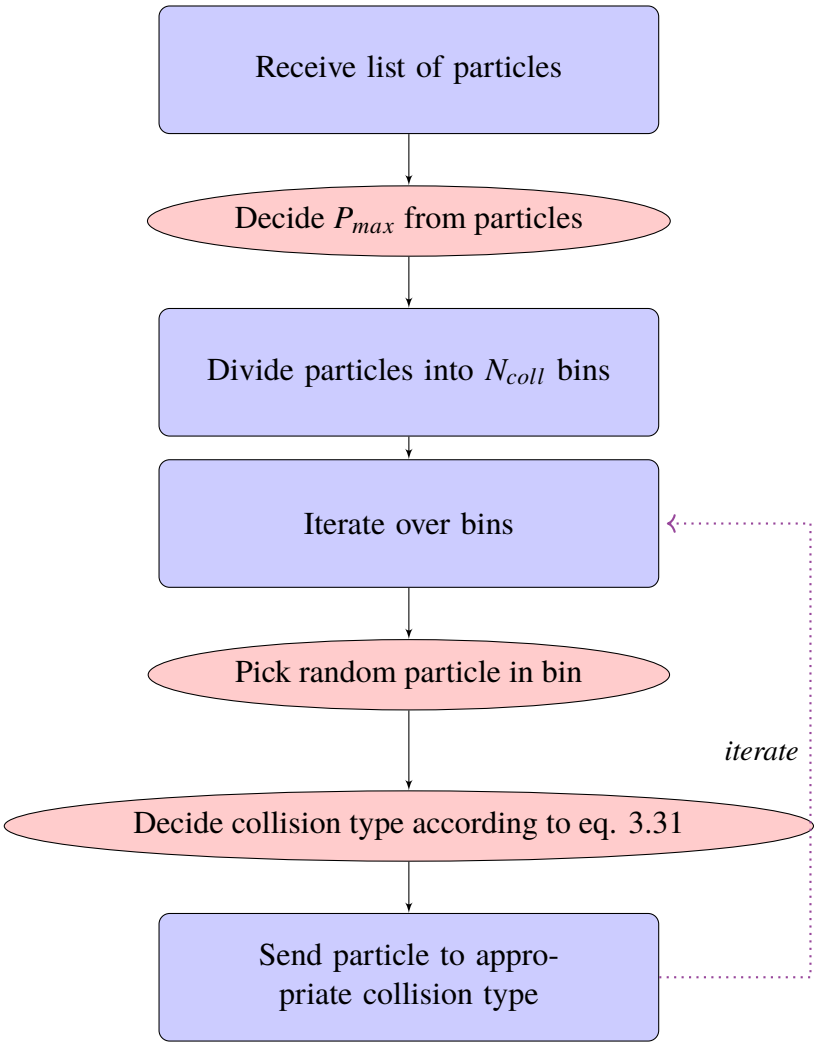

Figure 3.5: General flow of the collision functions. This will be done once for each time step, and charged specie.

In addition we need an initialization function to read input parameters from an input file, and a normalization function to normalize these input parameters. To make the code readable, and effective we also add functional pointers that point to the functions for each cross-section model, and choose which one to use from input at initialization.

3.5.1 Design Choices

We will here clarify some choices made along the way, which might impact the results.

We needed an effective way to avoid the same particle being selected for collision twice. The simplest way to do this would be to keep track of the particles that have

collided, and for each new particle that collides, check the list of collided particles. This would have been very slow, so instead we choose to use bins, and let one particle collide within each bin. This way, duplicates are automatically excluded, and we only need one iteration over the population.

Some earlier work M. M. Oppenheim and Y. S. Dimant (2004) has used a modified mass ratio of electrons to neutrals. This was done to get the correct dissipation value, which was determined to be 100 times larger. The reason why we need to modify the dissipation value is because the E-region is dominated by inelastic collisions, and the simulations in earlier work only use elastic collisions. To mimic the effects of inelastic collisions, the mass ratio of electron to neutral is therefore modified. To be able to compare our results with the previous work, this is also done in the collision module of PINC, and the value is controlled through the input file. Further studies on how large errors such approximations cause would be highly relevant.

3.5.2 The Collision Functions

The MCC module in PINC has three collision functions per species, one for each cross-section model. It also has a method handler (selects what functions to call based on input file), and its own normalization function.

The differences in the three collision functions per specie is only in how they select particles that collide, but they follow the same flow, we write a pseudo code in *C* style in the code block 3.6

The $Pmax...()$ functions are simple functions that gather the necessary variables for the specific specie and collision type, and decides P_{max} according to eq. 3.26, and ν_{max} if it is not constant.

The functions $mccGetMyCollFreq...()$ are also fairly simple functions that compute $\nu = n_t \sigma_T v$. For the case of a constant collision frequency these are not function calls, but simply read from input. The functions for the functional form model decides σ_T from an internal call to a separate function.

The if test at the end is the implementation of 3.31. Here we could add as many collision types as we wish. The line “if (Randomnumber<(MyCollFreq1+MyCollFreq2 + ...)/maxfreq...)” excludes the particles that fall within the null-collision probability P_{null} from the rest of the if tests. For the constant collision frequency model, this line can be removed, as we can let P_{max} absorb P_{null}, since they are both constants.

```
void mccCollide...(){

    ... define variables ...

  call to mccGetPmax...(); // updates Pmax and maxFreq

  int NparticleColl = Pmax*Nparticles;
  int mccStepSize = Nparticles / NparticleColl;

  for(long int i=specieStart;i<specieStop;i+=mccStepSize){

    ... pick new random numbers and decide index q of particle to
        collide ...

    double MyCollFreq1 = mccGetMyCollFreq...();
    double MyCollFreq2 = mccGetMyCollFreq...();
        ...


    if (Randomnumber0<(MyCollFreq1+MyCollFreq2 + ...)/maxfreq...){
      if(Randomnumber1 < MyCollFreq1/maxfreq...){
        // do one collision type e.g. elastic:
        scatter...();
      }
      if(Randomnumber2 < MyCollFreq2/maxfreq...
                && Randomnumber1 > MyCollFreq1/maxfreq...){
                ... next collision type
            }
    }
  }
}
```

Figure 3.6: A pseudo-code of the collision functions implemented in PINC

3.5.3 The Scatter Functions

As a start, it is implemented three scattering functions. We have elastic scattering for both ions, and electrons, and charge-exchange for ions. The charge-exchange is so simple that we don't need a dedicated function, but simply add

```
vx = vxN;
vy = vyN;
vz = vzN;
```

Where vx, vy, vz point to the x, y, z component of the velocity of the particle, and vxN, vyN, vzN is the velocity components of the neutral particle. These are picked from a normal distribution with standard deviation equal to the thermal velocity of the ions in one dimension.

For each collision the functions then call the scattering sub-functions $scatterIon$, and $scatterElectron$. These functions then use the different equations for energy, eq 3.35 for electrons, and eq 3.41 for ions, to determine the scattering angle χ, ϕ, and the relation angle θ by eq 3.36 and 3.38.

The implementation of eq 3.37 is done by precomputing each vector component

```
A = (sin(angleChi)*sin(anglePhi))/sin(angleTheta);
B = (sin(angleChi)*cos(anglePhi))/sin(angleTheta);
vx_ = (vx*cos(angleChi)+B*(vy*vy + vz*vz) );
vy_ = (vy*cos(angleChi)+A*vz-B*vx*vy);
vz_ = (vz*cos(angleChi)-A*vy-B*vx*vz);
```

Where A, B are placeholders for precomputation. After the scattered velocity components are determined the magnitude is determined using the new energy from eq 3.39 and 3.42, and the definition of kinetic energy $E_{kin} = \frac{1}{2} m_s v^2$, to relate energy to velocity.

3.5.4 MCC Initialization And Normalization

The collision module introduces some new variables in PINC, and since every variable in PINC is normalized to dimensionless variables, we need to normalize these new variables also.

First we need to make sure that we conserve the probabilities of a collision happening within a time step. The maximum probability is given by eq. 3.26, where in PINC time is normalized by the time step Δt. So the time step is equal to 1, and can be removed from eq. 3.26 if we dedimensionalize all frequencies by Δt, we can thus write a dimensionless collision frequency as

$$\tilde{\nu}_s = \nu_s \Delta t \tag{3.45}$$

If frequencies are defined by eq. 3.27, we need to normalize n_t, σ_T, v also. All velocities internally in PINC are normalized by $\Delta t/\Delta x$, so this is already taken care of. n_t can either be defined as the real density of neutrals, or the density of neutral super-particles, both would work as long as σ_T uses the same definition. We choose the latter, and thus the normalization is

$$\tilde{n}_t = n_t \frac{\Delta x^{ndims}}{W_1} \tag{3.46}$$

where W_1 is the weights of the ions, $ndims$ is the number of spatial dimensions, which must be 3 when using collisions. Assuming that the neutrals and ions have the same mass, and ions are specie 1 (electrons are specie 0), for σ_T we have

$$\tilde{\sigma}_T = \sigma_T \frac{W_1}{\Delta_x^2} \tag{3.47}$$

Normalization in PINC is subject to change, as it has changed in the past. The overall normalization scheme is developed and implemented by Sigvald Marholm, and follows a Lorentz-Heaviside normalization.

The MCC-specific variables are normalized by a call to function mccNormalize() which must be called at initialization. After this we call a function mccAlloc(), which reads the normalized values stored in a dictionary, and allocates them to a new data struct mccVars. This is done so we only need to handle the slow dictionary data type once during initialization, and that all MCC variables are available through a tidy syntax e.g variable=mccVars->$variable$, where $variable$ is the variable name in the struct.

3.6 Verification MCC

We first performed some simple tests in the collision functions implemented in PINC. The first one was a simple unit test that checked that the scattered unit vector was indeed a vector with unit size. The second unit test was to check if the change in energy of the particle was consistent with eq. 3.39 and 3.42. As another simple test of the implementation we plot the trajectory of the particle and verify that we have changes at discrete points, and that they don't look symmetric.

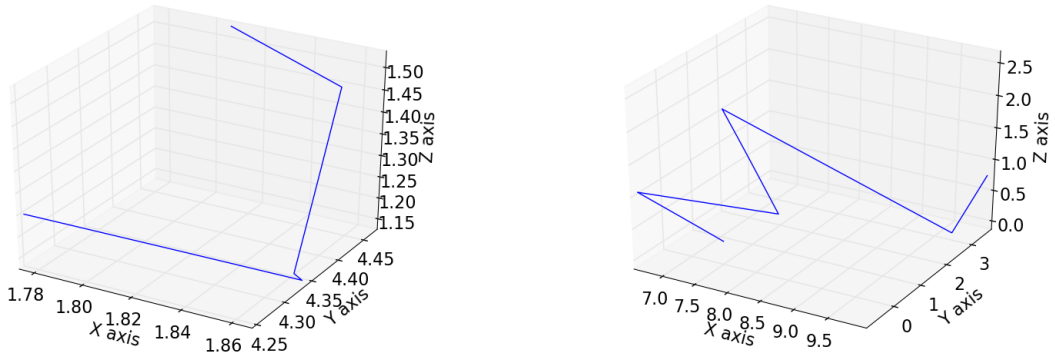

(a) trajectory of colliding ion

(b) trajectory of colliding electron

Figure 3.7: Plots showing trajectories of particles colliding with neutrals. The Plots are done in 3-D to verify that the collisions have semi random scattered components in each dimension.

We must also require the amount of collisions per time step to reflect the number defined by eq. 3.29. For the constant collision frequency model this is always satisfied. However, for the constant cross-section model, the number of collisions per time step is defined by the cross-section. Thus, we should check that we have the correct amount of collisions in the constant cross-section model. To do this we can set up a small simulation with $8 \times 8 \times 8$ grid with 420 particles per cell. In this case we used some typical values that lead to a time step of $0.1\omega_{pe} = 1.77e-8s$, and a high collision frequency of $400000s^{-1}$ for both species. Putting these numbers into eq. 3.29, we $N_{coll} = 758$ per time step.

Electron-elastic	Ion-elastic	Ion-charge-exchange	ions-both
769.7	510.8	255.4	766.2

Table 3.1: Number of collisions from a test case averaged over ten timesteps

We let $1/3$ of the ions collide with charge-exchange, and the rest as elastic collisions. We then ran ten time steps and averaged the number of collisions. In table 3.1 we see that the number of collisions performed on average by the collision model is in good agreement with the calculated value. The worst in this case was the electron-elastic collisions with an error of 1.5%. This is deemed sufficient, and we suspect the error to average out over more time steps.

3.6.1 Verification Using Change In Energies

As a more complete test I ran a series of test simulations in a warm plasma. The test is based on two assumptions, in the absence of any external forces,

1. when the background neutral gas has the same temperature as a specie, that given species temperature should not change (on average) over time.

2. When the background neutral gas has a different temperature than a specie, that given species temperature should converge towards the temperature of the gas.

We also expect the charge-exchange to converge faster than elastic collisions since the change in energy is equal to the difference between the ions and the neutrals. Moreover the convergence of the electrons should be slow compared to the ions as their energy change is low due to their low mass. In fact they will always converge towards zero since the model assumes $v_n \ll v_e$.

In the first test run we simulate a hot plasma where we let the neutral temperature be half that of the ions, $T_n = 0.5T_i$ with $T_i = 1000$K We run the test two times once with only ion-elastic collisions and once with only charge-exchange collisions. We initiate the system with a Maxwellian distribution, and uniform distribute the particles. The reason for this setup is that we wish to see the energy converge towards half that of the initial value. Additionally we want to see the ion distribution shift towards the neutral distribution at T_n.

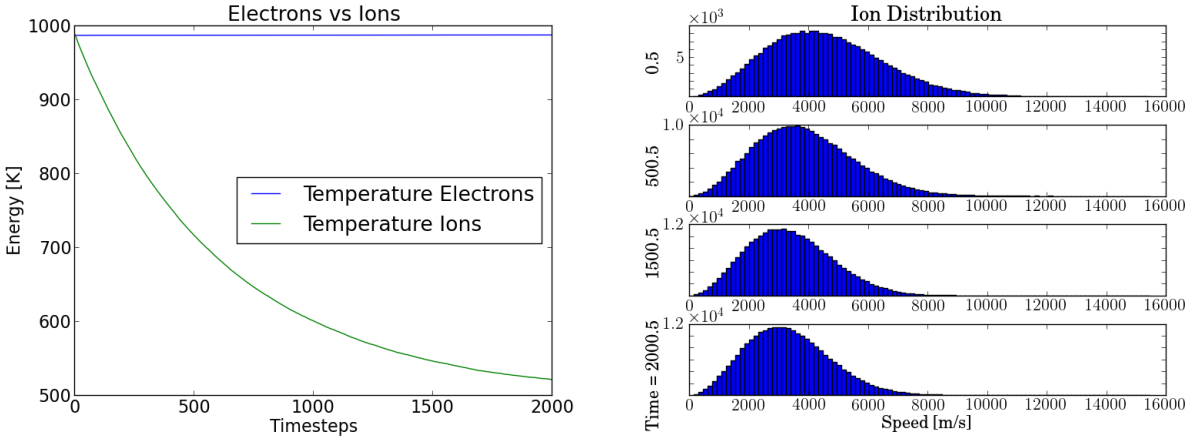

(a) Change in energy for both species over time. **(b)** Change in distribution for ions over time

Figure 3.8: Only ion elastic collisions are turned on. The initial temperature of the plasma is $T = 1000$K, and the neutrals have a temperature $T_n = 500$K. In a) values are average energies given in units of Kelvin. Figure b) shows the form of the distribution, values are relative to the number of particles in the simulation. From top to bottom time step = (0.5,500.5,1500.5,2000.5).

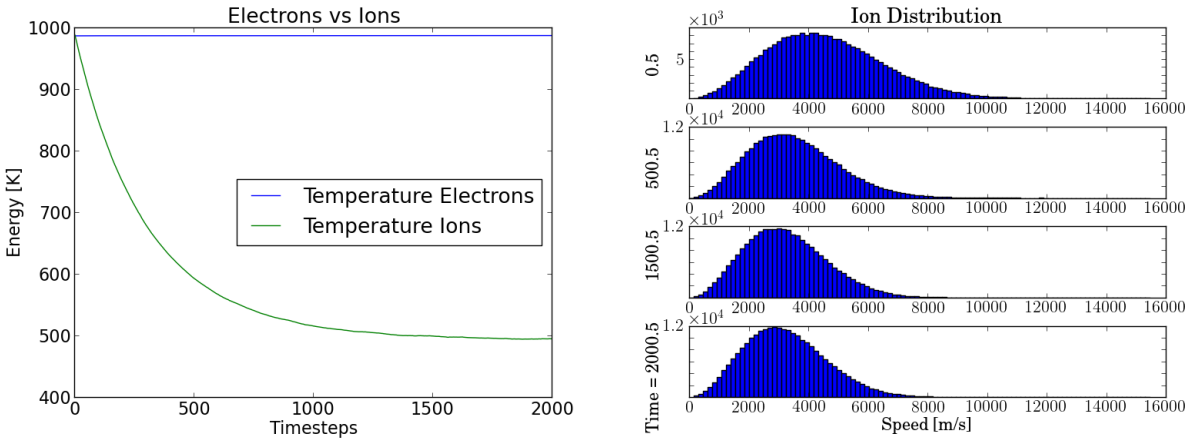

(a) Change in energy for both species over time **(b)** Change in distribution for ions over time

Figure 3.9: Only charge-exchange collisions are turned on. The initial temperature of the plasma is $T = 1000$K, and the neutrals have a temperature $T_n = 500$K. In a) values are average kinetic energies given in units of Kelvin. Figure b) shows the form of the distribution, values are relative to the number of particles in the simulation. From top to bottom time step = (0.5,500.5,1500.5,2000.5).

In fig 3.8 a) we see the result of the first test run. We ran with only ion-elastic collisions,

and as expected the energy level seems to converge towards $T_i = 500$K. In fig. 3.8 b) we see the distribution getting compressed, but it keeps the Maxwellian form. In the plots of the vx, vy, vz distributions we see the same compression of the distributions. We also see that there are no unphysical asymmetries introduced by the collisions. plots of the vx, vy, vz distributions are given in the appendix (A.1).

In fig 3.9 where we turned off ion-elastic collisions, and ran only with charge-exchange collisions, we see the same convergence towards $T_i = 500$K. Also, as expected at a faster rate. Again we see the same compression of the distribution.

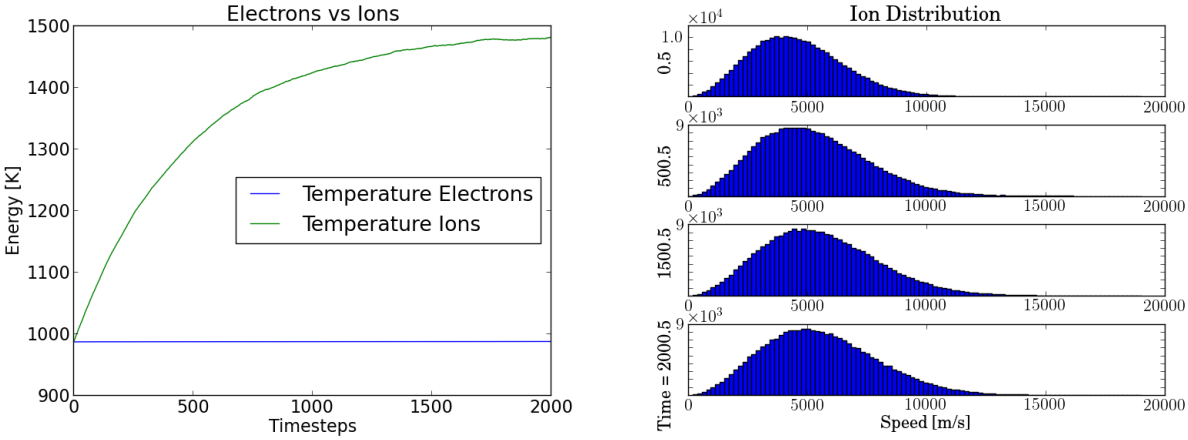

(a) Change in energy for both species over time

(b) Change in distribution for ions over time

Figure 3.10: Only ion elastic collisions are turned on. The initial temperature of the plasma is $T = 1000$K, and the neutrals have a temperature $T_n = 1500$K. In a) values are average kinetic energies given in units of Kelvin. Figure b) shows the form of the distribution, values are relative to the number of particles in the simulation. From top to bottom time step = (0.5,500.5,1500.5,2000.5).

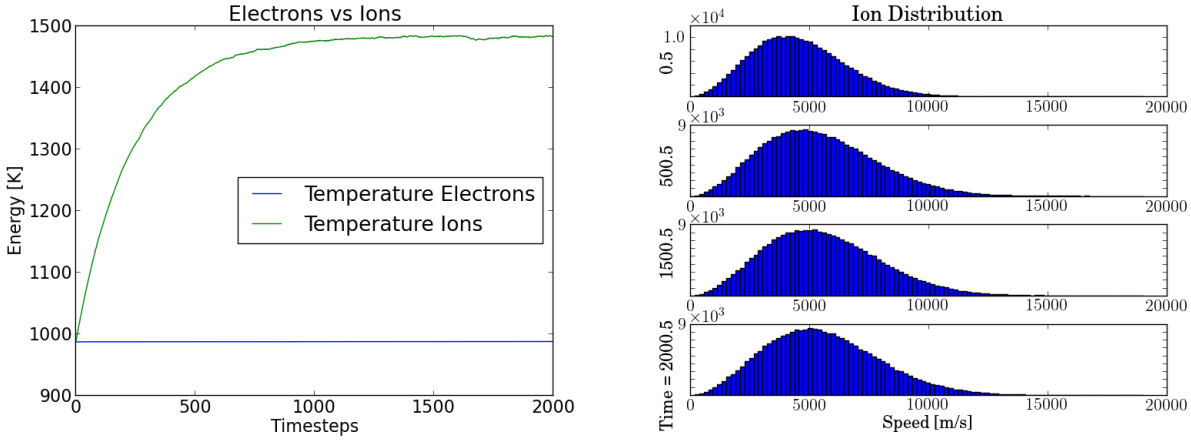

(a) Change in energy for both species over time

(b) Change in distribution for ions over time

Figure 3.11: Only charge-exchange collisions are turned on.The initial temperature of the plasma is $T = 1000$K, and the neutrals have a temperature $T_n = 1500$K. In a) values are average kinetic energies given in units of Kelvin. Figure b) shows the form of the distribution, values are relative to the number of particles in the simulation. From top to bottom time step = (0.5,500.5,1500.5,2000.5).

Next we ran the test with $T_n = 1500$K, and $T_i = 1000$K. This test run is similar to the previous two runs, but we wish to see the energy go up, to exclude the possibility of the energy only being able to drop for the ions.

The results of these runs are seen in fig 3.10, and fig 3.11. In the a) plots we see how the convergence has the exact opposite form of the ones in fig 3.8, and 3.9. If the rate of change where different in these two sets of runs there would have been a problem, but as we see the rate of change is the same, but slightly faster for charge-exchange in both cases. The vx, vy, vz distributions are given in the appendix (fig A.2), and are subject to a widening over time. This is expected as the Gaussian form should be conserved, and not have a spike at one point. We also see vx, vy, vz distributions that there are no unphysical asymmetries.

For the electron-elastic collisions, since they will not converge, we will have to look for asymmetries in the distribution. We also know that the energy should drop, and not rise. To be sure that this is the case, we use a neutral temperature of $T_n = 1500$K. The vx, vy, vz distributions are again given in the appendix (fig. A.2), and show no asymmetries.

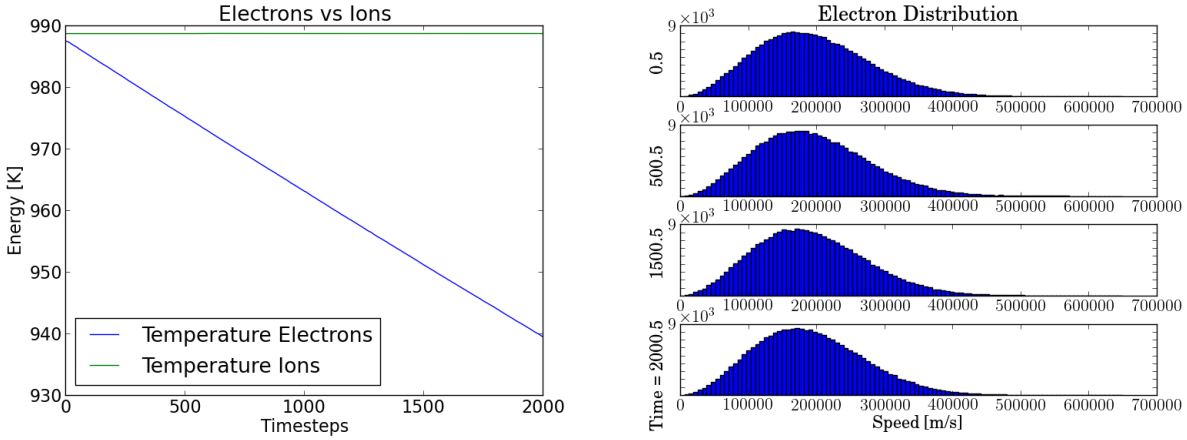

(a) energy for both species

(b) distribution for electrons

Figure 3.12: Only electron-elastic collisions are turned on. The initial temperature of the plasma is $T = 1000$K, and the neutrals have a temperature $T_n = 1500$K. In a) values are average kinetic energies given in units of Kelvin. Figure b) shows the form of the distribution, values are relative to the number of particles in the simulation. From top to bottom time step = (0.5,500.5,1500.5,2000.5).

Because the neutral mass is massive compared to the electrons $m_n \ll m_e$ the rate of change is expected to be small compared to rate of change for the ions. In addition, because the collision module assumes the speed of the electrons to be large compared to the neutrals $v_i \gg v_n$, the energy should always drop. in fig. 3.12 a) we see this expected behaviour, where the energy drops at a constant rate, but slower than for the ions. The distributions in b) seem constant, which they should on these timescales, but as we will see in the next test, on a longer timescale these will also be slightly compressed.

As a final run of this type, we now let $T_n = T_i$, and run 10000 time steps, to investigate the behaviour on longer timescales.

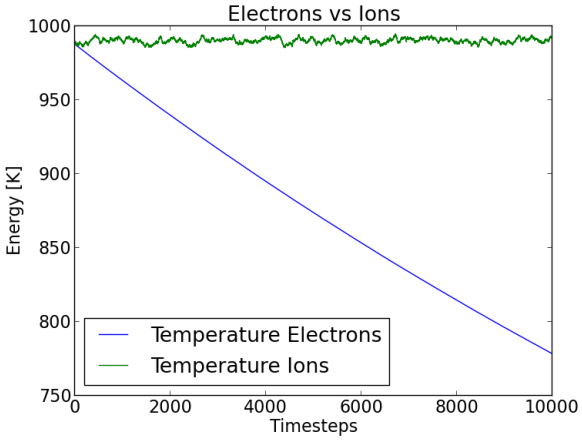

(a) Change in energy for both species

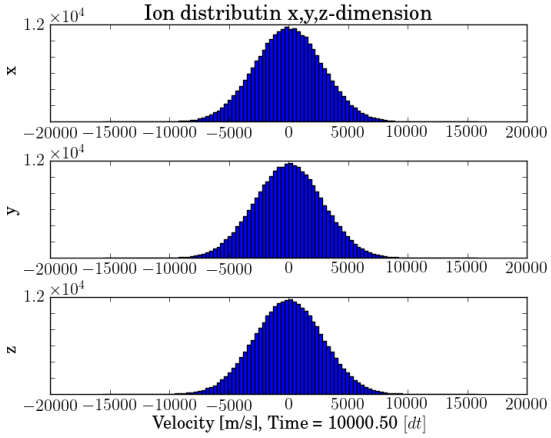

(b) Final vx,vy,vz distribution for electrons

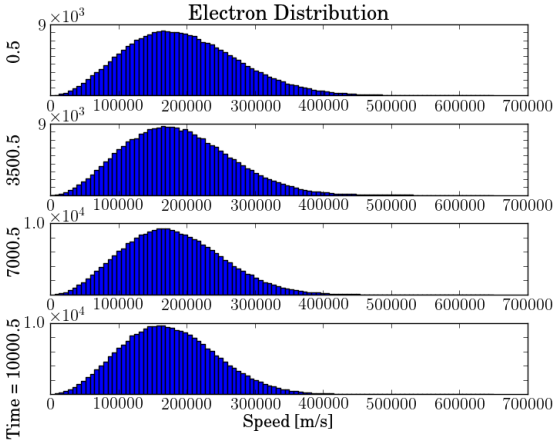

(c) Electron distributions

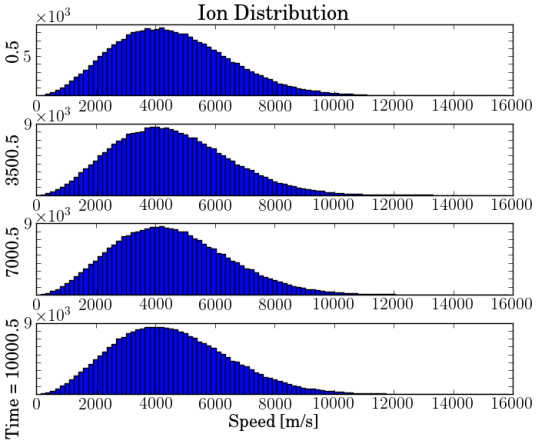

(d) Ion distributions

Figure 3.13: All collisions are turned on, and the test is run for an extended period. The initial temperature of the plasma is $T = 1000$K, and the neutrals have a temperature $T_n = 1000$K. In a) values are average kinetic energies given in units of Kelvin. In figure b) the final distribution of ions are given in v_x, v_y, v_z space. Figure c),d) shows the form of the distributions for both species. Values are relative to the number of particles in the simulation. From top to bottom time step = (0.5,3500.5,7500.5,10000.5).

In fig. 3.13 a) we see that the energy is not kept exactly constant as the collisions will randomly add and subtract energy to the particles when the neutral temperature is the same. However, on average the energy is more or less constant, as expected. In fig. 3.13 b) we choose to show the vx, vy, vz distribution of the electrons as this is the one that changed the most. The ion distributions are given in the appendix (A.4). In fig. 3.13 c), and d) we also see that the distributions keep their form, and no asymmetries

build up even on a long timescale.

Finally, as an extreme case, we change the initial state of the system by giving every particle exactly the same speed, but still let $T_n = T_i$, and the other parameters are as before.

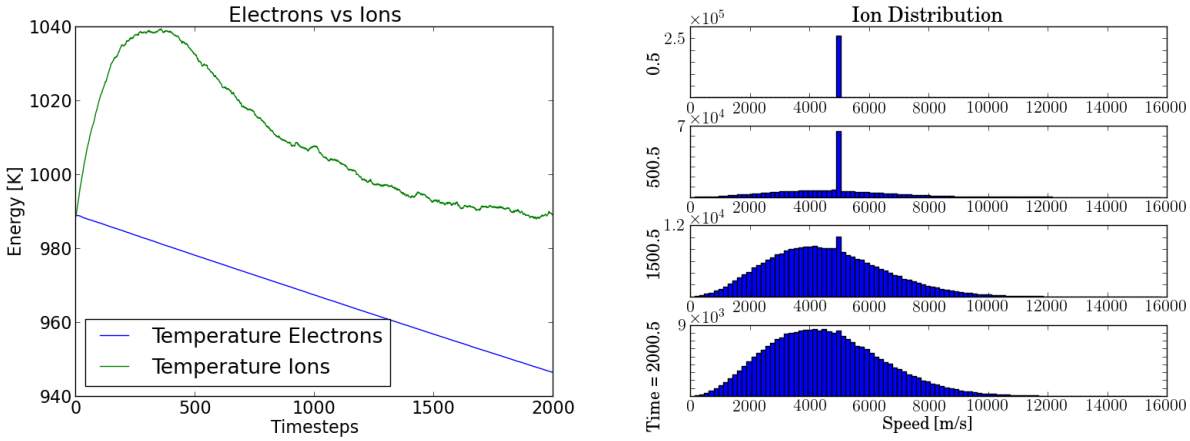

(a) **(b)**

Figure 3.14

To stress-test we ran this setup with only ion-elastic collisions, as charge-exchange collisions are simpler. In fig 3.14 we see how the Maxwellian distribution grows from collisions. The temperature increases initially, but this is believed to be because of the non-Maxwellian form of the distribution. However the energy seems to stabilize close to T_n, as expected. See also appendix fig. A.5 for v_x, v_y, v_z distributions.

3.7 Simulation Setup

In all simulation runs presented in this thesis we used the geometry shown schematically in fig. 3.15. We have chosen for the first set of simulations to run with a symmetric geometry, where the length of the simulated box is the same in every spatial direction $L_x = L_y = L_z$.

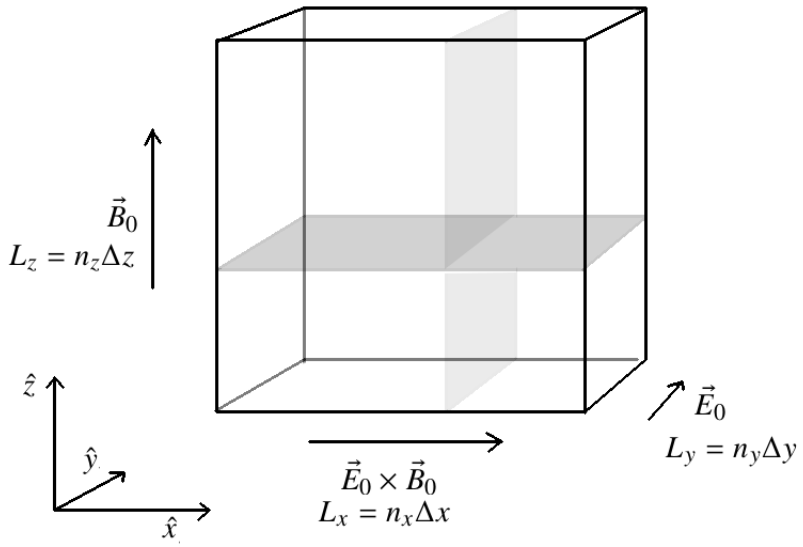

Figure 3.15: Figure showing the geometry of the simulation setup. The box length in the three dimensions is given by $L_i = n_i \Delta i$, where $i = x, y, z$. n_i is the number of spatial grid points in dimension i, and Δi is the step length between the grid points. Most figures are plotted on the $x - y$ plane shown by the darker gray rectangle. The light gray rectangle represents the expected plane where an FB wave will grow.

We expect plane waves to grow in the $y - z$ plane, and that they move in the $\vec{E}_0 \times \vec{B}_0$, $\hat{x}$ direction. these are represented by the light gray rectangle. Most of the data plots are performed in the $x - y$ direction, represented by the darker gray rectangle.

The first simulation presented in the Results chapter of this thesis has parameters based on M. M. Oppenheim and Y. S. Dimant (2004). We call this simulation the Baseline simulation. The Baseline simulation has parameters typical for the lower E-region ionosphere. In order to have a simulation to compare this one to, we also set up a simulation with modified driving electric field, external magnetic field, and collision frequencies for both species. We call this simulation the Optional simulation. The initial idea of the Optional simulation was that conserving the Hall and Pedersen conductivities should lead to the same FB-instability growth. Although this initial idea was somewhat flawed, it turned out to be an excellent simulation for comparison. We can outline the general idea as follows

In order to conserve the Pedersen and Hall conductivity (or drift rates) we need to modify the collision frequencies and the external magnetic field. From H. Pécseli (2012) chpt. 8.9 the total current density in a plasma with neutral collisions is

$$\begin{aligned} \vec{J}_\perp &\equiv \sigma_P \vec{E} + \sigma_H \vec{E} \times \vec{\hat{b}} \\ J_\parallel &\equiv \sigma_\parallel E_\parallel \end{aligned} \tag{3.48}$$

and the Pedersen and Hall conductivities are given by

$$\begin{aligned} \sigma_P \equiv \frac{en}{B}(\alpha_i - \alpha_e) \quad \text{and} \quad \sigma_H \equiv \frac{en}{B}(\beta_i - \beta_e) \\ \text{with} \\ \alpha_s \equiv \frac{\nu/\Omega_s}{1 + \nu_s^2/\Omega_s^2} \quad \text{and} \quad \beta_s \equiv \frac{1}{1 + \nu_s^2/\Omega_s^2} \end{aligned} \tag{3.49}$$

where Ω_s is the cyclotron frequency and ν_s is the collision frequency, and the subscript s denoting the species, which in this case are ions and electrons. To be able to increase the spatial step length in the simulations we need to lower the magnetic field, so we see that to maintain the conductivities we need to conserve the quantity ν_s/Ω_s. This means that if we multiply $\Omega_s = qB/m_s$ (the magnetic field) by a factor ζ, we need to multiply ν_s by the same factor. We can also see that to conserve the current density $J_\perp \propto E/B$, we also need to multiply E by the same factor ζ. There is one caveat however, $\sigma_\parallel \equiv e^2 n[1/(m_i\nu_i) + 1/(m_e\nu_e)]$ has also changed with a factor $1/\zeta$. This implies that we should extend the box length in the $B_\parallel$ direction if parallel effects are of importance.

In general the growth rate should be comparable using the method of modifying the Hall and Pedersen conductivities(slightly higher due to the ion collision frequency being lowered), but the modification of the ion collision frequency means that the ion mean free path is longer, and thus the optimum wavelength is expected to be longer, and if the optimum wavelength is longer the growth is lower. See the appendix (B) for some further explanation.

For the first set of simulations presented in the results we choose to simulate the smallest possible system where we still could expect waves. The Baseline parameters are based on the lower E-region ionosphere, where we know from observations that there should be a significant wave component at $\sim 3m$. Because of electron gyration the step length is $\Delta_x = 0.04m$. (the same as in M. M. Oppenheim and Y. S. Dimant (2004) and therefore we choose $L_x = L_y = L_z = 128\Delta_x = 5.12m$. The Optional simulation has a lowered magnetic field so we can increase the step length and still resolve the electron gyration. We should still require $L_x, L_y > r_{g,i} \approx 6m$. In the Optional simulation we used $\delta_x = 0.08m$ and $L_x = L_y = L_z = 128\Delta_x = 10.24m$.

Both simulations used an elevated electron mass. This is justified by keeping the Pedersen drift rates the same M. M. Oppenheim and Y. S. Dimant (2004), M. M.

Oppenheim, Y. Dimant, and Dyrud (2008), and Oppenheim M. M. and Dimant Y. S. (2013). In practice this means that the collision frequency of the electrons needs to be scaled by the inverse factor of the mass. (see eq. 3.22). This argument is the same as the above argument of conserving the drift rates, but here it is used to elevate the electron mass. In the case of elevated electron mass however, the ion collision frequency remains the same, and we can thus expect exactly the same physics. The electron mass can not be elevated too much, as the scaling of the collision frequency can lead to damping of waves. We can also lower the density n_0 since the dominant linear effect does not depend on density, only the normalized density gradient. However it can not drop to low as this will break quasi neutrality. 3.24. Rosenberg and Chow (1998). The initial mass ratio used was that of a NO^+ plasma with $m_i/m_e \approx 50.000$, but the increased electron mass bring it closer to a H^+ plasma.

The collision module uses an artificially lowered neutral mass for the electrons-neutral collisions. This is reasoned by the fact that the plasma region simulated is dominated by inelastic collisions, while the simulator only simulates elastic collisions. So to mimic the effect of inelastic collisions we artificially raise the diffusion rate. M. M. Oppenheim and Y. S. Dimant (2004) and Oppenheim M. M. and Dimant Y. S. (2013) use an elevated diffusion rate of 100, this is based on observational data Gurevich (1978). In the present simulations we have used a more modest value of 10.

3.8 Data Analysis Tools

In this section we present some details about the methods used for the analysis of data in this thesis.

3.8.1 Electric Field

The average electric field values are obtained by summing over the whole grid (absolute values) and dividing by the number of grid points

$$E_{avg} = \sum_i \sum_j \sum_k \sqrt{Ex^2_{i,j,k} + Ey^2_{i,j,k} + Ez^2_{i,j,k}}/(n_i + n_j + n_k) \tag{3.50}$$

Here i,j,k is the indices of the discrete grid points in the spatial dimensions x,y,z. This is done at every 100 time steps, which makes this fairly computationally heavy. The maximum values are found using a “if” test in the i,j,k loop, and storing the value if it is larger than the previous.

3.8.2 Fourier Transforms

We present spectral plots of the $k_x - k_y$ domain for the electric field. The plots are produced by taking the absolute value $a_{i,j} = \sqrt{Ex^2_{i,j,k} + Ey^2_{i,j,k} + Ez^2_{i,j,k}}$ at each discrete grid point i,j and a chosen value of k. We compare these plots with the 2-D Fourier transform in the $x - y$ plane (indices i,j) using numpy's built in 2-D FFT function numpy.fft.fft2(). Numpy uses the definition of a 2-D fft2

$$A_{l,m} = \sum_{i=0}^{I-1} \sum_{j=0}^{J-1} a_{i,j} \exp -2\pi i \left(\frac{il}{I} + \frac{jm}{J} \right);\ l = 0, ..., I-1;\ m = 0, ..., J-1, \tag{3.51}$$

where I is the number of grid points in the x direction, and J is the number of grid points in the y direction.

3.8.3 Temperatures

Analyzing the energy level of the system is done by computing an effective temperature. The temperature is found by summing up all particle kinetic energies and dividing by the total number of particles and the Boltzmann constant.

$$\begin{aligned} T_{s,r} =& \frac{1}{k_b N_{s,p}} \sum_{p=0}^{N_{s,p}-1} \frac{1}{2} m_s \sqrt{v^2_{p,r}}\,, \\ T_{s,tot} =& T_{s,x} + T_{s,y} + T_{s,z} \end{aligned} \tag{3.52}$$

where k_b is the Boltzmann constant, and $N_{s,p}$ is the number of particles for specie s. The subscript r indicates the spatial direction x,y,z.

3.9 Scale of FB Simulations

We have mentioned earlier that the Farley-Buneman instability is inherently difficult to simulate due to the time and length scales involved. We will clarify this statement with an example. Using eq 2.5, and typical E-region values (from table Baseline simulation), we get $\lambda_D = 0.0378$m, and to resolve the Debye length we set the step length $\Delta_x, \Delta_y, \Delta_z = 0.04$m. To accurately simulate the wave physics, we in general need the $L_r > \lambda_r$, where $\lambda_r = 2\pi/k_r$ is the wavelength in the spatial r direction. As a

best case we can use a box that is two times as large. We know from radar data that there exists waves at 3,6 and 15 m. Simulating all of these we should require a 30m long box, meaning that we need $n_i = 30\text{m}/0.04\text{m} = 750$ grid points along the x, and y axes. For the grid points in the z direction it is a "the more the better" case. The issue here is the $k_{||}$ in eq. 2.37. This parameter says that the wave growth is impacted by the wave length in the z direction, and it will tend to dampen waves if it is not long enough ($k_{||}$ small enough). To be reasonable we use $L_z = 2L_x$, so we need $n_z = 1500$. PINC has shown that it can run a $32 \times 32 \times 32$ simulation reasonably fast, and a $64 \times 64 \times 64$ simulation at acceptable speed on one core. Assuming that PINC scales linearly that means we need $(750 \times 750 \times 1500)/(64 \times 64 \times 64) = 3218$ CPU's at a minimum, or $(750 \times 750 \times 1500)/(32 \times 32 \times 32) = 25749$ CPU's if we need speed. This is the best case to barely capture (probably) all of the physics.

Chapter 4

Results

4.1 FB Instability - Simulation Runs

In this section we will present four FB-instability simulations. The two first we have called the Baseline simulation and Optional simulation, and the second two we have called the Baseline Lowered and Optional Lowered, due to them having a lowered driving electric field. Our Baseline simulation is based on the 2-D simulation of M. M. Oppenheim and Y. S. Dimant (2004). We will compare this simulation to a modified simulation which we call the Optional simulation. The Baseline simulation uses input parameters typical of the lower E-region ($\sim$ 101 km high latitude) to produce Farley-Buneman instabilities (type 1). See section 3.7 for more details.

The Baseline and Optional simulations are expected to produce similar physics according to linear theory. The main idea is to retain the physics by conserving the Pedersen and Hall conductivities. There are several reasons why we wish to run two simulations in this manner. First, as we will see, it is possible to run a simulation on a larger physical domain at the same computational cost. Secondly, comparing physical quantities in these two might gain some insight to the driving mechanisms of the Farley-Buneman instability. Thirdly, we are able to run similar simulations where the collision frequencies are different. This is important to be able to put the simulations in the context of the new collision module, and further verify its validity.

4.1.1 Comparing Baseline To Optional Run

Imposing the idea in sect 3.7 we get two sets of simulation parameters

Parameter	Value
$timesteps$	25000
dt	3×10^{-6} s
dx, dy, dz	0.04 m
n_x, n_y, n_z	128
n_0	1×10^9 1/m^3
m_e	4×10^{-29} kg
m_i	5×10^{-26} kg
$\vec{B}_0$	$[0, 0, 5 \times 10^{-5}]$ T
$\vec{E}_0$	$[0, 0.1, 0]$ V/m
ν_e	2800 1/s
ν_i	1800 1/s
q	$\pm 1.602 \times 10^{-26}$ C
$v_{th,e}$	10175 m/s
$v_{th,i}$	288 m/s
$n_{s,sim}$	420 pc

(a) Baseline simulation

Parameter	Value
$timesteps$	80000
dt	3×10^{-6} s
dx, dy, dz	0.08 m
n_x, n_y, n_z	128
n_0	1×10^9 1/m^3
m_e	4×10^{-29} kg
m_i	5×10^{-26} kg
$\vec{B}_0$	$[0, 0, 1.5 \times 10^{-5}]$ T
$\vec{E}_0$	$[0, 0.03, 0]$ V/m
ν_e	840 1/s
ν_i	540 1/s
q	$\pm 1.602 \times 10^{-26}$ C
$v_{th,e}$	10175 m/s
$v_{th,i}$	288 m/s
$n_{s,sim}$	420 pc

(b) Optional simulation

Table 4.1: Simulation parameters. The Optional simulation has a larger step length in space (dx,dy,dz). this is obtained through modification of the driving electric field E_0, external magnetic field B_0, and the collision frequencies ν_e, ν_i.

The density of the electrons and ions are the same as that of the neutral specie n_0, where the simulated particle number is 420 per cell. The thermal velocities where decided assuming all species having the same temperature $300K$. As explained in the section 3.7 the simulations use an elevated electron mass, and the neutral mass is modified in electron-neutral collisions to mimic the effect of inelastic collisions. In this simulation, and the next two it was used the $\nu \propto v$ (i.e constant cross-section) collisional model. This is the same model that is used in most cases by M. M. Oppenheim and Y. S. Dimant (2004) and described in section 3.4. The Optional simulation used a larger number of time steps such that we simulate the same amount of ion gyro periods Ω_i.

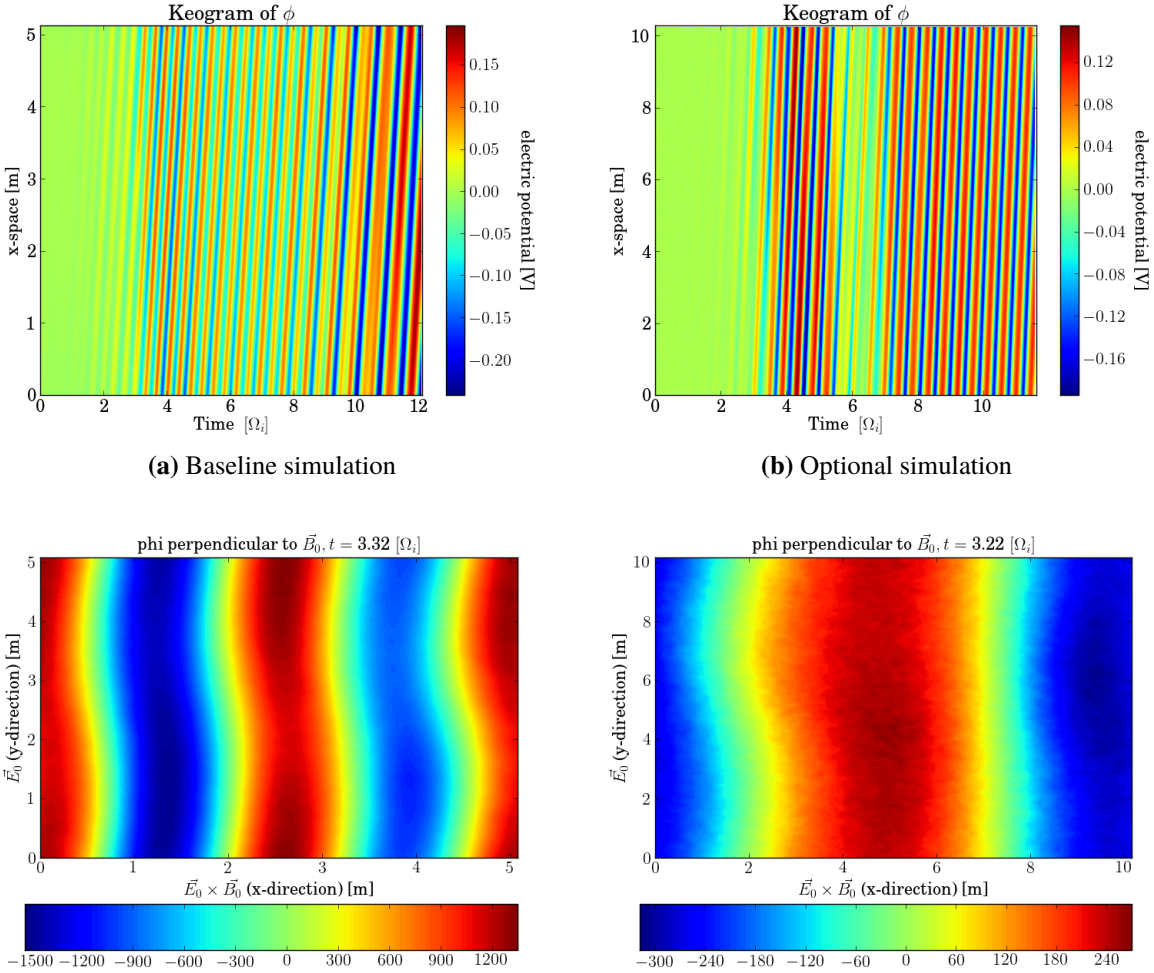

(a) Baseline simulation

(b) Optional simulation

(c) Baseline simulation

(d) Optional simulation

Figure 4.1: a) and b) are keograms of a slice in x-direction for each time step. The slice is of the ϕ (electric potential) grid. c) and d) are plots of the potential ϕ during the linear growth phase. The potential values are given in dimensionless PINC values, and are added only for reference.

The keograms in fig 4.1 a) and b) are produced by picking a line along the electric potential ϕ grid in the respective directions for each time step and appending them to an array. A simple plot of the array for one of the spatial dimensions show the development of the waves in time. In fig. 4.1 c) and d) we see a slice of the $x - y$ plane of the ϕ grid during the linear growth phase. Both simulations show many of the same features, but also some notable differences. In the Baseline simulation waves seem to build from shorter wavelengths. Around the time the peak amplitude is reached shorter waves transform into longer wavelengths roughly proportional to the box length. The Optional simulation does not appear to do this, instead it features the same wavelengths

from the onset til the end, where the wavelength is constantly proportional to the box length. Time seems to scale fairly linearly with Ω_i, the ion gyro period.

Insight into the difference in behaviour of the wavelengths can be gained from calculating some estimates for the optimum wavelength. We use the definition of mean free path

$$l_i = \frac{v_{th,i}}{\nu_i}, \tag{4.1}$$

and the RMS value for the thermal velocity $T_i = \sqrt{(3k_bT_i)/m_i}$. The rest of the values are given in table 4.1

	Baseline	Optional
Mean-free path	0.32 m	1.07 m
eq. 2.51	3.11 m	10.37 m

Table 4.2: Calculated values of the wavelength for the baseline and optional simulation.

From table 4.2 we see that the simple estimate of the wavelength being comparable to a few ion mean-free paths gives a rough estimate that is comparable to the simulation results. However, the estimates given from the model of Yakov S. Dimant and Meers M. Oppenheim (2003) eq. 2.51 is in excellent agreement with the wavelengths seen during the linear growth phase.

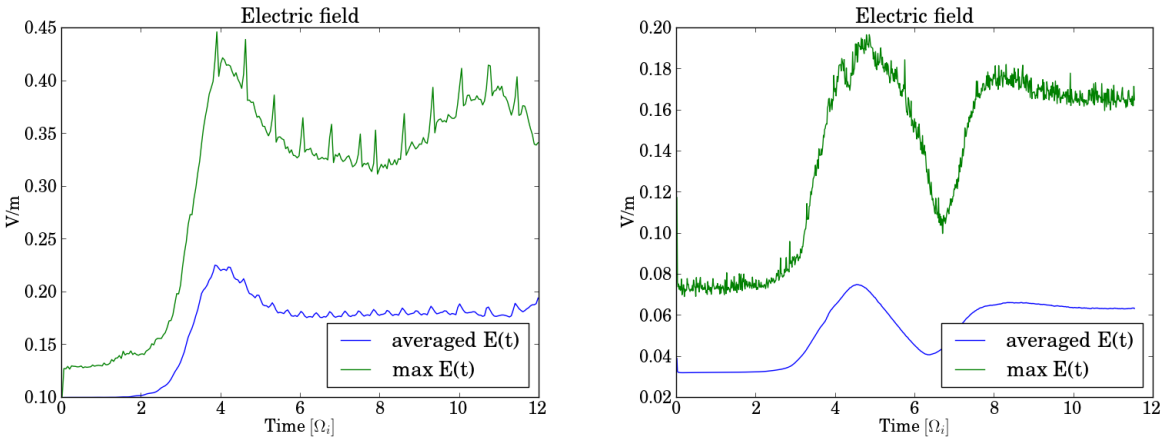

(a) Baseline **(b)** Optional

Figure 4.2: Electric field average and max values plotted in time. Time is scaled with Ω_i since physics seems to scale with this value.

Next, we look at the overall behaviour of the electric field. In 4.2 there is a plot of the electric field average values, and max values, for both simulations. We can note that the overall shape in the plots are similar. However, the baseline simulation has some periodic spikes in both the average and maximum values. The Optional simulation has a dip after the linear growth phase, at around $6\Omega_i$.

To see how close the Baseline, and Optional simulation are to each other we can compute some relative values for the electric field. If everything scales linearly, multiplying electric field values from the Baseline simulation with the scaling factor (sect. 3.7) should yield the same values as we see in the Optional simulation. In fig. 4.2 a) the peak average value is 0.23 V/m. Multiplying this by the scaling factor 0.3 (e.g $B_{0,Optional}/B_{0,Baseline}$), gives 0.23 V/m $\cdot$ 0.3 = 0.069 V/m, and the system stabilizes at a value of 0.18 V/m. Multiplying this by the scaling factor we get 0.18 V/m $\cdot$0.3 = 0.054 V/m. These values are slightly lower than the ones in fig. 4.2 b). This result is somewhat counter intuitive since the linear growth $\gamma_{Optional} = (1/0.3) \cdot \gamma_{Baseline}$ is scaled oposite for a given wave number k. This could suggests that the growth should be larger for the Optional simulation, according to the linear theory. This, of course, is only true if we neglect the difference in wavelength. If we input the last values from table 4.2 and scale the growth with Ω_i we get $\gamma_{Baseline} = 5.7$, and $\gamma_{Optional} = 0.8$. This also explains the lower peak values in the Optional simulation mentioned earlier.

It is reasonable to require $E_{sat} \gg E_{init} \gg E_{noise}$. Where E_{sat} is the saturated average electric field due to the density perturbations. E_{init} is the initial average field.

	E_{sat}/E_0	E_{sat}/E_{init}	E_{sat}/E_{noise}
Baseline	1.8	1.8	3.69
Optional	2.33	2.33	1.44

Table 4.3: Relative values for the electric field. The average saturated electric E_{sat} field is compared to three other field values. E_0 is the external electric field. E_{init} is the initial average electric field, and E_{noise} is an estimate of the field noise. A larger value means the saturated electric field "signal" is comparably stronger.

Table 4.3 show the relative values electric field values. The value of E_{init} is read of the graphs in 4.2, and the value of E_{noise} is calculated using 3.21. E_0 is the external driving electric field. It is clear that the electric field is relatively elevated to a higher value in the Optional run than in the Baseline simulation. In addition, the Optional simulation is noisier than the Baseline simulation.

Next we can look at a slice of the electric field. We can choose 3 time steps that appear to be interesting based on the figures in 4.2. We choose one time during the linear growth phase, and pick the time $3\Omega_i$, one right after the linear growth phase $6\Omega_i$, and one after the system has stabilized $12\Omega_i$.

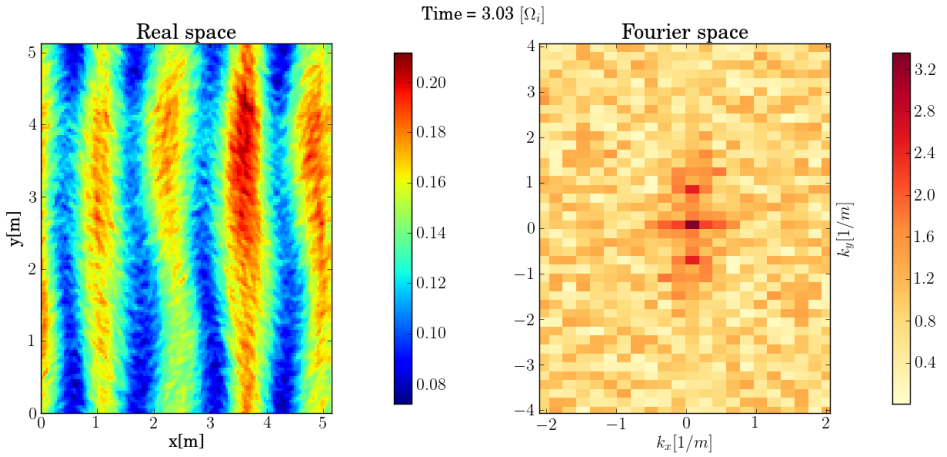

(a) Baseline simulation $T = 3\Omega_i$

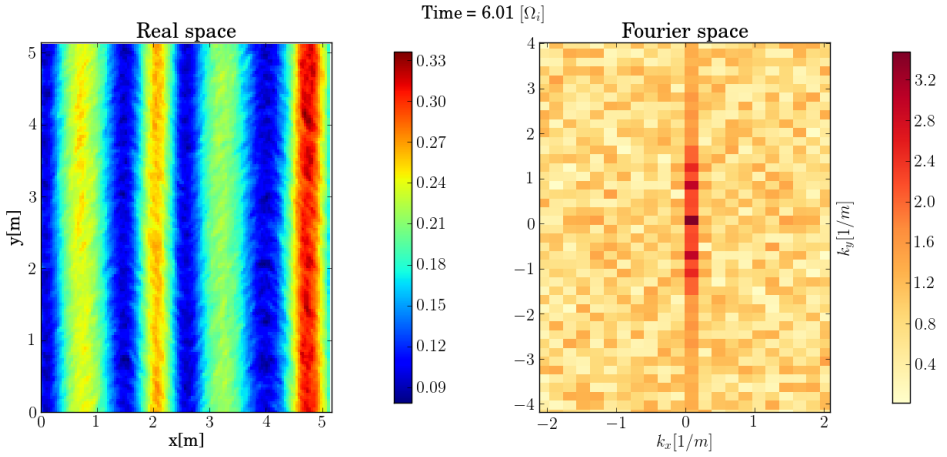

(b) Baseline simulation $T = 6\Omega_i$

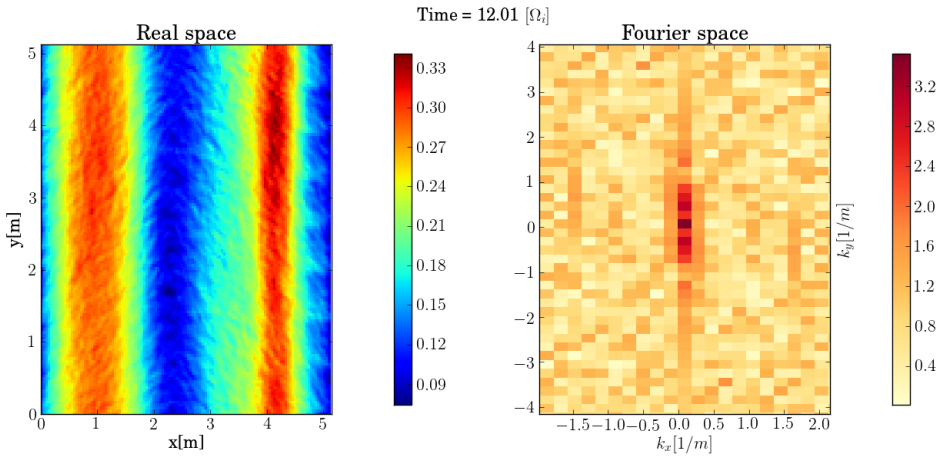

(c) Baseline simulation $T = 12\Omega_i$

Figure 4.3: plot of $|\vec{E}|$ values on a slice in x-y against its 2d Fourier transform (kx-ky) at different times.The plots show the Baseline simulation at chosen values of $T = 3, 6, 12\ [\Omega_i]$. The amplitudes in the spectral plots are logarithmically scaled.

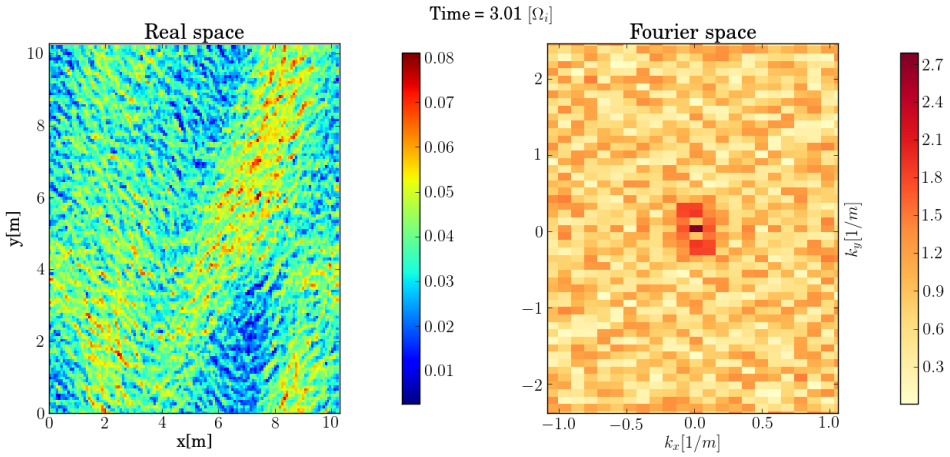

(a) Optional simulation $T = 3\Omega_i$

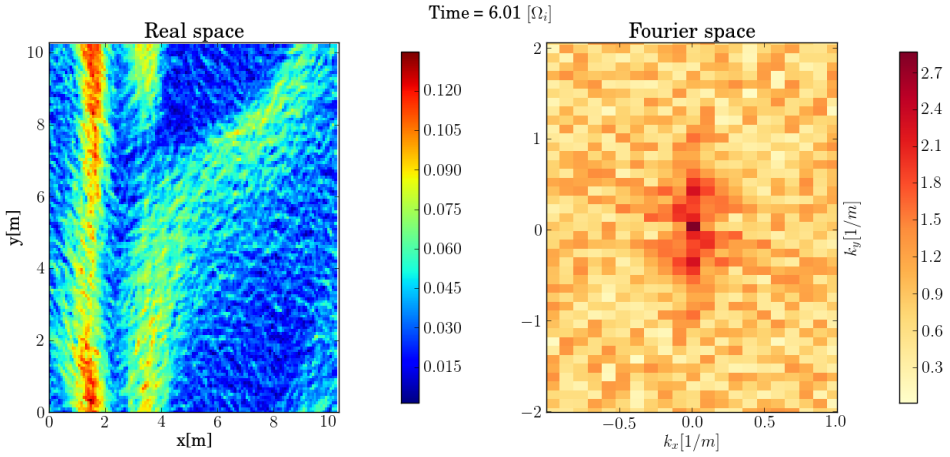

(b) Optional simulation $T = 6\Omega_i$

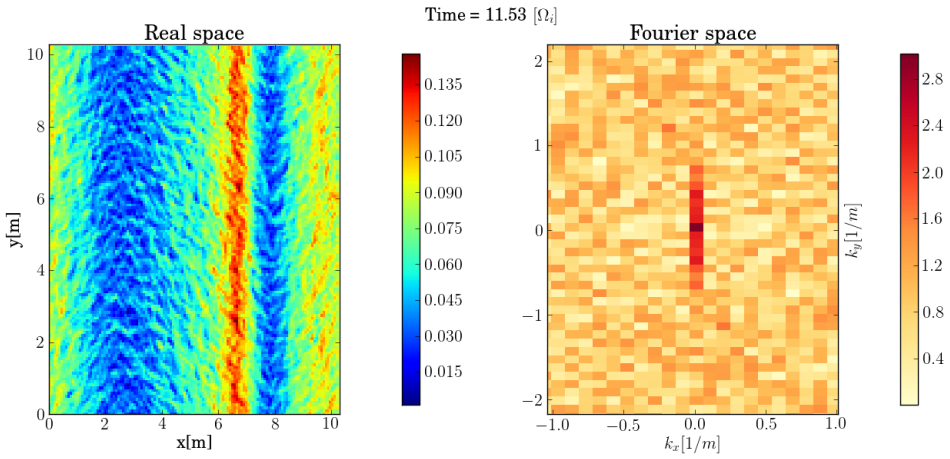

(c) Optional simulation $T = 12\Omega_i$

Figure 4.4: plot of $|\vec{E}|$ values on a slice in x-y against its 2d Fourier transform (kx-ky) at different times. The plots show the Optional simulation at chosen values of $T = 3, 6, 12$ $[\Omega_i]$, The amplitudes in the spectral plots are logarithmically scaled.

The left sides of the figures 4.3, and 4.4 are produced by computing the absolute value of the electric field at each grid point and ploting a slice in the $x - y$ domain. These are compared to the spectral domain $k_x - k_y$ on the right. The spectral plots are produced using numpys built in 2-D FFT function 3.51, and are done in amplitude space, and not the power-spectrum.

In fig. 4.3 we can see the waves build up from a broader spectrum of wave lengths to a roughly single mode that seems to be bound by the simulation box length. The same behaviour is seen in fig. 4.4, for the Optional simulation. Except here the strongest mode is the one corresponding to the box length in all sub figures.

Comparing the three spectral plots for each fig. 4.3, and 4.4 we see that there is broadening of the spectrum along the y direction. More of the shorter wavelengths seem to grow stronger from the onset until the system stabilizes. In fig 4.3 c) we can even see a periodic oscillation along y on the right side of the plot.

In the Optional simulation the growth seems to be more chaotic. From fig 4.4 b) we see that the strongest wave mode has broken up. Later in fig 4.4 c) this has stabilized to a homogeneous wave, like in the Baseline simulation. This can possibly explain the drop we saw in the electric field values from fig 4.2.

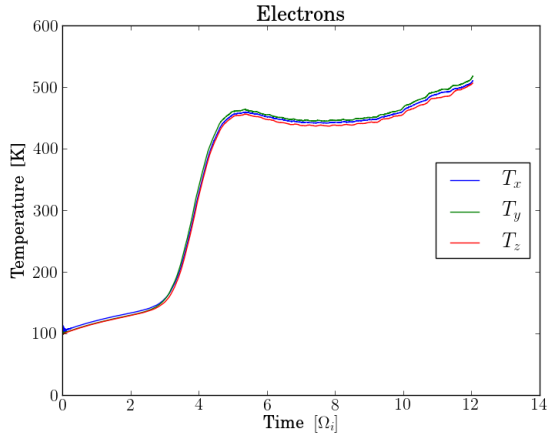

(a) Baseline

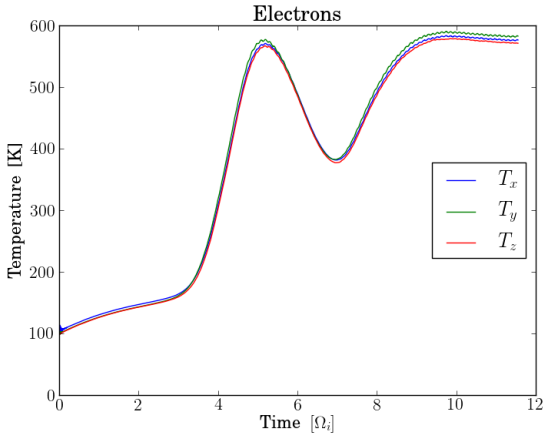

(b) Optional

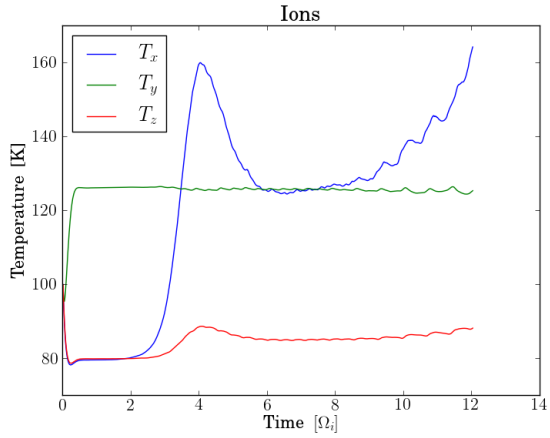

(c) Baseline

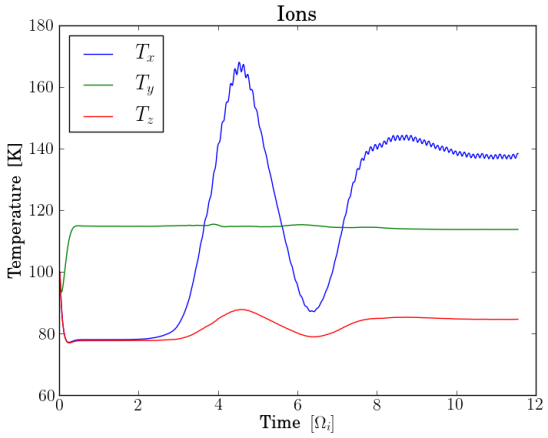

(d) Optional

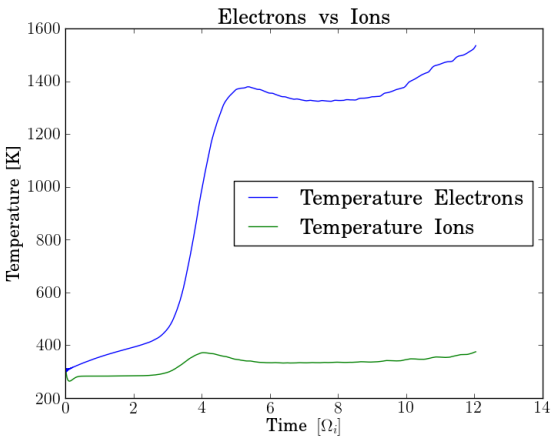

(e) Baseline

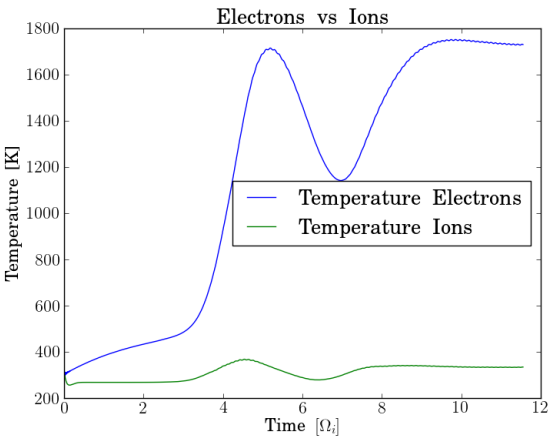

(f) Optional

Figure 4.5: Plot of the effective temperatures for both the base and Optional simulation. Plots a,b are of the electrons in x, y, z. plots c,d are of the ions in x, y, z. Plots e,f are of the total effective temperature for both electrons and ions.

The temperature plots have many similar features to the electric field plots in fig. 4.2. We can compute the temperature of each specie resulting from collisional heating balanced by collisional cooling, as done in M. M. Oppenheim and Y. S. Dimant (2004). The equation used to do this is

$$T_{i,e} = \frac{2}{3}\frac{\mu_{i,e} v_{i,e}^2}{\delta_{i,e}} + T_n, \tag{4.2}$$

where the subscript i, e stands for ions and electrons. $\mu_{i,e}$ is the reduced masses for ions and electrons. $\delta_{i,e}$ is the average fraction of energy lost during one collision ($\delta_i = 2m_i/(m_i + m_n)$). $v_{i,e}$ is the average drift speed.

For ions this can be written Yakov S. Dimant and Meers M. Oppenheim (2003)

$$T_i = T_n + \frac{m_i v_{di}^2}{3} = T_n + \frac{\kappa_i^2}{1+\kappa_i^2}\frac{m_i v_{di}^2}{3} \tag{4.3}$$

where

$$v_{di} = \left(\frac{e\vec{E}_0}{m_i \nu_i} + \kappa_i^2 v_d\right)/(1+\kappa_i^2) \tag{4.4}$$

is the ion drift with both Hall and Pedersen components, and κ_i is the ion magnetization $\kappa_i \equiv \Omega_i/\nu_i$

For all parameters involved we should have the same values for both the Baseline simulation, and the Optional simulation. The exception being a modification to the drift velocities due to collisions, but this should be small. I calculated the values to be $T_i \sim 300$K, and $T_e \sim 350$K. To do this i used the equations above for ions 4.1.1, and the equation given in the appendix of Oppenheim M. M. and Dimant Y. S. (2013) for the electrons. These values are not exactly comparable to the current simulations, However in the paper M. M. Oppenheim and Y. S. Dimant (2004) they calculate a temperature of 335K for ions, and 397K for electrons, which fits well with the wave free equilibrium values from the current simulations, and the one in the paper. The difference of our calculated values is probably due to them using a more complicated expression for the drifts.

There are some significant differences between the results of the current simulations and the comparable simulation in M. M. Oppenheim and Y. S. Dimant (2004). In this paper, the temperature of the ions rises more, which seems to exceed $\sim$ 500K. For both species the temperature also drops significantly after the linear growth phase. This is in contrast with what we see in the current simulations, especially the Baseline simulation

(which is most comparable) where temperatures don't drop for the electrons, and seem to be rising again towards the end. The electron temperatures in our simulations also rise significantly more. These differences might be explained due to the fact that we are currently running a 3-D simulation, and comparing it to a 2-D simulation from the paper. An explanation to this is given in Oppenheim M. M. and Dimant Y. S. (2013), where electron heating gets a significant contribution from a small electric field component parallel to the magnetic field. For this effect to be present, the simulation needs to be done in 3 spatial dimensions.

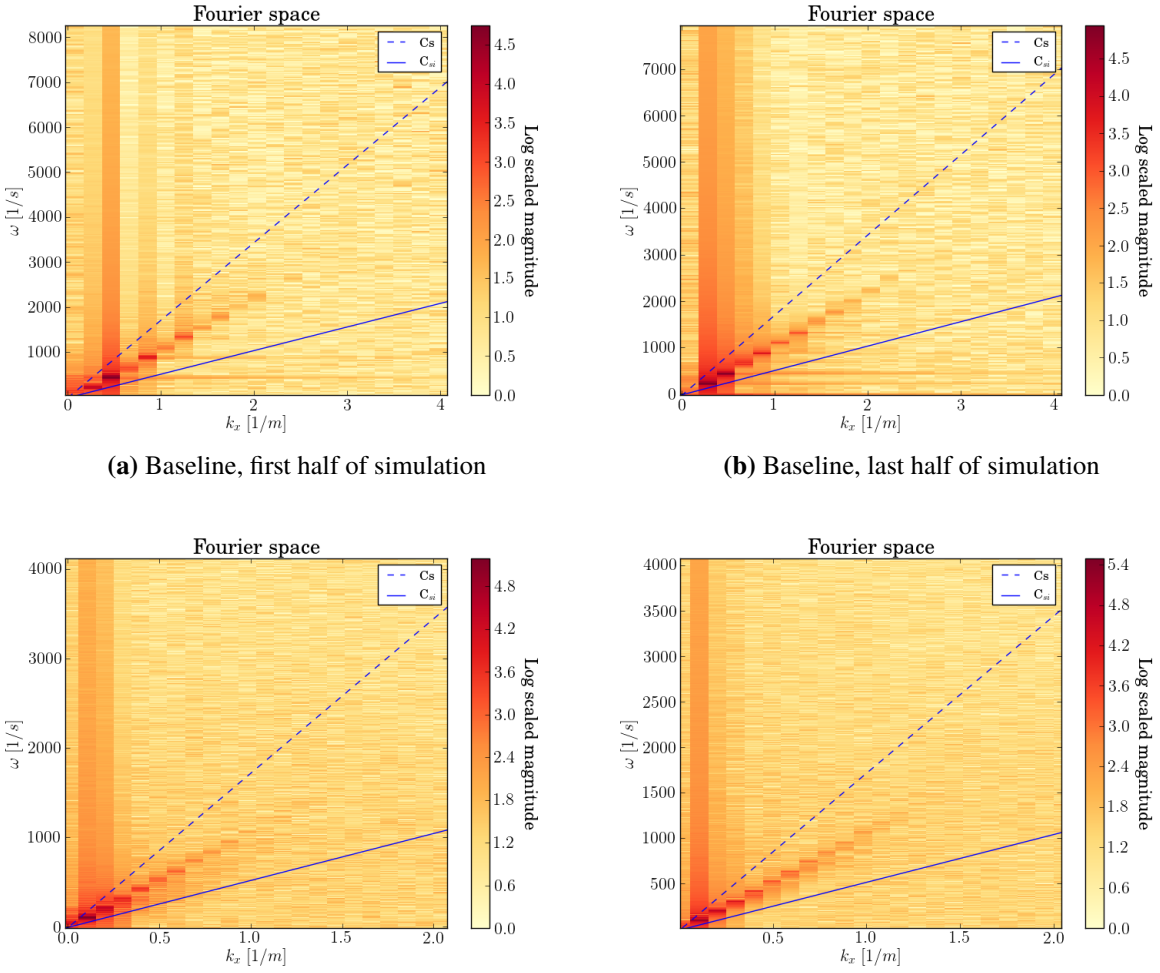

(a) Baseline, first half of simulation

(b) Baseline, last half of simulation

(c) Optional, first half of simulation

(d) Optional, last half of simulation

Figure 4.6: The figures are of the $\omega - k$ domain. The plots are scaled logarithmically and show the amplitude of a 2-D Fourier transform of keograms from a line along x in the ϕ grid.

To produce spectral plots of ω vs k we again use the built in 2-D FFT function from

numpy using eq. 3.51. In this case we feed in the keograms form fig. 4.1 to link the oscillations in time to space.

The two lines in the plot correspond to the analytic sound speed using the expression from linear theory eq. 2.43, and taking the aspect angle to be zero

$$C_s = V_d/(1+\psi). \tag{4.5}$$

and the standard expression for ion sound speed eq. 2.9

$$C_{si} = \sqrt{\frac{\gamma_i T_i + \gamma_e T_e}{m_i}} \tag{4.6}$$

where $\gamma_{i,e}$ is the adiabatic index for ions and electrons. Taking both ions and electrons to be fully adiabatic $\gamma_{i,e} = 5/3$, as a best case scenario gives a value of $C_{si} = 525.4\text{m/s}$, and from linear theory we get the predicted value of $C_s = 1728\text{m/s}$ for the Baseline simulation and for the Optional simulation. The phase velocity $v_{ph} = \omega/k$ lies between these two values in both simulations. This is also in agreement with earlier work, with similar simulations M. M. Oppenheim, Y. Dimant, and Dyrud (2008). We also know from linear theory (eq. 2.30) that the waves can not have a phase velocity above the value of C_s, and from radar backscatter we know that the phase velocity should be comparable, or slightly greater than the ion sound speed C_{si}.

Again we see that the Optional simulation tends towards longer wavelengths, the strongest mode is also almost an order of magnitude stronger in the second half of the simulation, for the Optional simulation. In the Baseline simulation this is not the case where the strongest mode is the same for the first and last half of the simulation.

4.1.2 Lowered Driving Electric Field

The next set of simulations use the exact same parameters as in table 4.1, except for the external driving electric field E_0. We run with a value of E_0 that is half that of the two previous simulations. We run one new simulation using Baseline parameters except we run it with $E_0 = 0.05\text{V/m}$. We can for simplicity call this one “Baseline Lowered”, and we run one with the Optional parameters and $E_0 = 0.015\text{V/m}$. This one we call “Optional Lowered”. In both simulations the driving electric field is still roughly double the threshold electric field.

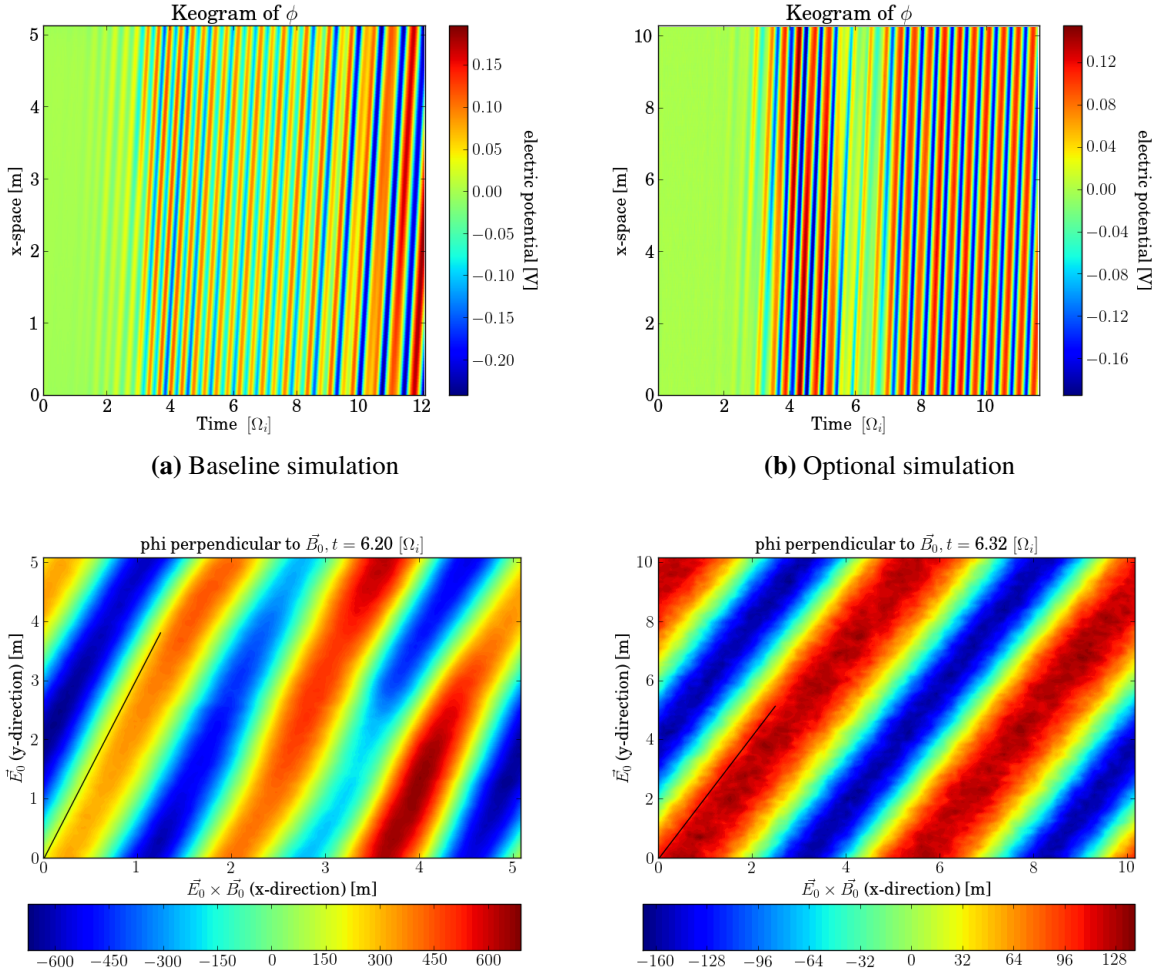

(a) Baseline simulation

(b) Optional simulation

(c) Baseline simulation

(d) Optional simulation

Figure 4.7: Keograms of a slice in x-direction for each time step. The slice is of the ϕ (electric potential) grid.

The keograms in fig. 4.7 show the development of the two new simulations in time. In this case both simulations start building a wavelength, which seems to persist throughout the simulation. This is in contrast to the Baseline simulation in fig 4.1. Lowering the driving field has also led to both of the new simulations having waves that are tilted downward. The angle θ of this tilt is found by plotting a line corresponding to the tilt angle $\theta - \pi$, so we easily can see the line matching the transverse direction of the wave. We found the angles to be $-\pi/10$ for the Baseline Lowered simulation, and $-\pi/7$ for the Optional Lowered simulation.

As in the two previous simulations we can calculate the optimum wavelength for these two simulations.

	Baseline	Optional
Mean-free path	0.32 m	1.07 m
eq. 2.51	1.94 m	5.04 m

Table 4.4: Calculated values of the wavelength for the Baseline Lowered and Optional Lowered simulation.

We have not changed any of the collision frequencies, or the thermal velocities, so the mean-free paths are the same. The values in table 4.4 for eq. 2.51 where computed using the angles found in the potential plots of fig 4.7. The mean-free path values are again too low, but closer, as the dominant wavelength is shorter in this case. The values calculated using eq. 2.51, and taking into account the wave tilt, are again in excellent agreement.

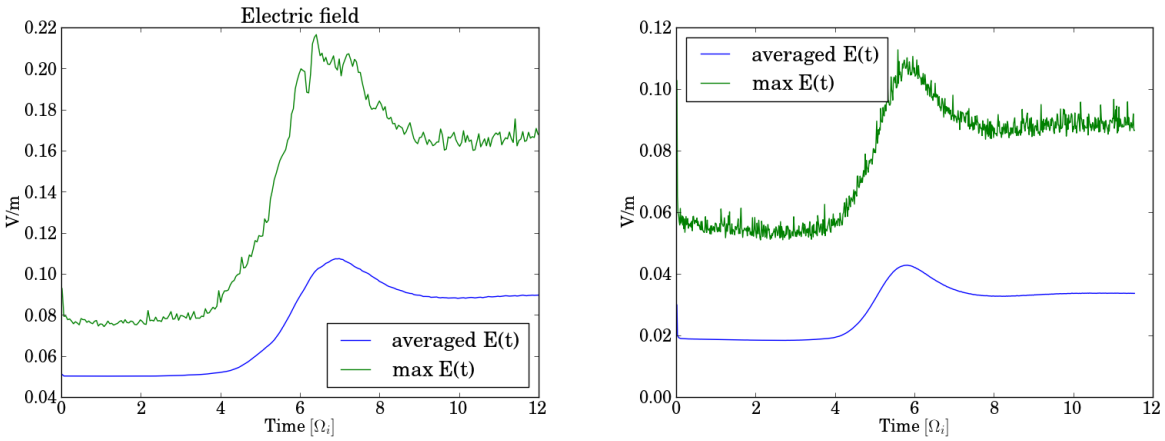

(a) Baseline **(b)** Optional

Figure 4.8: Electric field average and max values plotted in time. Time is scaled with Ω_i since physics seem to scale with this value.

The overall shape of the electric field values in fig. 4.8 is similar to the previous set of simulations fig 4.2. One apparent difference is that there are no periodic spikes, like in fig. 4.2 a), but instead both simulations in the lowered driving electric field case are smoother. The Baseline Lowered simulation has an initial average value of $\sim 0.05\text{V/m}$, and rises to about $\sim 0.10\text{V/m}$, before dropping to $\sim 0.09\text{V/m}$. In the plot for the Optional Lowered simulation, the average electric field is initially $\sim 0.02\text{V/m}$, before peaking at $\sim 0.04\text{V/m}$, and stabilizing at $\sim 0.034\text{V/m}$. These values are close to half of those we got in the previous two simulations, which suggests linear scaling of the polarization electric field due with the driving electric field.

	E_{sat}/E_0	E_{sat}/E_{init}	E_{sat}/E_{noise}
Baseline	1.8	1.8	1.84
Optional	2.67	1.7	0.697

Table 4.5: Relative values for the electric field. The average saturated electric E_{sat} field is compared to three other field values. E_0 is the external electric field. E_{init} is the initial average electric field, and E_{noise} is an estimate of the field noise. A larger value means the electric field "signal" is comparably stronger.

In table 4.5 we compare the average saturated electric field values to some relative electric field values. The Baseline Lowered simulation has similar values as the regular Baseline simulation, but suffers from a lower signal-to-noise (SNR) value. (the last one in table 4.5). The same thing is apparent in the Optional Lowered case, but here the calculated noise is comparable to the average electric field. We have chosen to call the saturated electric field values a "signal" since it includes more than only the polarization electric field.

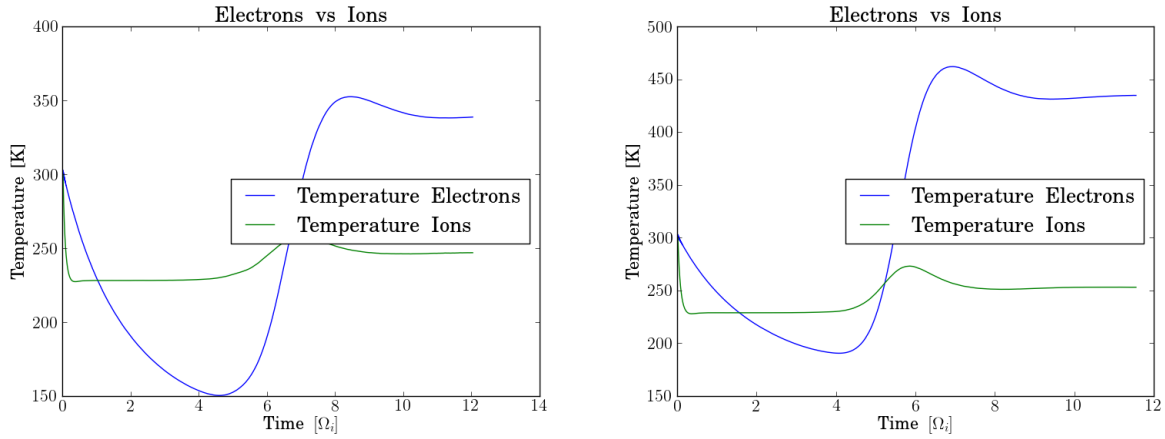

(a) Baseline **(b)** Optional

Figure 4.9: Plot of the effective temperatures for both the base and Optional simulation. Plots a,b are of the electrons in x,y,z. plots c,d are of the ions in x,y,z. Plots e,f are of the total effective temperature for both electrons and ions.

Effective temperatures are given for both the Baseline Lowered case, and the Optional Lowered case in fig. 4.9. In both cases temperatures drop significantly for the electrons, before rising during the linear growth phase. The lowest values are $\sim$ 150K for the Baseline Lowered simulation, and $\sim$ 180K for the Optional simulation. After the linear growing phase they stabilize at $\sim$ 350K for the Baseline Lowered simulation, and $\sim$ 450K for the Optional Lowered simulation. The electron temperature values are

far from half of those we got in the first two Baseline and Optional simulations. This suggests that electron temperatures do not scale linearly with the driving electric field.

	λ_d/dx	$r_{g,e}/dx$
Baseline	0.67	0.89
Optional	0.37	1.64

Table 4.6: Table showing temperature dependent stability parameters.

Temperatures dropping this far in a simulation is of major concern, as we can see in table 4.6. We have given relative values for the condition $\lambda_d/dx < \pi$, and where in general $r_{g,e}/dx > 1$ at least. (see section 3.3). The actual numbers are computed using $v_{th,e}$, so in reality there are some particles with even poorer resolution with respect to $r_{g,e}$. In any case the condition on gyroradius is broken for the Baseline Lowered simulation, and possibly for the Optional Lowered simulation.

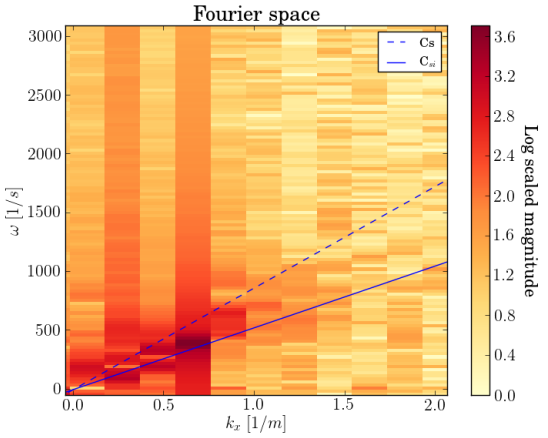

(a) Baseline lowered, first half of simulation

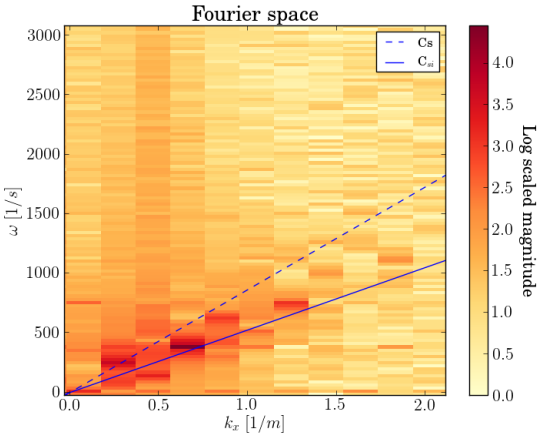

(b) Baseline lowered, last half of simulation

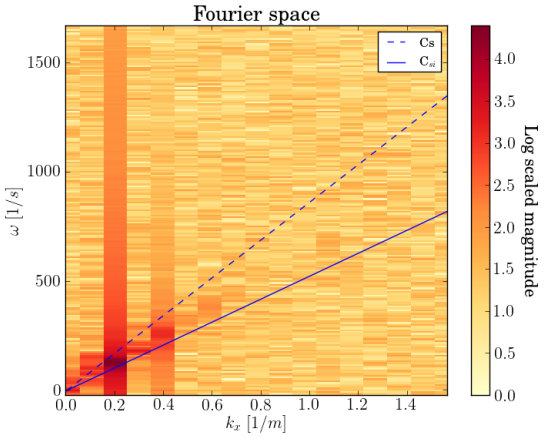

(c) Optional lowered, first half of simulation

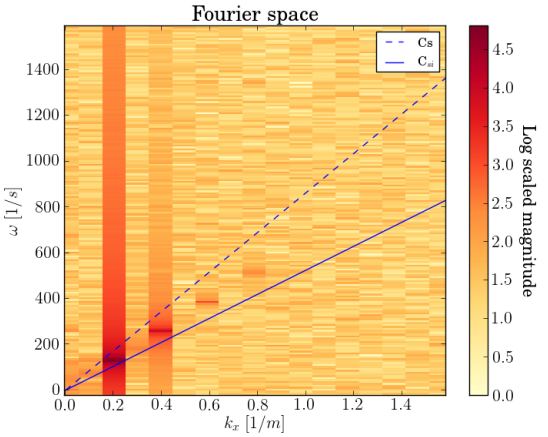

(d) Optional lowered, last half of simulation

Figure 4.10: The figures are of the $\omega - k$ domain.. The plots are scaled logarithmically and show the amplitude of a 2-D Fourier transform of keograms from a line along x in the ϕ grid.

Fourier transforming the keograms in fig 4.7, yields similar results overall as the previous Fourier transforms in fig. 4.6. We can again see the phase velocity mainly lining up in between C_s (eq. 2.43), and a fully adiabatic ion acoustic peed C_{si}, from eq. 2.9. However, the clear sharp line for the phase velocity seen in fig 4.6, seems to be "smudged" out somewhat in this case. There are also some significant amplitudes that fall outside of the two sound speed lines, this seems to be especially the case for the Baseline Lowered simulation. This is probably explained by the relatively higher noise in these simulations.

4.2 Baseline Simulation - Stability Test

Due to rising concerns about the stability of the system I deemed it necessary to do a stability analysis. To this aim we can run four test simulations using the Baseline parameters (table 4.1). We can for these tests lower the grid size as we are not interested in physical waves, but rather the numerical stability. A reasonable size of $n_x = n_y = n_z = 32$ was used, and we modified the following parameters.

	$\vec{E}_0$	$\vec{B}_0$	Collisions
Test 1	$0.1\mathrm{V/m}$	$5 \times 10^{-5}\mathrm{T}$	–
Test 2	$0.001\mathrm{V/m}$	$5times10^{-5}\mathrm{T}$	–
Test 3	–	$5 \times 10^{-5}\mathrm{T}$	–
Test 4	–	–	–

Table 4.7: Table showing The difference in the four stability test simulations.

As we can see in table 4.7, the test are set up as follows. Test 1 has the Baseline parameters, but no collisions. In test 2 we use a lower driving field E_0, in addition to no collisions. In test 3 we turn off the driving field E_0, and have no collisions. In test 4 we turn off both external fields E_0, B_0, and turn off collisions.

	λ_D/dx	$r_{g,e}/dx$	$(dt \times \omega_{pe})/2$	$(dt \times \Omega_e)/2$
Baseline	0.94	1.27	0.40	0.30
Optional	2.12	0.47	0.40	0.09

Table 4.8: Stability parameters. The Baseline simulation has poor resolution in space relative to the gyroradius of the electrons. While the Optional simulation has poor resolution in space relative to the Debye length of the electrons. Both are "expected" to be stable.

We can analyze the expected stability of the system by computing some basic stability parameters 3.3. In table 4.8 we list these parameters, and we can note that the time constrains seem to be barely satisfied. Usually we wish $(dt \times \omega_{pe})/2 \ll 1$. However the resolution in space is close to one of the constraints in both the Baseline and Optional simulation. For the Baseline simulation, using $v_{th,e}$ as a mean value, $r_{g,e}$ is close to dx. For the Optional simulation λ_D/dx is close to π, but both are within the absolute limit. It is also worth noting that dx/dt is close to $v_{th,e}$.

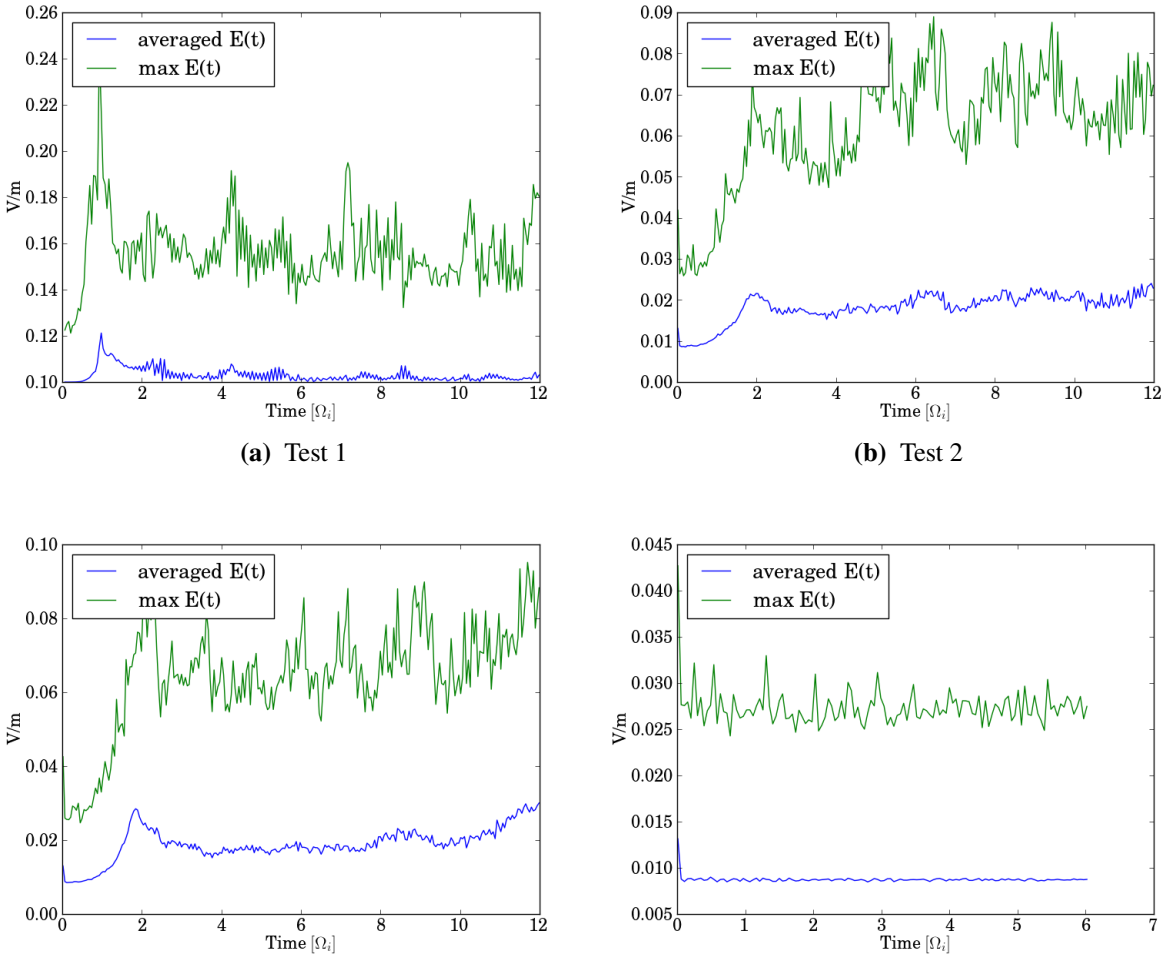

(a) Test 1

(b) Test 2

(c) Test 3

(d) Test 4

Figure 4.11: Electric field values in time for the four tests. Average, and max values are given in V/m.

It is permissible that the electric field values go up. This would mean that energy is stored in the fields. In this case this energy would have to come from somewhere. If we have an external electric field, this can be the source of free energy. However, if there is no external electric field, as in test 3, and 4, the energy must come from kinetic energy. If there is stability, and no exotic physics we should expect the average electric field to be constant (or oscillate near $\omega_{p,e}$). From the above reasoning we can see that test 4 is most likely stable, but the other three might have problems if there is not a drop in average energy.

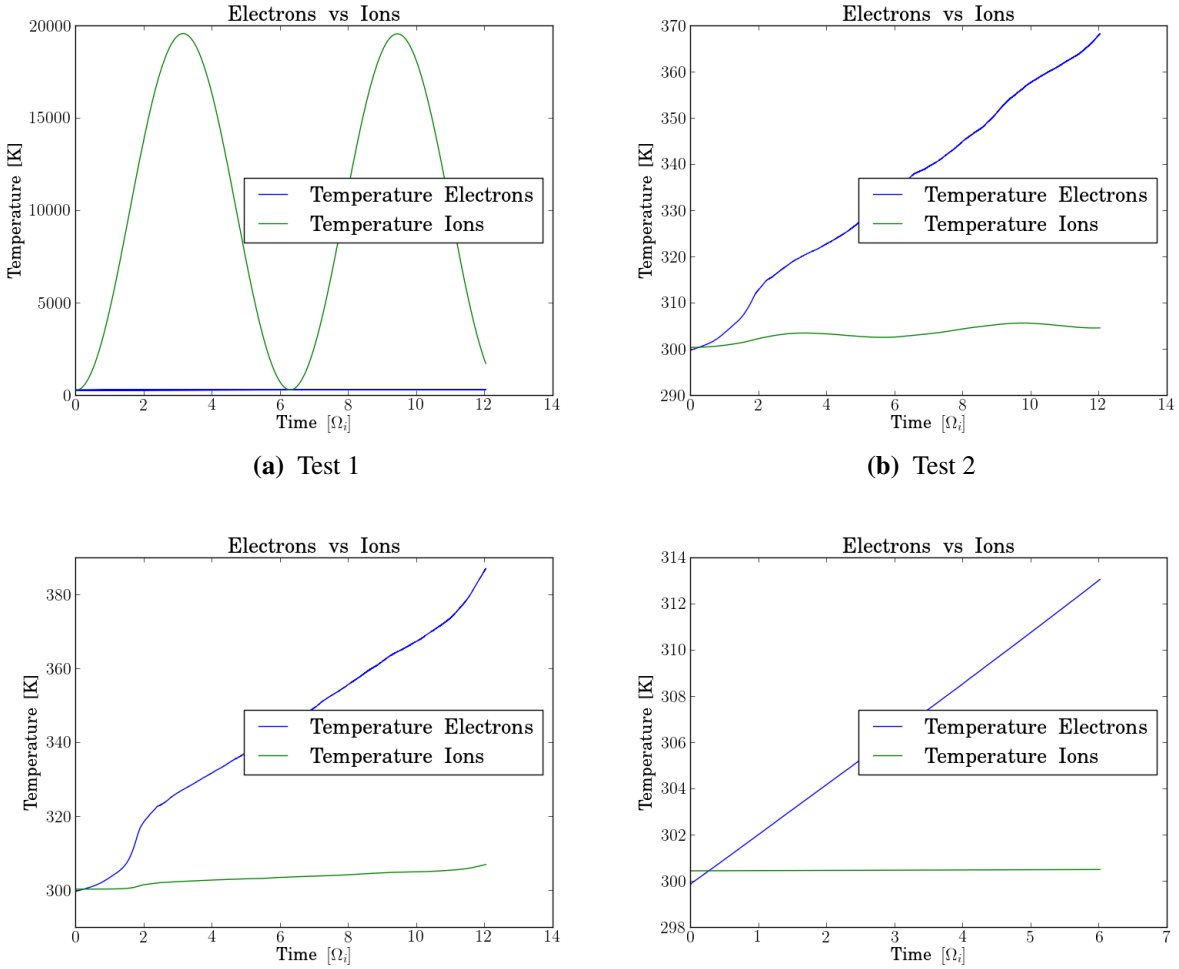

(a) Test 1

(b) Test 2

(c) Test 3

(d) Test 4

Figure 4.12: Average energy is given in nits of Kelvin for both species, and plotted in time for the four tests.

In fig 4.12 we can see that the energy is, contrary to the above reasoning, rising. We need to interpret the energy plots with a grain of salt though, as our PiC code is not energy conserving, and it can be shown that on long timescales the plasma will heat numerically in such a code. This long timescale heating is expected to be slow and linear, like in 4.12 d). However, in fig. 4.12 c) d) we can see an abrupt rise that coincides exactly with the rise in the electric fields in fig. 4.11 c) d). This points to a stability issue. The rise is not that high so it would seem that it is a borderline case.

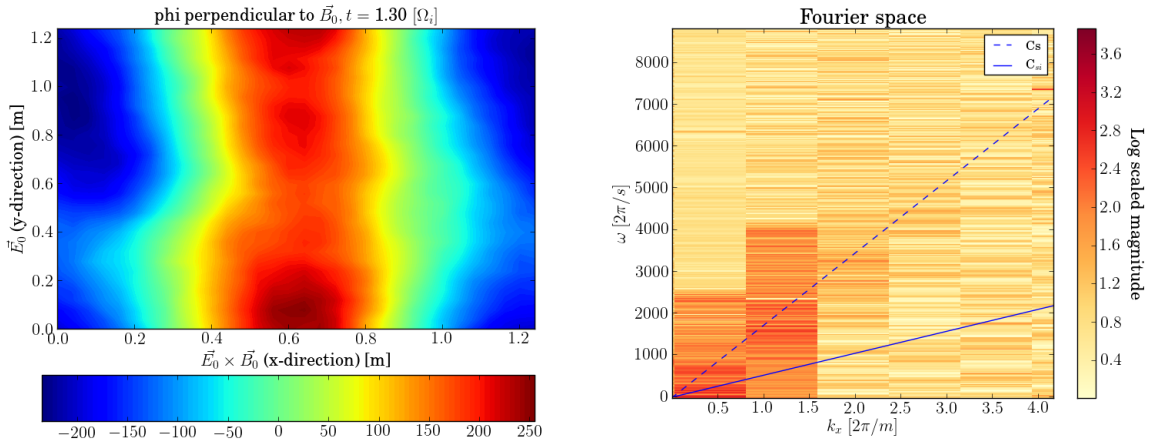

(a) Potential **(b)** FFT of keogram

Figure 4.13: Potential and Fourier transform of a keogram of ϕ to show the similarities to the FB-instability. The potential figure was chosen at a time in the middle of the abrupt rise in electric field and temperature values.

In fig 4.13 we show a slice of the potential and a Fourier transform of $\omega - k$ space for the first test, where the drift v_d is the same as the Baseline simulation. It is important to note here that the Farley-Buneman instability is entirely excluded from this test, as the electrons and ions are drifting with the same speed. This is because the ions are not collisionally slowed. However, the test shows some remarkable similarities to the FB simulations above. However the "wave" in figure 4.13 a) was periodically observed, and mostly in the vicinity of the abrupt jump in electric field. Thus, it seems that these numerical effects can not account for the waves seen in the Baseline, and Optional simulations.

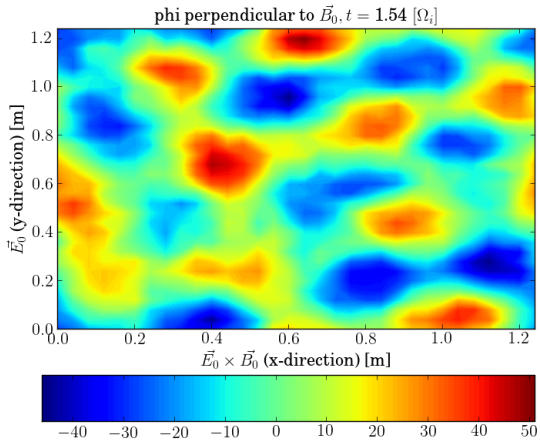

Figure 4.14: Potential figure for test 3. The time was chosen in the middle of the abrupt rise in electric field, and temperature values.

The last figure shown, fig 4.12 is included to show the "griding" effect. This seems to happen in both test 2, and test 3. It is also only present during the abrupt rise in electric field, and temperature from about $1.2\Omega_i$ to $2.11\Omega_i$. This effect has been observed in earlier studies of numerical instabilities due to poor resolution of the gyroradius Horký and Miloch (2015b).

Chapter 5

Discussion

In this chapter we will start with a discussion of the results presented in chapter 4 in context of the theories given in chapter 2.3. We will after this discuss the results in context of the new collision model, and the implications such a model has on simulations. Lastly we will discuss the results in context of the stability issues that arise from the subsection 4.2.

5.1 Comparing Result With Theory

The largely outstanding question of the FB-instability is the question of "what mechanism suppresses growth, and leads to saturation?". The results shown in 4.1 are subject to a limited simulation domain. Therefore the saturation levels are likely due to some coupling mechanism of the waves with itself on the periodic boundaries. With this said, we still see some remarkable equalities with theory.

Most notable is the agreement between wavelengths observed and calculations of the optimum wavelength from eq 2.51. These calculations use an equation given in Yakov S. Dimant and Meers M. Oppenheim (2003), where they argue that ion thermal effects play a significant role in lower E-region instabilities. The ion thermal effect arises from a mechanism where the ion thermal perturbations are out of phase with the density perturbations. This will lead to a modification of the pressure term in a similar way to the ion inertia "pressure" which drives usual FB-instability. In Yakov S. Dimant and Meers M. Oppenheim (2003) they show that the ion thermal effect can lead to a tilting of the wave. As we also observe a tilting (in the lowered driving electric field case), and calculate almost exact optimum wavelengths with, and without this tilt, this naturally leads us to believe that ion thermal effects have a significant role in the present simulations. There are other mechanisms proposed to explain the tilting of the wave. In St.-Maurice and Hamza (2001) they develop a non-spectral "blob" approach. The

"blob" approach is shown to lead to growth and saturation that match observations. However, the equation given in this method 2.3.5 should lead to the same angle of flow for both the Baseline Lowered and the Optional Lowered. This does not match our findings.

In addition to the wavelengths agreeing with the theory from Yakov S. Dimant and Meers M. Oppenheim (2003), the phase velocities are in good agreement with theory. We know from the original work of Buneman (1963) eq. 2.30, that waves can not have a phase velocity greater than the value we called C_s in the spectral plots of ω vs k. fig. 4.6, and 4.10. The same constraint, in conjunction with eq. 2.43 also says that the phase velocity must be greater than the ion sound speed. In the results chapter we computed the ion sound speed using fully adiabatic ions and electrons to get an estimate of the "highest" possible sound speed, which we called C_{si}. The results showed that in all four FB simulations the phase velocities lined up in between these two values, giving us a good argument for this being the FB-instability. In earlier work M. M. Oppenheim, Y. Dimant, and Dyrud (2008), they get the same result with the phase velocities lining up in between these two calculated values (albeit using a slightly different method). This result of M. M. Oppenheim, Y. Dimant, and Dyrud (2008) would be most comparable to the Baseline Lowered simulation as they use the same driving electric field, external magnetic field, and almost the same collision frequencies. They also plot a line along the center of the phase velocities, at a velocity they calculate using adiabatic 1-D ions, and 3-D adiabatic electrons. This line exactly matches the phase velocities in their simulation, making the argument for 1-D adiabatic ions. In the current results we have decided to leave out this 1-D adiabatic ion line, because the theory does not say that the phase velocities should match the ion acoustic speed, but rather that it needs to be greater than the ion acoustic speed. However, the two other lines for C_s, and C_{si}, and the phase velocities lining up in between are in good agreement with their result.

In the plots of the keograms of fig. 4.1, and 4.7, we saw that the Baseline simulation started with a shorter dominant wavelength, and transformed to a longer dominant wavelength. This suggests that spectral energy is transferred from shorter wavelength modes to longer wavelength modes. This observation is in agreement with earlier simulations M. M. Oppenheim, Y. Dimant, and Dyrud (2008) and Oppenheim M. M. and Dimant Y. S. (2013). However it seems that this process does not always happen, as we did not observe this in the other simulations. In the optional simulation we calculated the optimum wavelength to be almost the same as the box length. Thus, we can expect that a similar process of spectral energy transfer could happen on a larger simulated domain, but to wavelengths longer than the current box length. However, for the two lowered simulations, this process should be possible in the current simulations, but it does not seem to be present in these two. This could be due to the lower driving electric field, as this leads to less free energy in the system. However, if the main mechanism for suppression of growth is the transfer of energy from shorter to longer wavelengths, we should expect this process to be present in the lowered simulations

also, which suggests that this can not be the reason alone for suppression of growth.

In the current simulations we have observed a broadening of the spectrum in the electric fields in the transverse direction k_y, fig 4.3, and 4.4. This broadening means that there is an increase in spectral energy along the k_y direction, which strongly suggests some sort of mode coupling between the primary $\vec{E} \times \vec{B}$ direction and perpendicular modes in the $\vec{E}$ direction. This result is something that is not discussed in depth in earlier work M. M. Oppenheim and Y. S. Dimant (2004), M. M. Oppenheim, Y. Dimant, and Dyrud (2008), and Oppenheim M. M. and Dimant Y. S. (2013), and is therefore an interesting topic for future work. This result gives weight to the non-linear mode coupling theories Hamza and Imamura (2001), where energy is transferred from the direction of flow to perpendicular directions trough coupled wave modes (although usually to the $B_\parallel$ direction).

An observation made by comparing the temperatures of the four FB simulations is that temperature does not seem to scale linearly with the driving electric field E_0. We can compare this result to the calculations done in Oppenheim M. M. and Dimant Y. S. (2013), where it is argued that the electron temperature $T_e \propto E_\parallel$. In addition taking into account that the electric field values do seem to scale linearly, which is backed up by the results in M. M. Oppenheim, Y. Dimant, and Dyrud (2008), this leads to a discrepancy. Either the average perturbed electric field scales linearly, but the $E_\parallel$ values do not, or the argument for $T_e \propto E_\parallel$ is flawed. There is a third option which is numerical heating, but it is reasonable to assume numerical heating to be more severe in the lowered case. However, this does not seem to be the cause because temperatures are less than half in the lowered case, where the driving electric field is only half. A more extensive parameter study on the linearity of $E_\parallel$ would be highly relevant.

5.2 Result With New MCC Module

The new collision module has proven to work satisfactory based on the fact that we where able to simulate the FB-instability. That we are indeed simulating the FB-instability seems apparent by the similarities between our current simulations and earlier work M. M. Oppenheim and Y. S. Dimant (2004) and Oppenheim M. M. and Dimant Y. S. (2013), and the agreement with theory discussed above. There are however some discrepancies worth noting. First, the wave free temperature values we observe are slightly higher for the electrons, and slightly lower for the ions than those in M. M. Oppenheim and Y. S. Dimant (2004). This might be due to their use of a $\nu \propto v^2$ collision model which is sometimes used. This will lead to a lower temperature as, on average, more energetic electrons will collide. On the other hand, ions have a slightly lower temperature in our simulations, which can not be explained by the same reasoning, but it does suggest that slightly different models are used.

5.3 Results With Numerical Issues

In all of our FB-instability simulations we have higher saturated temperature values compared with M. M. Oppenheim and Y. S. Dimant (2004). This is most likely because we are currently running a 3-D simulation, and comparing to a 2-D simulation. The temperature values are more in line of the 3-D simulations presented in Oppenheim M. M. and Dimant Y. S. (2013), where they attribute the high electron temperatures to the "anomalous Electron Heating" (AEH). It is explained theoretically (in the appendix of Oppenheim M. M. and Dimant Y. S. (2013)), where a small parallel electric field component can lead to significant heating of the electrons.

The AEH Oppenheim M. M. and Dimant Y. S. (2013) is explained with a component of the electric field being parallel to the magnetic field. Although this might be correct, it is my belief that this cannot be the only (or main?) reason for heating in these simulations. As we clearly see in 4.2 there is heating in the $x - y$ plane that is present even when there is no source of free energy (i.e only magnetic field). since there is no significant heating in the same system without the magnetic field, this heating must be due to the poor resolution of the gyroradius $r_{g,e}$.

As collisions with neutrals can control the energy in the system, it would seem that using a null-collision model to control collisions gives the user a method to dampen, and smooth out numerical effects. As such, one needs to be extremely careful of this smoothing effect. Although the simulations clearly show real physics (see above), it is hard to differentiate where the real physics ends, and numerical effects start. In addition numerical instabilities have a tendency to look very similar to the real instabilities 4.2, which further complicates the matter.

We can also deduce from the above that the usual stability constraint

$$dx < Cr_{g,e} \tag{5.1}$$

where $r_{g,e}$ is the smallest gyroradius present and C is a constants that is often taken to be one, but seems to need to lie in the range of > 3. This is an empirical result that is unproven, but other other papers have shown similar results before Horký and Miloch (2015b).

We have also seen that numerical noise was mixed into the simulations from table 4.3, and 4.5. In the case of the Optional Lowered simulation this seems to have manifested itself in the Fourier transforms with significant components at unexpected wave frequencies. It does however appear that this has not suppressed growth of the FB-instability as we would expect.

Chapter 6

Future work

6.1 Improving the Collision model

The cross section model used in the results of this thesis is the $\nu \propto v$ model which uses a constant cross-section. It is discussed in the literature Oppenheim M. M. and Dimant Y. S. (2013) whet er a $\nu \propto v^2$ or a $\nu = C$ constant collision frequency is more physical, based on heuristic arguments. However, the best cross-section model would be one that is based real cross sectional data. The framework for such a model already exists in the collisional module of PINC in the "functional cross-section" model explained in sect 3.4.6. Implementing more realistic cross-sections should therefore be easy if we had a correct functional form for the cross-sections. This functional form could be decided in one of two ways. We could use the existing function and decide the parameters involved based on real cross-section data. This method would probably be made to work in an energy range, and is thus not the most physical. Or if we had cross-section data from a wide range of energy values, we could use a three or fourth order polynomial fit, and use this polynomial as our cross-section function.

The collision module in its current form does not ensure complete randomization of the particles picked to collide. This is because we use bins with a fixed size, such that three adjacent particles cannot all collide, which should be possible in truly random system. One simple solution would be to use variable bins, and change the stepping through the population accordingly, but better schemes for randomly picking particles should therefore be investigated.

In the lower E-region ionosphere inelastic collisions dominate. This is per now only mimicked through modification of the neutral mass in an electron-neutral elastic collision event. A model to truly simulate inelastic collisions should be investigated.

6.2 Improving The Field Solver

A considerable effort was made to run a larger simulation as a part of this thesis. We where given 345000 CPU Hrs on the Abel HPC at UiO, and where planning on running on $\sim$ 2000 CPU's. This would have been the equivalence of running $\sim$ 39 yrs on a single CPU. This was unfortunately never done because of issues with scaling up PINC to this size. Initially it was believed that the problem lied with MPI, and a bug report was filed, but after extensive debugging it is seemingly clear that there is indeed a problem in PINC. The debugging effort on this problem is exhaustive as we need to run on upwards of 512 CPU's just to reproduce the issue. We also thought the issue was solved at one point when it was discovered that the buffers used to send and receive scaled with the real domain, and not the local domain.

As of today the issue seems to lie in the usage of "MPI_ANY_TAG", and "MPI_ANY_SOURCE" in the exchangeMigrants() function. This is done so that the processor can receive and process whichever message comes first. This seems to work on smaller domains, so it is strange that it does not work when scaled up. The usage of "MPI_ANY_SOURCE" and "MPI_ANY_TAG" is in general unadvised, so a modification might be needed.

Another possibility is that there is something in the solver that leads to a race condition. The multigrid solver sends messages between neighbors at each level of the multigrid cycle, this means a lot of possible race conditions. If at some point two processors are at a different level this would also lead to a crash.

It has also been observed that the multigrid solver scales poorly above $\sim$ 64 CPU's. Theoretically this should not happen to such a degree as observed (roughly 10 times slower from 64 to 128 in one instance). So improvements to the solver seems necessary. One possible solution is to offload the solver to a GPU (or a single CPU). The usage of subdomains leads to a theoretical complexity of $\mathcal{O}(N_g log(N_g))$, but in reality it might be worse. Consider the case of four subdomains in a line. For long wave solutions the solution must propagate through all four subdomains. The multigrid solver will solve its own subdomain effectively, but then exchanges "a part" of the solution to the neighbor. This needs to be repeated until the solution propagates throughout all four domains. If we instead solve the whole grid on one large domain, this will effectively be done with a theoretical complexity as $\mathcal{O}(N_g)$.

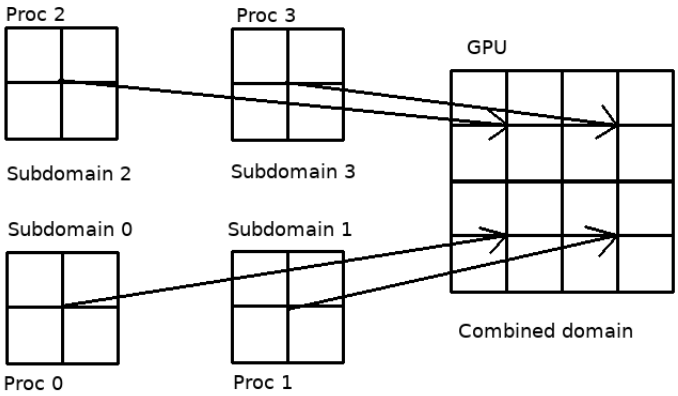

Figure 6.1: CPU's can offload their field grids to a GPU. Then the GPU can solve the fields and send back the solution.

Offloading the grids to the GPU will also remove much overhead since there is no need to communicate between processors at each multigrid level. A GPU is also well optimized for the type of equations we solve 3.12 and 3.13, see for example FXAA anti-aliasing algorithm used for computer games. The drawback of this would be the limit on a grid. When domain decomposing there is no limit, we can always add more subdomains, but on a GPU we will be limited by the GPU RAM. We can compute this limit on a reasonable sized GPU with 8 GB of RAM. Using double floats of 8 bytes for each grid point, and three dimensions the number of grid points in one dimension is $n_x = (8GB/8B)^{1/3} = 1000$. So we are limited by a $\sim 1000 \times 1000 \times 1000$ grid.

Lastly, as we have seen in the results, numerical noise has proven to be a problem. This problem could be alleviated through Fourier filtering schemes, such as the one in Verboncoeur (2005).

Appendices

Appendix A

Additional Collision Tests

in this appendice we present some additional plots from the MCC collision testing. These figures are meant only as a supplement to the section on verification of the new MCC module.

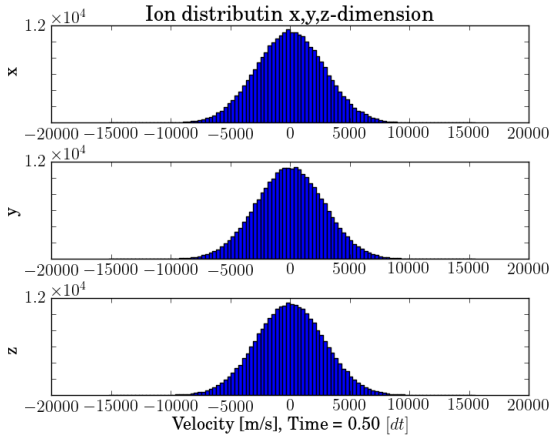

(a) Initial Ion-Elastic

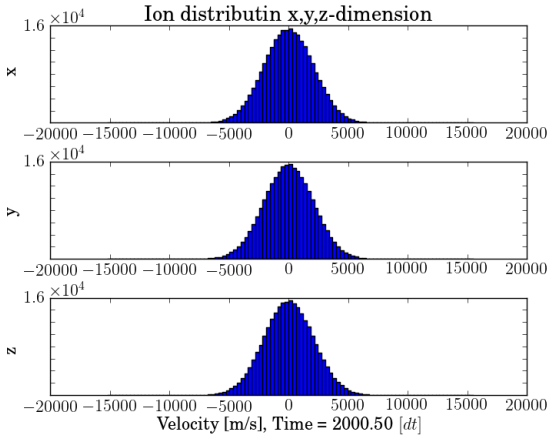

(b) Final Ion-Elastic

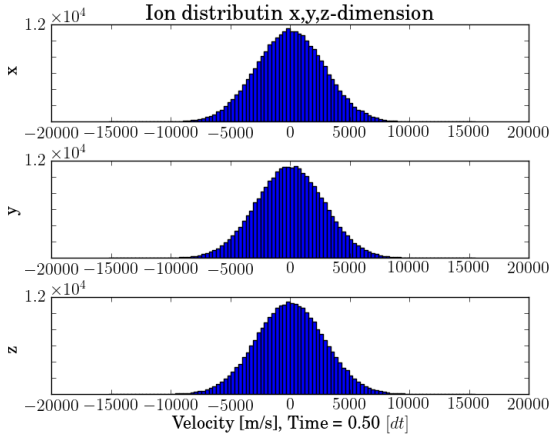

(c) Initial Charge-Exchange

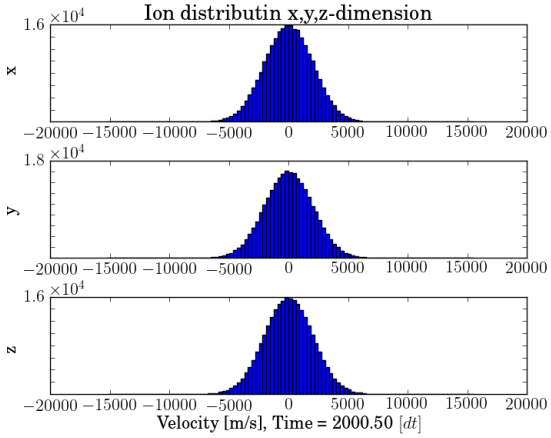

(d) Final Charge-Exchange

Figure A.1: Collection of initial and final v_x, v_y, v_z distributions for the lower neutral temperature case $T_n = 500$.

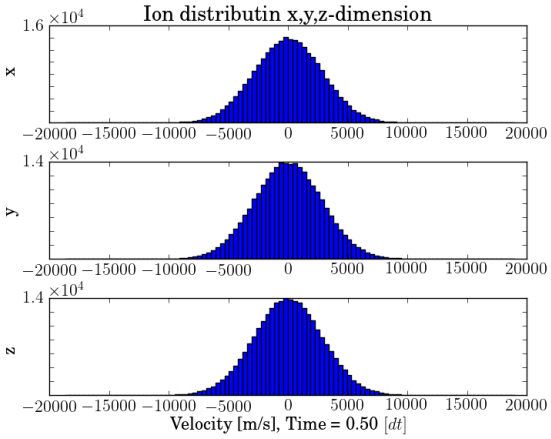

(a) Initial Ion-Elastic

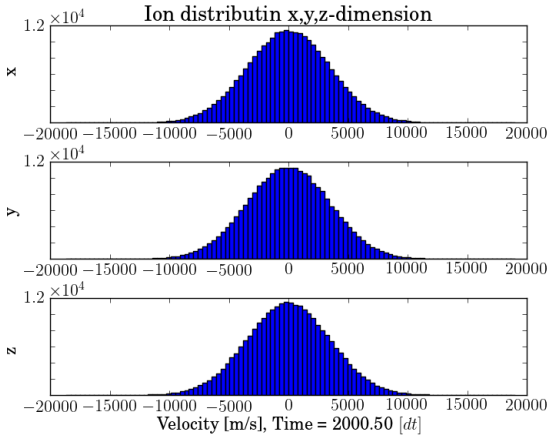

(b) Final Ion-Elastic

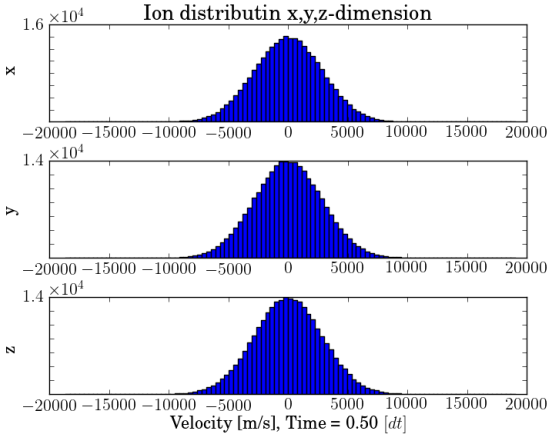

(c) Initial Charge-Exchange

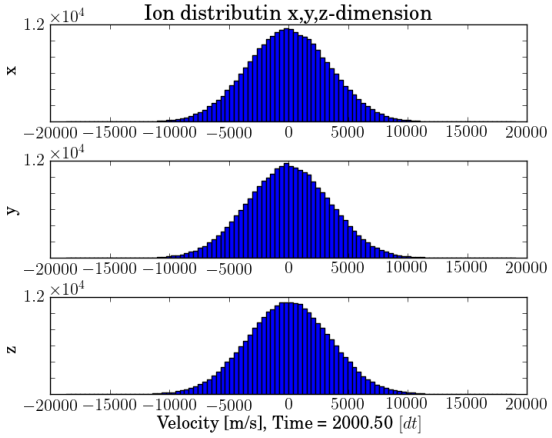

(d) Final Charge-Exchange

Figure A.2: Collection of initial and final v_x, v_y, v_z distributions for the higher neutral temperature case $T_n = 1500$.

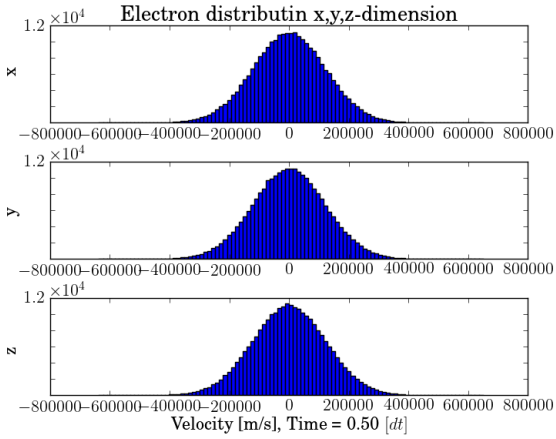

(a) Initial vx,vy,vz distributions

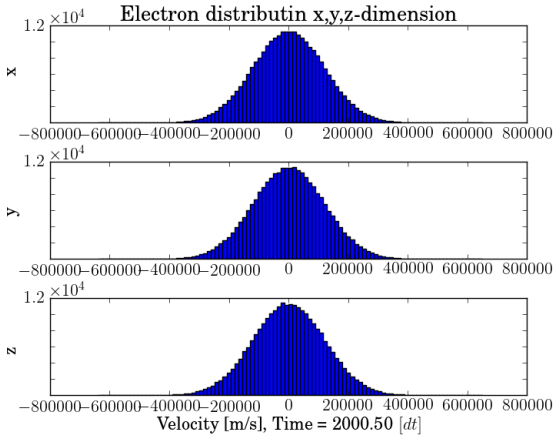

(b) Final vx,vy,vz distributions

Figure A.3: Collection of initial and final v_x, v_y, v_z distributions, only electron-elastic collisions are turned on, and $T_n = 1000K$. Values are relative to the number of particles in the simulation.

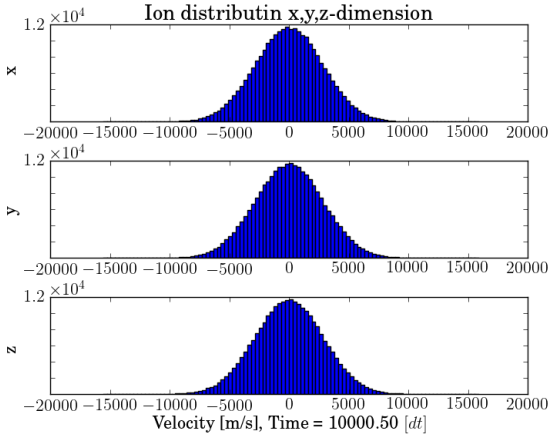

(a) Final Ion distributions

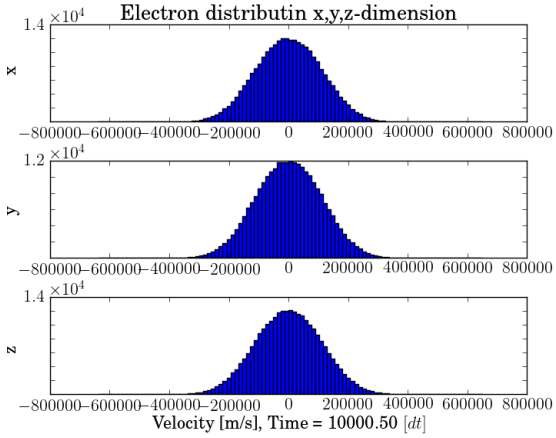

(b) Final electron distributions

Figure A.4: Plots of final v_x, v_y, v_z distributions. All collisions are turned on, and the test is run for an extended period of time. The neutral temperature $T_n = 1000K$. Values are relative to the number of particles in the simulation.

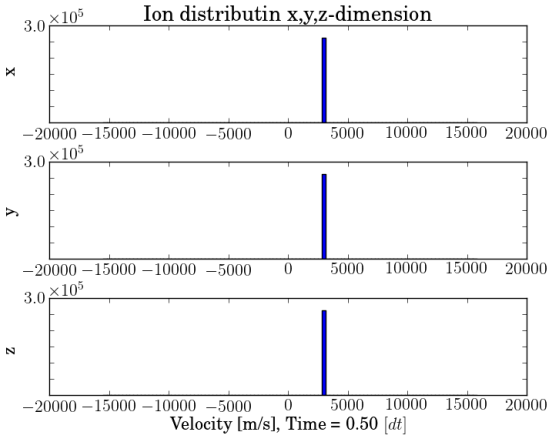

(a) Initial vx,vy,vz distributions

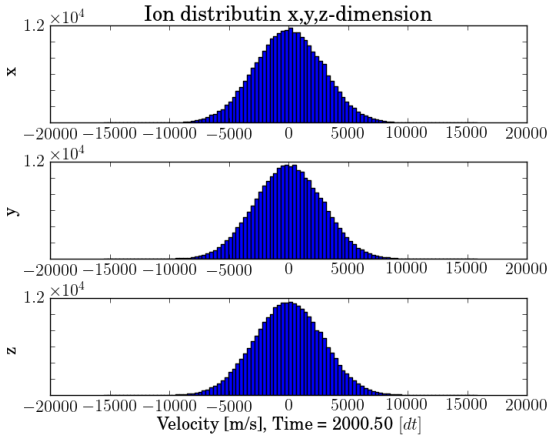

(b) Final vx,vy,vz distributions

Figure A.5: Initial and final v_x, v_y, v_z distributions for the extreme case where all particles initially have the same velocity. The neutral temperature is $T_n = 1000K$. Values are relative to the number of particles in the simulation.

Appendix B

Growth rate Baseline vs Optional

To explain the differences in the Optional simulation and the Baseline simulation, we solve the growth function eq. 2.41 numerically and compare the solution in an "ideal" case $k_{\parallel} = 0$ to a case where $k_{\parallel} = finite$.

We use the expression for ψ containing $k_{\parallel}$

$$\psi = \frac{\nu_e \nu_i}{\Omega_e \Omega_i}\left(1 + \frac{\Omega_e^2 k_{\parallel}^2}{\nu_e^2 k^2}\right) \tag{B.1}$$

and chose all other values to correspond to the ones given in table 4.1 a) and b).

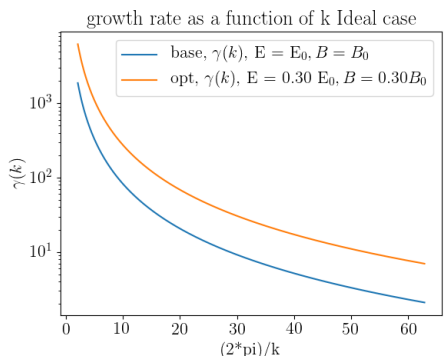

(a) Ideal case using original parameters.

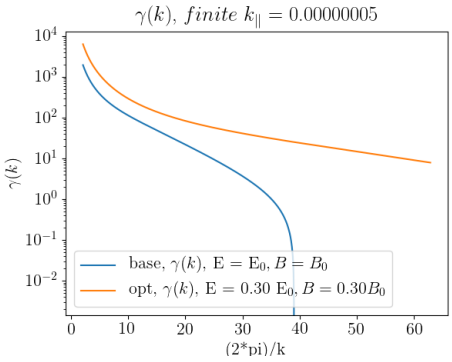

(b) Using a finite $k_{\|}$ with original parameters.

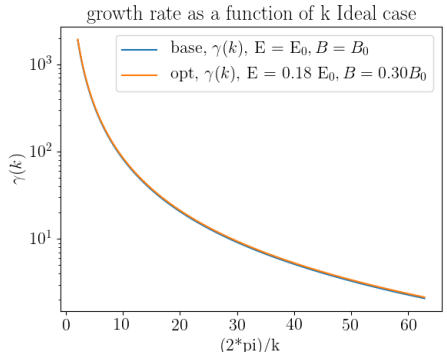

(c) Ideal case, matched growth

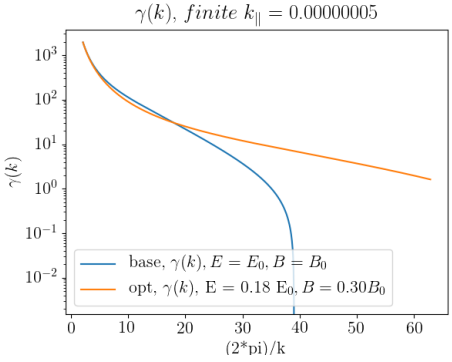

(d) Finite $k_{\|}$, matched parameters

Figure B.1: Solution to the growth function using Baseline vs Optional parameters. Ideal case means $k_{\|} = 0$. In the finite $k_{\|}$ case, $k_{\|}$ was chosen to emphasize the different behaviour of the growth. Figure c, and d show the growth when B_0 is further modified to try and match the growth between the Baseline and Optional simulation.

We see in fig. B.1 a) and c), that in the case of $k_{\|} = 0$, the simulations should feature the same physics. in fig. a), we use the same values as the ones used in the simulations, and the form is the same. The Optional simulation does however have a higher growth for any given k. In fig. c) we can see that it is possible to further modify the input parameters to match the growth of the two simulations. The reason why these are not the same is the ν_i in the denominator of the first term of the growth function eq. 2.41. This value had to be changed to maintain the Pedersen, and Hall currents. But as we see it should be possible to run the simulation with a lower driving electric field to produce the same physical system.

The caveat to this is shown in fig. B.1 b) and d). In these figures we see that if we give $k_{\|}$ a finite value other than zero, it is impossible to retain the same physics. The value used here is $k_{\|} = 0.00000005$, which corresponds to a wavelength of $125663706m$. If we use a more reasonable value of $k_{\|} = 0.5$ ($12.5m$), there are no positive values

for $\gamma(k)$, in fact $k_{||}$ needs to be of the order of 10^{-6} to have any positive values. This suggests that in a simulation constrained by a finite simulation domain smaller than $10^6 m$ the only valid solution is the one where $k_{||} = 0$. however fig. b) and d) also suggest that if $k_{||}$ is important, the physics might be different in the two simulations.

Bibliography

Bahcivan, Hasan and Russell Cosgrove (2010). "On the generation of large wave parallel electric fields responsible for electron heating in the high-latitude E region". en. In: *Journal of Geophysical Research: Space Physics* 115.A10. ISSN: 2156-2202. DOI: 10.1029/2010JA015424. URL: https://agupubs.onlinelibrary.wiley.com/doi/abs/10.1029/2010JA015424 (visited on 12/20/2018).

Baumjohann, Wolfgang and Rudolf A. Treumann (1997). *Basic Space Plasma Physics*. en. Google-Books-ID: e4yupcOzJxkC. World Scientific. ISBN: 978-1-86094-079-8.

Birdsall, C.K. (May 1991). "Particle-in-cell charged-particle simulations, plus Monte Carlo collisions with neutral atoms, PIC-MCC". In: *Plasma Science, IEEE Transactions on* 19, pp. 65–85. DOI: 10.1109/27.106800.

Birdsall, Charles K. and A. Bruce Langdon (1985). *Plasma physics via computer simulation*. en. Google-Books-ID: 7TMbAQAAIAAJ. McGraw-Hill. ISBN: 978-0-07-005371-7.

Buneman, O. (Apr. 1963). "Excitation of Field Aligned Sound Waves by Electron Streams". In: *Physical Review Letters* 10.7, pp. 285–287. DOI: 10.1103/PhysRevLett.10.285. URL: https://link.aps.org/doi/10.1103/PhysRevLett.10.285 (visited on 12/19/2018).

Chen, Francis F. (2016). *Introduction to Plasma Physics and Controlled Fusion*. en. 3rd ed. Springer International Publishing. ISBN: 978-3-319-22308-7. URL: //www.springer.com/la/book/9783319223087 (visited on 12/05/2018).

Courant, R., K. Friedrichs, and H. Lewy (Mar. 1967). "On the Partial Difference Equations of Mathematical Physics". In: *IBM J. Res. Dev.* 11.2, pp. 215–234. ISSN: 0018-8646. DOI: 10.1147/rd.112.0215. URL: http://dx.doi.org/10.1147/rd.112.0215 (visited on 12/20/2018).

Dimant, Y. S. and R. N. Sudan (Aug. 1995). "Kinetic theory of the Farley-Buneman instability in the E region of the ionosphere". In: *Journal of Geophysical Research: Space Physics* 100.A8, pp. 14605–14623. ISSN: 0148-0227. DOI: 10.1029/95JA00794. URL: https://agupubs.onlinelibrary.wiley.com/doi/abs/10.1029/95JA00794 (visited on 12/19/2018).

Dimant, Yakov S. and Meers M. Oppenheim (2003). "Ion thermal effects on Eregion instabilities : linear theory". In:

Eckersley, T. L. (Nov. 1937). "Irregular Ionic Clouds in the *E* Layer of the Ionosphere". en. In: *Nature* 140.3550, pp. 846–847. ISSN: 1476-4687. DOI: 10.1038/140846a0. URL: https://www.nature.com/articles/140846a0 (visited on 12/19/2018).

Farley Jr., D. T. (Nov. 1963). "A plasma instability resulting in field-aligned irregularities in the ionosphere". In: *Journal of Geophysical Research* 68.22, pp. 6083–6097. ISSN: 0148-0227. DOI: 10.1029/JZ068i022p06083. URL: https://agupubs.onlinelibrary.wiley.com/doi/abs/10.1029/JZ068i022p06083 (visited on 12/19/2018).

Farley, D. T. (Aug. 1985). "Theory of equatorial electrojet plasma waves: new developments and current status". In: *Journal of Atmospheric and Terrestrial Physics* 47.8, pp. 729–744. ISSN: 0021-9169. DOI: 10.1016/0021-9169(85)90050-9. URL: http://www.sciencedirect.com/science/article/pii/0021916985900509 (visited on 12/19/2018).

— (Apr. 2009). "The equatorial E-region and its plasma instabilities: a tutorial". English. In: *Annales Geophysicae* 27.4, pp. 1509–1520. ISSN: 0992-7689. DOI: https://doi.org/10.5194/angeo-27-1509-2009. URL: https://www.ann-geophys.net/27/1509/2009/ (visited on 12/19/2018).

Fejer, B.G. et al. (Apr. 1975). "Vertical structure of the VHF backscattering region in the equatorial electrojet and the gradient drift instability". In: *Journal of Geophysical Research* 80, pp. 1313–1324. DOI: 10.1029/JA080i010p01313.

Fejer, Bela G., Jason Providakes, and Donald T. Farley (1984). "Theory of plasma waves in the auroral E region". en. In: *Journal of Geophysical Research: Space Physics* 89.A9, pp. 7487–7494. ISSN: 2156-2202. DOI: 10.1029/JA089iA09p07487. URL: https://agupubs.onlinelibrary.wiley.com/doi/abs/10.1029/JA089iA09p07487 (visited on 12/19/2018).

Gurevich, A. (1978). *Nonlinear Phenomena in the Ionosphere*. en. Physics and Chemistry in Space. Berlin Heidelberg: Springer-Verlag. ISBN: 978-3-642-87651-6. URL: //www.springer.com/us/book/9783642876516 (visited on 12/20/2018).

Haldoupis, C. et al. (Nov. 2005). "Is there a plasma density gradient role on the generation of short-scale Farley-Buneman waves?" English. In: *Annales Geophysicae* 23.10, pp. 3323–3337. ISSN: 0992-7689. DOI: https://doi.org/10.5194/angeo-23-3323-2005. URL: https://www.ann-geophys.net/23/3323/2005/ (visited on 12/20/2018).

Hamza, A. M. and H. Imamura (2001). "On the excitation of large aspect angle Farley-Buneman echoes via three-wave coupling: A dynamical system model". en. In: *Journal of Geophysical Research: Space Physics* 106.A11, pp. 24745–24754. ISSN: 2156-2202. DOI: 10.1029/2000JA000065. URL: https://agupubs.onlinelibrary.wiley.com/doi/abs/10.1029/2000JA000065 (visited on 12/13/2018).

Hockney, R. W. and J. W. Eastwood (Jan. 1988). *Computer Simulation Using Particles*. en. Google-Books-ID: nTOFkmnCQuIC. CRC Press. ISBN: 978-1-4398-2205-0.

Horký, M. and W. J. Miloch (2015a). "Kinetic plasma instabilities due to charge exchange and elastic collisions". en. In: *Journal of Physics: Conference Series*

591.1, p. 012034. ISSN: 1742-6596. DOI: 10.1088/1742-6596/591/1/012034. URL: http://stacks.iop.org/1742-6596/591/i=1/a=012034 (visited on 04/09/2018).

— (Feb. 2015b). "Numerical study on the stability of weakly collisional plasma in E×B fields". In: *Physics of Plasmas* 22.2, p. 022109. ISSN: 1070-664X. DOI: 10.1063/1.4906887. URL: http://aip.scitation.org/doi/abs/10.1063/1.4906887 (visited on 07/25/2017).

Horký, M., W. J. Miloch, and V. A. Delong (Apr. 2017). "Numerical heating of electrons in particle-in-cell simulations of fully magnetized plasmas". In: *Physical Review E* 95.4, p. 043302. DOI: 10.1103/PhysRevE.95.043302. URL: https://link.aps.org/doi/10.1103/PhysRevE.95.043302 (visited on 12/19/2018).

Hysell, D. L. and J. Drexler (Aug. 2006). "Polarization of elliptic E region plasma irregularities and implications for coherent radar backscatter from Farley-Buneman waves". In: *Radio Science* 41.04, pp. 1–11. ISSN: 1944-799X. DOI: 10.1029/2005RS003424.

Iijima, T. and T. A. Potemra (Feb. 1978). "Large-scale characteristics of field-aligned currents associated with substorms". en. In: *Journal of Geophysical Research: Space Physics* 83.A2, pp. 599–615. ISSN: 2156-2202. DOI: 10.1029/JA083iA02p00599. URL: http://onlinelibrary.wiley.com/doi/10.1029/JA083iA02p00599/abstract (visited on 11/26/2016).

Janhunen, P. (June 1994). "Perpendicular particle simulation of the E region Farley-Buneman instability". In: *Journal of Geophysical Research: Space Physics* 99.A6, pp. 11461–11473. ISSN: 0148-0227. DOI: 10.1029/94JA00206. URL: https://agupubs.onlinelibrary.wiley.com/doi/10.1029/94JA00206 (visited on 12/19/2018).

Kagan, L. M. and M. C. Kelley (Mar. 2000). "A thermal mechanism for generation of small-scale irregularities in the ionospheric E region". In: *Journal of Geophysical Research: Space Physics* 105.A3, pp. 5291–5303. ISSN: 0148-0227. DOI: 10.1029/1999JA900415. URL: https://agupubs.onlinelibrary.wiley.com/doi/abs/10.1029/1999JA900415 (visited on 11/23/2018).

Kagan, Ludmila M. (Aug. 2002). "Effects of neutral gas motions on midlatitude E region irregular structure". In: *Journal of Atmospheric and Solar-Terrestrial Physics*. Equatorial Aeronomy 64.12, pp. 1479–1486. ISSN: 1364-6826. DOI: 10.1016/S1364-6826(02)00112-8. URL: http://www.sciencedirect.com/science/article/pii/S1364682602001128 (visited on 11/23/2018).

Killie, Gullik Vetvik (2016). "A Parallel Multigrid Poisson Solver for PINC, a new Particle-in-Cell Model". eng. In: URL: https://www.duo.uio.no/handle/10852/54053 (visited on 12/19/2018).

Kissack, R. S., J.-P. St-Maurice, and D. R. Moorcroft (Apr. 1995). "Electron thermal effects on the Farley–Buneman fluid dispersion relation". In: *Physics of Plasmas* 2.4, pp. 1032–1055. ISSN: 1070-664X. DOI: 10.1063/1.871383. URL: https://aip.scitation.org/doi/abs/10.1063/1.871383 (visited on 11/23/2018).

Koura, K. (Jan. 1998). "Improved null-collision technique in the direct simulation Monte Carlo method: Application to vibrational relaxation of nitrogen". In: *Com-*

puters & Mathematics with Applications 35.1, pp. 139–154. ISSN: 0898-1221. DOI: 10.1016/S0898-1221(97)00264-2. URL: http://www.sciencedirect.com/science/article/pii/S0898122197002642 (visited on 10/19/2017).

Kovalev, D. V., A. P. Smirnov, and Y. S. Dimant (Sept. 2008). "Modeling of the Farley-Buneman instability in the E-region ionosphere: a new hybrid approach". English. In: *Annales Geophysicae* 26.9, pp. 2853–2870. ISSN: 0992-7689. DOI: https://doi.org/10.5194/angeo-26-2853-2008. URL: https://www.ann-geophys.net/26/2853/2008/ (visited on 12/19/2018).

Langdon, A. Bruce (Jan. 1979). "Kinetic theory for fluctuations and noise in computer simulation of plasma". In: *The Physics of Fluids* 22.1, pp. 163–171. ISSN: 0031-9171. DOI: 10.1063/1.862452. URL: https://aip.scitation.org/doi/10.1063/1.862452 (visited on 12/19/2018).

Lapenta, Giovanni (Feb. 2012). "Particle simulations of space weather". In: *Journal of Computational Physics*. Special Issue: Computational Plasma PhysicsSpecial Issue: Computational Plasma Physics 231.3, pp. 795–821. ISSN: 0021-9991. DOI: 10.1016/j.jcp.2011.03.035. URL: //www.sciencedirect.com/science/article/pii/S0021999111001860 (visited on 01/24/2017).

Madsen, Chad A. et al. (Feb. 2014). "The Multi-Species Farley-Buneman Instability in the Solar Chromosphere". In: *The Astrophysical Journal* 783.2. arXiv: 1308.0305, p. 128. ISSN: 0004-637X, 1538-4357. DOI: 10.1088/0004-637X/783/2/128. URL: http://arxiv.org/abs/1308.0305 (visited on 07/25/2017).

McNamara, A. G. (Sept. 1969). "Rocket measurements of plasma densities and temperatures in visual aurora". In: *Canadian Journal of Physics* 47.18, pp. 1913–1927. ISSN: 0008-4204. DOI: 10.1139/p69-242. URL: http://www.nrcresearchpress.com/doi/abs/10.1139/p69-242 (visited on 12/19/2018).

Miloch, W. J., H. L. Pécseli, and J. K. Trulsen (2013). "Unstable ring-shaped ion distribution functions induced by charge–exchange collisions". en. In: *Plasma Physics and Controlled Fusion* 55.12, p. 124006. ISSN: 0741-3335. DOI: 10.1088/0741-3335/55/12/124006. URL: http://stacks.iop.org/0741-3335/55/i=12/a=124006 (visited on 07/25/2017).

Nevins, W. M. et al. (Dec. 2005). "Discrete particle noise in particle-in-cell simulations of plasma microturbulence". In: *Physics of Plasmas* 12.12, p. 122305. ISSN: 1070-664X. DOI: 10.1063/1.2118729. URL: https://aip.scitation.org/doi/10.1063/1.2118729 (visited on 12/19/2018).

Oppenheim M. M. and Dimant Y. S. (Feb. 2013). "Kinetic simulations of 3-D Farley-Buneman turbulence and anomalous electron heating". In: *Journal of Geophysical Research: Space Physics* 118.3, pp. 1306–1318. ISSN: 2169-9380. DOI: 10.1002/jgra.50196. URL: https://agupubs.onlinelibrary.wiley.com/doi/full/10.1002/jgra.50196 (visited on 04/04/2018).

Oppenheim, M. M. and Y. S. Dimant (Nov. 2004). "Ion thermal effects on E-region instabilities: 2D kinetic simulations". In: *Journal of Atmospheric and Solar-Terrestrial Physics*. 40 Years of Equatorial Aeronomy Sparked by the Jicamarca Radio Obser-

vatory 66.17, pp. 1655–1668. ISSN: 1364-6826. DOI: 10.1016/j.jastp.2004.07.007. URL: http://www.sciencedirect.com/science/article/pii/S1364682604001646 (visited on 11/23/2018).

Oppenheim, M. M., Y. Dimant, and L. P. Dyrud (Mar. 2008). "Large-scale simulations of 2-D fully kinetic Farley-Buneman turbulence". In: *Ann. Geophys.* 26.3, pp. 543–553. ISSN: 1432-0576. DOI: 10.5194/angeo-26-543-2008. URL: https://www.ann-geophys.net/26/543/2008/ (visited on 11/23/2018).

Oppenheim, Meers, Niels Otani, and Corrado Ronchi (1995). "Hybrid simulations of the saturated Farley-Buneman instability in the ionosphere". en. In: *Geophysical Research Letters* 22.4, pp. 353–356. ISSN: 1944-8007. DOI: 10.1029/94GL03277. URL: https://agupubs.onlinelibrary.wiley.com/doi/abs/10.1029/94GL03277 (visited on 12/19/2018).

— (Aug. 1996). "Saturation of the Farley-Buneman instability via nonlinear electron E×B drifts". en. In: *Journal of Geophysical Research: Space Physics* 101.A8, pp. 17273–17286. ISSN: 2156-2202. DOI: 10.1029/96JA01403. URL: http://onlinelibrary.wiley.com/doi/10.1029/96JA01403/abstract (visited on 09/29/2017).

Otani, Niels and Meers Oppenheim (Mar. 2006). "Saturation of the Farley-Buneman instability via three-mode coupling". In: *Journal of Geophysical Research* 111. DOI: 10.1029/2005JA011215.

Pécseli, H (Sept. 2012). "Waves and Oscillations in Plasmas". In: *Waves and Oscillations in Plasmas. Series: Series in Plasma Physics, ISBN: 978-1-4398-7848-4. Taylor & Francis, Edited by Hans Pécseli*. DOI: 10.1201/b12702.

Pécseli, H. L., F. Primdahl, and A. Bahnsen (1989). "Low-frequency electrostatic turbulence in the polar cap E region". en. In: *Journal of Geophysical Research: Space Physics* 94.A5, pp. 5337–5349. ISSN: 2156-2202. DOI: 10.1029/JA094iA05p05337. URL: https://agupubs.onlinelibrary.wiley.com/doi/abs/10.1029/JA094iA05p05337 (visited on 12/27/2018).

Prölss, Gerd (July 2004). *Physics of the Earth's Space Environment: An Introduction*. en. Google-Books-ID: GKS5pI3feW4C. Springer Science & Business Media. ISBN: 978-3-540-21426-7.

Qin, Hong et al. (Aug. 2013). "Why is Boris algorithm so good?" In: *Physics of Plasmas* 20.8, p. 084503. ISSN: 1070-664X. DOI: 10.1063/1.4818428. URL: https://aip.scitation.org/doi/10.1063/1.4818428 (visited on 12/19/2018).

Rosenberg, M and V.W. Chow (Jan. 1998). "Farley-Buneman instability in a dusty plasma". In: *Planetary and Space Science* 46, pp. 103–108. DOI: 10.1016/S0032-0633(97)00104-9.

Sahr, J. D. et al. (June 1992). "Observations of 3-m auroral irregularities during the ERRRIS campaigns". In: *Journal of Atmospheric and Terrestrial Physics*. E-Region Irregularities 54.6, pp. 809–818. ISSN: 0021-9169. DOI: 10.1016/0021-9169(92)90117-4. URL: http://www.sciencedirect.com/science/article/pii/0021916992901174 (visited on 06/15/2018).

Sahr, John and Bela G. Fejer (Dec. 1996). "Auroral electrojet plasma irregularity theory and experiment: A critical review of present understanding and future directions". In: *Journal of Geophysical Research* 101, pp. 26893–26909. DOI: 10.1029/96JA02404.

Schield, Milo A., J. W. Freeman, and A. J. Dessler (1969). "A source for field-aligned currents at auroral latitudes". In: *Journal of Geophysical Research* 74.1, pp. 247–256. URL: http://onlinelibrary.wiley.com/doi/10.1029/JA074i001p00247/full (visited on 11/26/2016).

St. -Maurice, J.-P. and R. S. Kissack (May 2000). "The role played by thermal feedback in heated Farley-Buneman waves at high latitudes". English. In: *Annales Geophysicae* 18.5, pp. 532–546. ISSN: 0992-7689. DOI: https://doi.org/10.1007/s00585-000-0532-x. URL: https://www.ann-geophys.net/18/532/2000/ (visited on 11/23/2018).

St.-Maurice, J.-P. and A. M. Hamza (2001). "A new nonlinear approach to the theory of E region irregularities". en. In: *Journal of Geophysical Research: Space Physics* 106.A2, pp. 1751–1759. ISSN: 2156-2202. DOI: 10.1029/2000JA000246. URL: https://agupubs.onlinelibrary.wiley.com/doi/abs/10.1029/2000JA000246 (visited on 12/20/2018).

Sudan, R. N., J. Akinrimisi, and D. T. Farley (1973). "Generation of small-scale irregularities in the equatorial electrojet". en. In: *Journal of Geophysical Research* 78.1, pp. 240–248. ISSN: 2156-2202. DOI: 10.1029/JA078i001p00240. URL: https://agupubs.onlinelibrary.wiley.com/doi/abs/10.1029/JA078i001p00240 (visited on 12/20/2018).

Surendra, M., D. B. Graves, and G. M. Jellum (Jan. 1990). "Self-consistent model of a direct-current glow discharge: Treatment of fast electrons". en. In: *Physical Review A* 41.2, pp. 1112–1125. ISSN: 1050-2947, 1094-1622. DOI: 10.1103/PhysRevA.41.1112. URL: https://link.aps.org/doi/10.1103/PhysRevA.41.1112 (visited on 04/10/2018).

Tabata, Tatsuo and Toshizo Shirai (Sept. 2000). "ANALYTIC CROSS SECTIONS FOR COLLISIONS OF H+, H2+, H3+, H, H2, AND H WITH HYDROGEN MOLECULES". en. In: *Atomic Data and Nuclear Data Tables* 76.1, pp. 1–25. ISSN: 0092640X. DOI: 10.1006/adnd.2000.0835. URL: http://linkinghub.elsevier.com/retrieve/pii/S0092640X00908350 (visited on 11/20/2017).

Trivellato, F. and M. Raciti Castelli (2014). "On the Courant–Friedrichs–Lewy criterion of rotating grids in 2D vertical-axis wind turbine analysis". In: *Renewable Energy* 62.C, pp. 53–62. ISSN: 0960-1481. URL: https://econpapers.repec.org/article/eeerenene/v_3a62_3ay_3a2014_3ai_3ac_3ap_3a53-62.htm (visited on 12/20/2018).

Trottenberg, Ulrich, Cornelius W. Oosterlee, and Anton Schuller (Nov. 2000). *Multigrid*. en. Google-Books-ID: 9ysyNPZoR24C. Academic Press. ISBN: 978-0-08-047956-9.

Vahedi, V. and M. Surendra (May 1995). "A Monte Carlo collision model for the particle-in-cell method: applications to argon and oxygen discharges". In: *Computer*

Physics Communications. Particle Simulation Methods 87.1, pp. 179–198. ISSN: 0010-4655. DOI: 10.1016/0010-4655(94)00171-W. URL: http://www.sciencedirect.com/science/article/pii/001046559400171W (visited on 10/19/2017).

Verboncoeur, J P (May 2005). "Particle simulation of plasmas: review and advances". In: *Plasma Physics and Controlled Fusion* 47.5A, A231–A260. ISSN: 0741-3335, 1361-6587. DOI: 10.1088/0741-3335/47/5A/017. URL: http://stacks.iop.org/0741-3335/47/i=5A/a=017?key=crossref.c855d4d27c6daaf363c1c23c98f94d28 (visited on 12/19/2018).